

NASA Contractor Report 159255

(NASA-CR-159255) MAGNETIC SUSPENSION SYSTEM
FOR AN ANNULAR MOMENTUM CONTROL DEVICE
(AMCD) (Sperry Flight Systems, Phoenix,
Ariz.) 114 p HC A06/MF A01

N80-24551

CSSL 09C

Unclass

G3/33 21032

Magnetic Suspension System for an Annular Momentum Control Device (AMCD)

*Revised
Copy*

SPERRY FLIGHT SYSTEMS
PHOENIX, AZ 85036

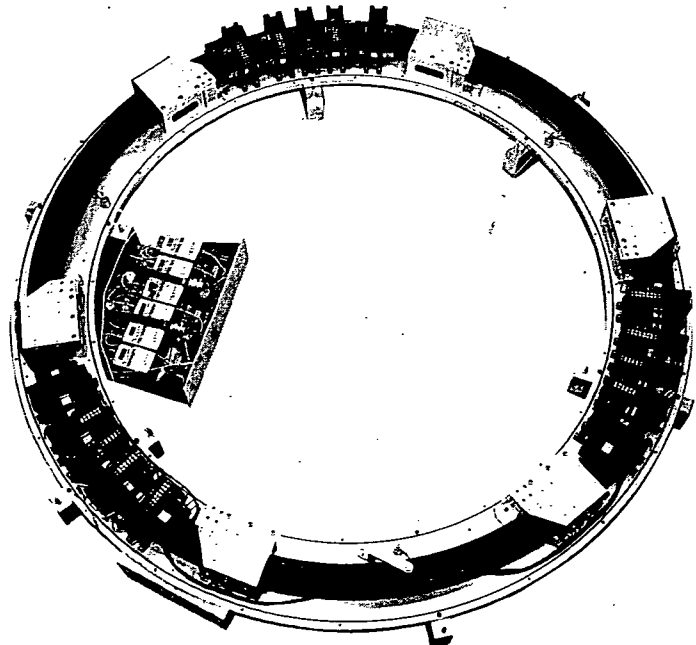
CONTRACT NO. NAS1-14502
DECEMBER 1979

FOR



National Aeronautics and
Space Administration

Langley Research Center
Hampton, Virginia 23665



NASA Contractor Report 159255

Magnetic Suspension System for an Annular Momentum Control Device (AMCD)

SPERRY FLIGHT SYSTEMS
PHOENIX, AZ 85036

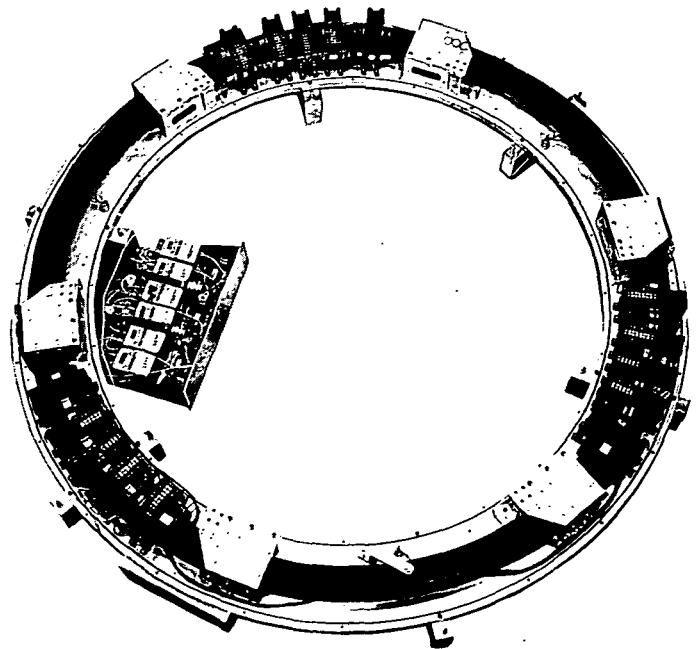
CONTRACT NO. NAS1-14502
DECEMBER 1979

FOR



National Aeronautics and
Space Administration

Langley Research Center
Hampton, Virginia 23665



PREFACE

The Annular Momentum Control Device (AMCD) represents a new concept in momentum storage devices, and is proposed for the control and stabilization of spacecraft. The basic AMCD concept is that of a rotating thin rim which is suspended by a minimum of three noncontacting magnetic suspension stations and driven by a noncontacting electromagnetic spin motor. A detailed discussion of the rationale for the AMCD configuration and its potential applications are presented in Reference 1.

To investigate potential problem areas in implementing the AMCD concept, a laboratory test model was built and is being used as part of a continuing AMCD hardware technology development. A detailed description of the laboratory test model AMCD is given in Reference 2. The original suspension system for the laboratory model utilized permanent magnet flux-biased magnetic bearing elements which presented certain constraints on suspension system performance.^{3,4} Because of these constraints, a decision was made to explore an alternate approach to the design of the magnetic suspension system. Subsequently, a contract for the design, fabrication, and testing of a new magnetic suspension system for the existing laboratory test model AMCD was awarded to Sperry Flight Systems.

The resulting Sperry design required all new suspension electronics as well as heavy duty actuators capable of levitating the rim independent of a permanent magnet bias. The design also made provisions for an electromagnetic bias scheme where the actuators could simulate the original control scheme. Also included within the control law were two primary modes of operation⁴ - direct and precession. The direct mode was designed to provide direct servo control up to 750 r/min and then switch over to a precessional control mode for speeds up to 2740 r/min. Each mode was designed for a bandwidth of two hertz. The advantage of the scheme was to account for precessional cross-coupling effects while high momentum was present in the system and to keep the bandwidth low to avoid excitation of rim bending modes.

An analysis of direct and precession mode control, as applied to a double gimbal control moment gyroscope, is presented in Reference 5.

The original checkout and system evaluation revealed that both axial and radial control loops exhibited instability in the form of a limit cycle. Further tests traced the cause of the limit cycle to mismatches between each magnetic bearing actuator and to minor mounting dimension differences. Using a process of improving actuator calibration data and raising the suspension bandwidth to compensate for the calibration error, a stable zero rpm suspension system was achieved. The resulting bandwidths were set at 16 Hz for the axial loops and 28 Hz for the radial control loops. By comparison, the original magnetic suspension system contained loops set at approximately 27 Hz and 10 Hz, respectively.² As the control problem was concluded, continued analysis disclosed that the radial sensors were insufficient for use at high rim velocities. Previous analysis disclosed that rotational effects caused the rim to expand .050+ inch at full speed, whereas the radial sensors had only a .10-inch total measurement distance. The predicted rim growth, when added to the operating position of the rim when at zero velocity, indicated that a highly nonlinear result would be seen when at full distention. This would result in a highly nonlinear force calculation and, in turn, cause instability within the operating system. The solution to this dilemma was to exchange the existing sensors with a set whose measurement range would be linear under all operating conditions.

Simultaneously, an effort was expended to more accurately characterize the electromagnetic force constants available from the actuators. This effort yielded a better constant value and was incorporated into the operating system. No measurement, however, was made to reflect the small differences between individual actuators.

Further into the program, a system alignment and base plate stiffness problem surfaced. This was resolved by providing axial support at six points and, in particular, directly beneath each proximeter sensor. The increased stiffness immediately reduced an instability problem caused by the support system. In conjunction with this effort, a concentrated effort to level the rim was made so that the system alignment was assured to less than .001 inch. At

the same time, all of the proximeter control units were slaved together and were operated at a single common frequency. This step resolved a crosscoupling effect observed as a beat frequency phenomena within the operating system.

At this stage in the checkout procedure, the zero-speed testing was begun.

TABLE OF CONTENTS

Section		Page No.
	PREFACE	iii
1.0	INTRODUCTION	2
2.0	DESCRIPTION OF THE SYSTEM	4
	2.1 Objectives	11
3.0	DATA COLLECTION	13
	3.1 Important Milestones Achieved	17
4.0	INTERPRETATION OF COLLECTED DATA	20
	4.1 Data Collected at Zero R/Min	20
	4.1.1 Step Response at Zero R/Min	20
	4.1.2 Frequency Response at Zero R/Min	20
	4.2 Data Collected at 500 R/Min	35
	4.2.1 Step Response at 500 R/Min	35
	4.2.2 Frequency Response at 500 R/Min	35
	4.3 Higher Speeds	35
	4.4 Interpretation	48
5.0	ANALOG COMPUTER SIMULATION	51
	5.1 Description	51
	5.2 Results	53
6.0	REFERENCES	56

TABLE OF CONTENTS (cont)

Section	Page No.
Appendix	
A ANALOG SIMULATION MODEL	58
A.1 Simulation Schematic and Scaling	58
A.1.1 Radial Loop Simulation	59
A.1.1.1 Force Command to Current Command	59
A.1.1.2 Current Command to Force Applied	65
A.1.1.3 Force to Gap Rate	66
A.1.1.4 Radial Gap	67
A.1.2 Axial Loop Simulation	67
A.1.2.1 Force Command to Current Command	68
A.1.2.2 Current Command to Force Applied	70
A.1.2.3 Force to Gap Rate	71
A.1.2.4 Torque to Rotation Rate	72
A.1.2.5 Angular Rates to Axial Displacement Rates	73
A.1.2.6 Axial Displacement Rates to Axial Gaps	75
A.1.3 Radial Ripples in the Rim	76
A.1.4 Axial Ripples in the Rim	79
A.1.5 Mass Imbalance	81
A.2 Static Test Scheme for AMCD Simulation	82
B AMCD LOW SPEED BALANCE	90
B.1 Balance Improvement at 200 R/Min	90
B.2 Balance Improvement at 350 R/Min	94
C AMCD MAGNETIC BEARING CHARACTERIZATION	100

LIST OF ILLUSTRATIONS

Figure No.		Page No.
1	Laboratory Test Model AMCD Layout (Photograph)	5
2	Station 3 MBA and the Hall Sensor (Photograph)	6
3	Radial Actuator Control System Dynamic Model	8
4	Axial Actuator Control System Dynamic Model	9
5	AMCD Actuator Dynamic Models	10
6	Setup for Open-Loop Frequency Response	14
7	Setup for Closed-Loop Frequency Response	15
8	Sample Recording	16
9	Step Response at Zero Speed (ΔX , ΔY Loops)	21
10	Step Response at Zero Speed (ΔZ Loop)	22
11	Step Response at Zero Speed ($\Delta\theta_x$, $\Delta\theta_y$ Loops)	23
12	Closed-Loop Frequency Response at Zero Speed for ΔX Loop	24
13	Closed-Loop Frequency Response at Zero Speed for ΔY Loop	25
14	Closed-Loop Frequency Response at Zero Speed for ΔZ Loop	26
15	Closed-Loop Frequency Response at Zero Speed for $\Delta\theta_x$ Loop	27
16	Closed-Loop Frequency Response at Zero Speed for $\Delta\theta_y$ Loop	28
17	Open-Loop Frequency Response at Zero Speed for ΔX Loop	29
18	Open-Loop Frequency Response at Zero Speed for ΔY Loop	30
19	Open-Loop Frequency Response at Zero Speed for ΔZ Loop	31
20	Open-Loop Frequency Response at Zero Speed for $\Delta\theta_x$ Loop	32
21	Open-Loop Frequency Response at Zero Speed for $\Delta\theta_y$ Loop	33
22	Closed-Loop Step Response at 500 R/Min	36
23	Closed-Loop Frequency Response at 500 R/Min for ΔX Loop	38
24	Closed-Loop Frequency Response at 500 R/Min for ΔY Loop	39
25	Closed-Loop Frequency Response at 500 R/Min for ΔZ Loop	40

LIST OF ILLUSTRATIONS (cont)

Figure No.		Page No.
26	Closed-Loop Frequency Response at 500 R/Min for $\Delta\theta_x$ Loop	41
27	Closed-Loop Frequency Response at 500 R/Min for $\Delta\theta_y$ Loop	42
28	Open-Loop Frequency Response at 500 R/Min for ΔX Loop	43
29	Open-Loop Frequency Response at 500 R/Min for ΔY Loop	44
30	Open-Loop Frequency Response at 500 R/Min for ΔZ Loop	45
31	Open-Loop Frequency Response at 500 R/Min for $\Delta\theta_x$ Loop	46
32	Open-Loop Frequency Response at 500 R/Min for $\Delta\theta_y$ Loop	47
33	AMCD Analog Simulation Setup	52
34	Step Response of Design Simulation	54
35	AMCD System Configuration for Analog Simulation	58
36	AMCD Radial Loops	61
37	AMCD Axial Loops	63
38	Balance Improvement at 200 R/Min	93
39	Balance Improvement at 200 R/Min	95
40	Balance Improvement at 350 R/Min	96

LIST OF TABLES

Table No.		Page No.
1	AMCD Characterization at Zero R/Min	34
2	AMCD Characterization at 500 R/Min	37
3	AMCD Radial Loops Board	83
4	AMCD Axial Loops Board	84
5	Radial Board Checklist	87
6	Axial Board Checklist	88

SECTION 1.0

INTRODUCTION

This final report for the Magnetic Suspension System for the Annular Momentum Control Device, AMCD, describes the important milestones achieved during its development. It includes description of the system and various test setups along with illustrative diagrams. It describes techniques of data collection at zero- and 500-r/min speed of the rim and interpretation of the data collected. A detailed description of the analog simulation, together with a static check scheme for future reference, is included in Appendix A. Appendix B explains how dynamic balancing of the rim was accomplished to improve response of the rim at speeds greater than 200 r/min. Appendix C is added to illustrate and explain the setup to acquire magnetic bearing constants. Conclusions and remarks are included at the end of the report.

SECTION 2.0

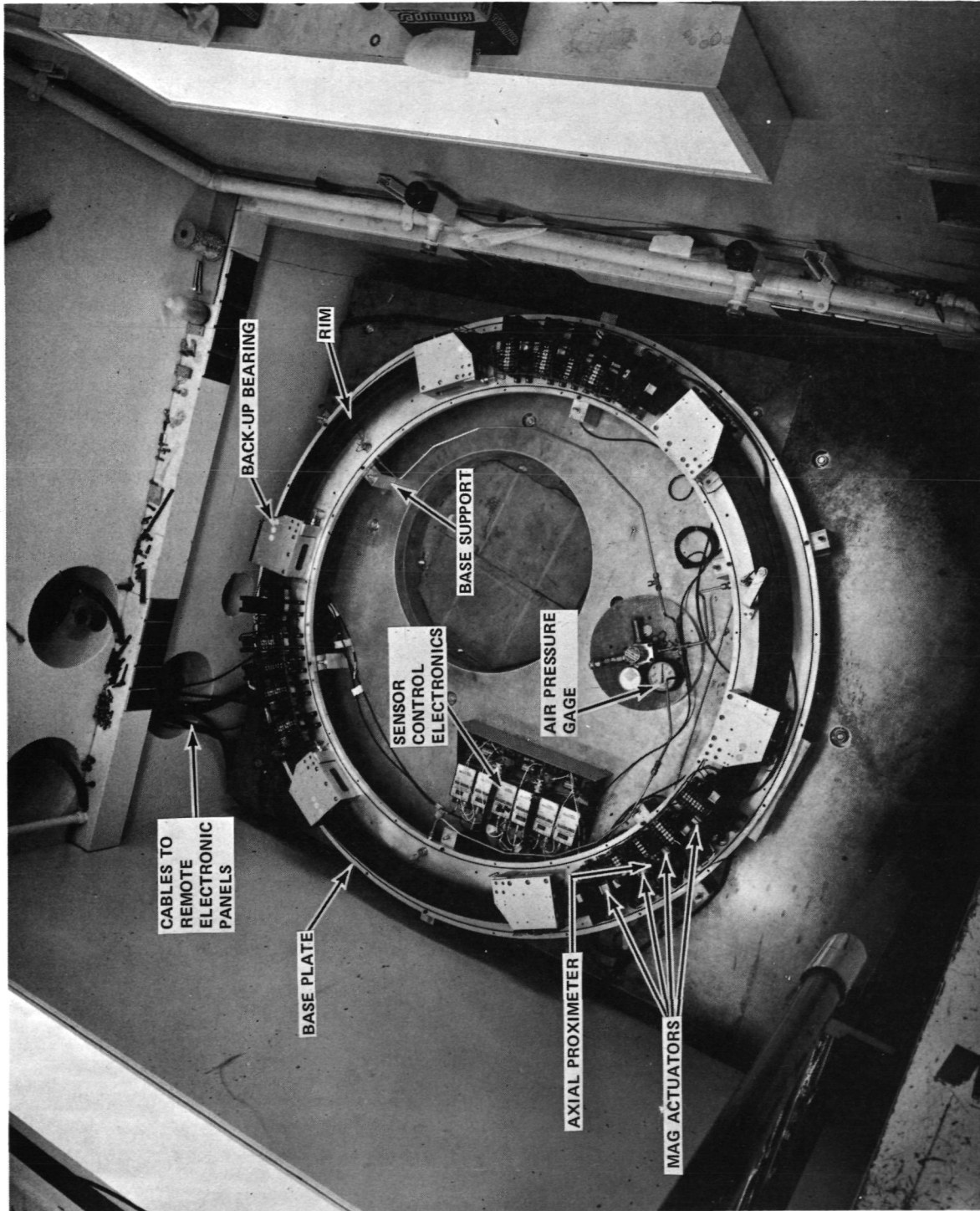
DESCRIPTION OF THE SYSTEM

The laboratory test model AMCD consists of 1) a rim, 2) magnetic actuators, 3) a brushless dc motor, 4) a support structure, 5) sensors, 6) a backup air bearing system, 7) a vacuum system and 8) an electronics drive and control system. A photograph of the layout of the test model is shown in Figure 1.

The basic setup includes a 1.6-meter diameter rim made of graphite-epoxy composite material. The rim is held in place and contained by three actuator stations. Each station has three complete sets of magnetic actuators, upper axial, lower axial and radial, and two sets of backup air bearing and braking sections. Each station has a set of radial and axial rim position sensors which provide the loop feedback information. All stations are mounted on an aluminum circular plate which, in turn, is firmly anchored to a flat and stable floor. Each backup air bearing station is connected to a high pressure air cylinder through a controlled solenoid valve system. The whole assembly can be covered with an air tight cover and can be depressurized for high speed testing.

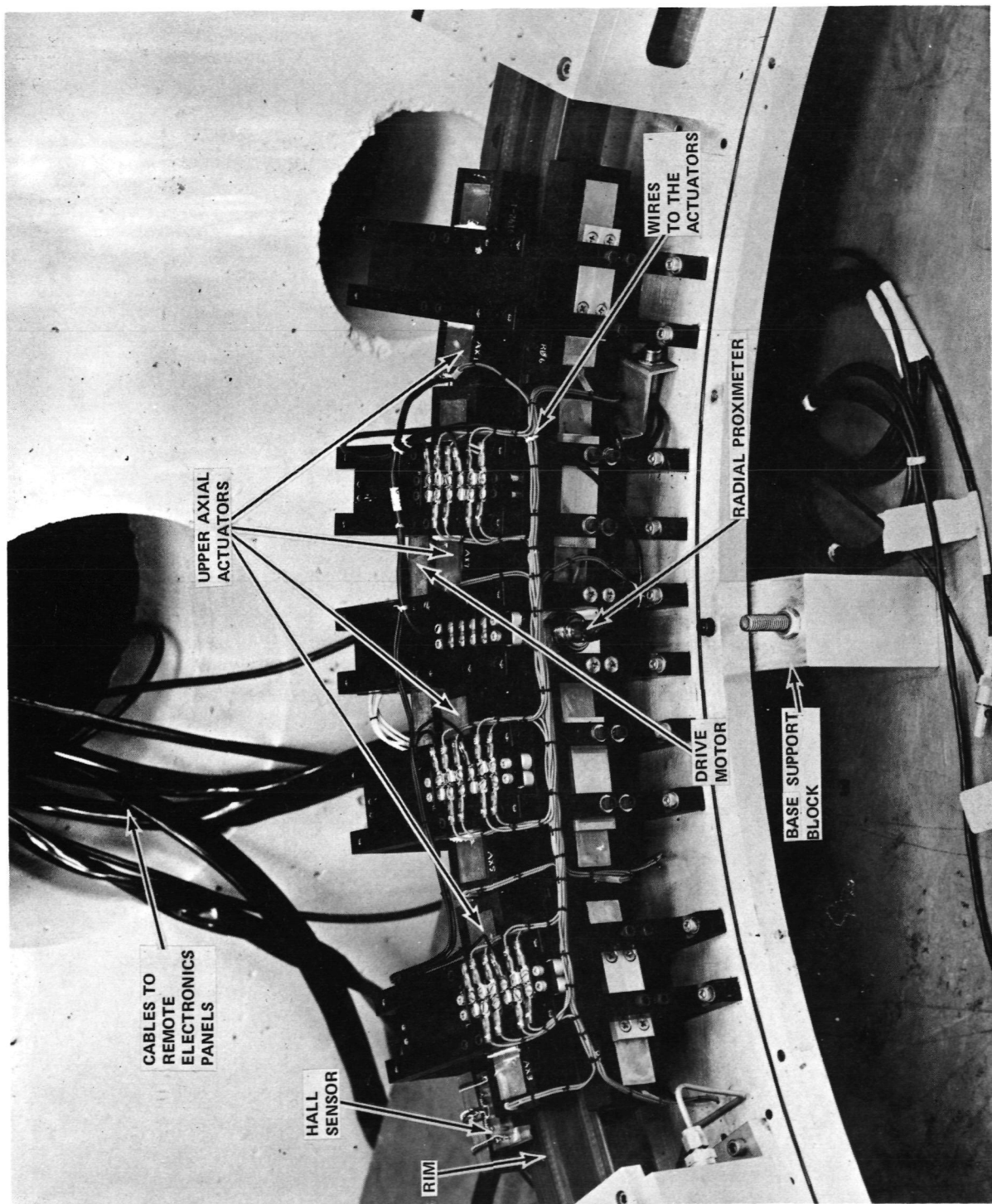
The rim is suspended in a magnetic field created by the magnetic actuators. Each actuator can only attract the rim. Therefore, the rim can be suspended in free space at a predetermined distance from each actuator set. Once the rim has been suspended and centered, the brushless dc drive motor (mounted on the outer periphery of each station) can accelerate the rim to a desired speed. A Hall sensor is used to commutate the motor and to measure the speed of the rim (see Figure 2). There are 72 equidistant permanent magnets imbedded in the outer periphery of the rim. As each magnet passes under the Hall sensor a pulse is generated. The frequency of the pulses is used to calculate the speed of the rim.

A backup air bearing system is used to support the rim in the event of a magnetic suspension system failure. Preset trip points are used to trigger the air bearing system into operation. When the rim is operated at speeds higher than 100 r/min, the assembly is covered with the airtight lid, and the housing is then depressurized. This evacuation reduces the air drag on the rim. Measurement of rim displacement and rotational speed level are routed to a



8-13167-4 R1

Figure 1
Laboratory Test Model 1 AMCD Layout



8-13167-3 R1

Figure 2
Section 3 MBA and the Hall Sensor

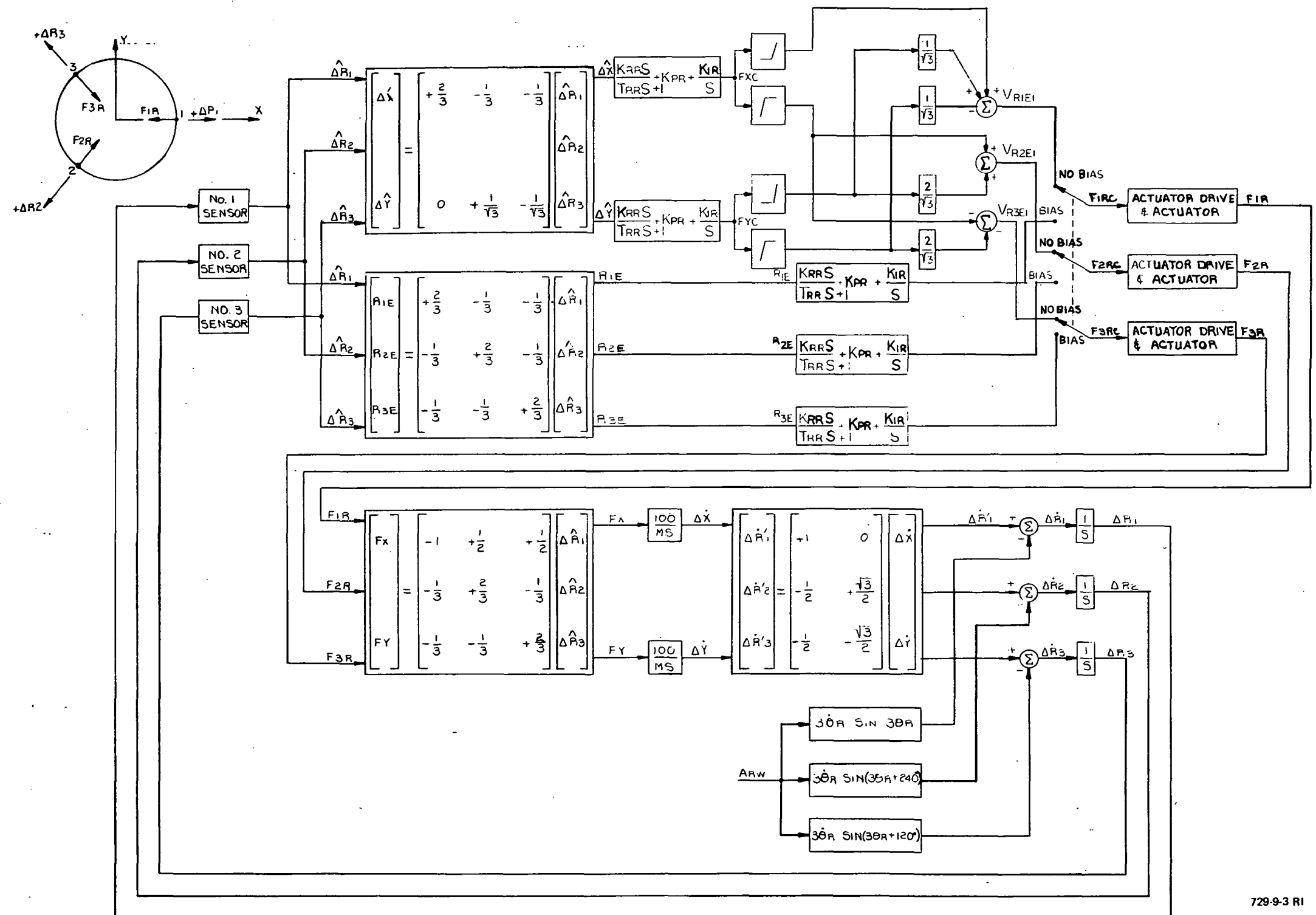
remotely-positioned electronic control station where the signals are processed and analyzed, and command signals are generated to control the rim. Appropriate magnetic actuators are given a gap-compensated current command to balance any displacement errors that occur.

No magnetic coupling exists between the radial and axial actuators. Therefore, radial control loops and axial control loops are independent from one another. Figures 3 and 4 illustrate the radial and axial control loop block diagrams, respectively. Detailed design and description of control system is given in Reference 1.

In Figure 3, three radial gap errors, ΔR_1 , ΔR_2 and ΔR_3 are sensed by the radial proximeters and are used to compute radial displacement errors ΔX and ΔY , the translation of the wheel along the X and Y axes. In order to control the wheel, compensation force commands F_{1RC} , F_{2RC} and F_{3RC} are generated, converted to control currents and routed to the three radial actuator stations. Forces F_{1R} , F_{2R} and F_{3R} are applied to the rim by the radial magnetic actuators and force the rim to move to the desired position.

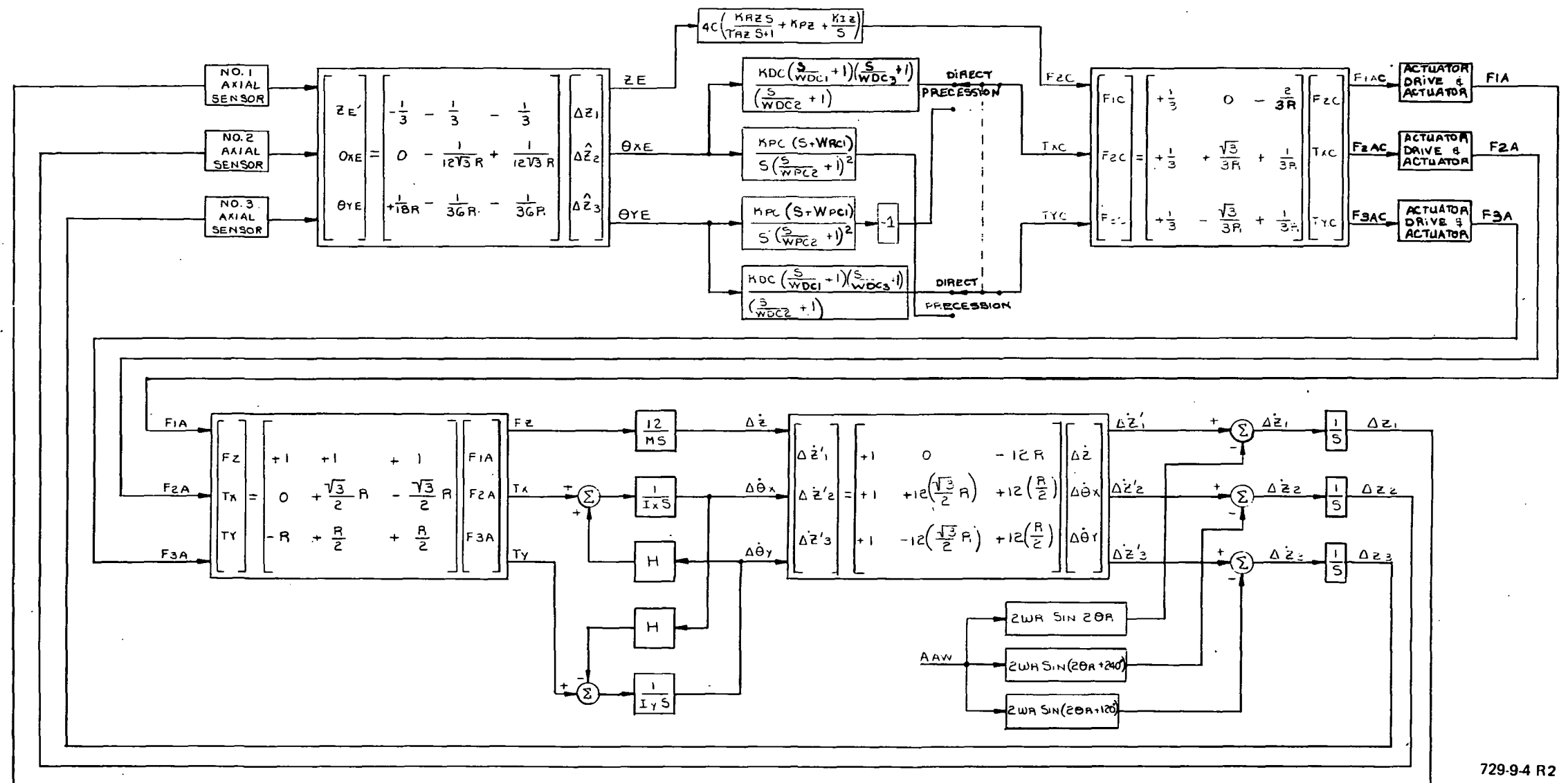
In Figure 4, three axial gap errors ΔZ_1 , ΔZ_2 and ΔZ_3 are sensed by the axial proximeters and are used to compute the axial displacement, ΔZ , as well as the tilt of the rim: θ_{XE} about the X axis and θ_{YE} about the Y axis. In order to center and level the rim, compensating current commands I_{1AC} , I_{2AC} and I_{3AC} are generated and routed to three axial stations. Forces $\pm F_{1A}$, $\pm F_{2A}$ and $\pm F_{3A}$ are applied by the axial magnetic actuators and force the rim to move to its desired position. Figure 5 shows the dynamic model of the magnetic actuators, both axial and radial.

Electronic Servo Compensation was designed for a 28-hertz closed-loop bandwidth for the radial loops (ΔX and ΔY), 16-hertz closed-loop bandwidth for torsional loops (θ_{XE} and θ_{YE}) and 16-hertz closed-loop bandwidth for the axial loop (ΔZ). These bandwidths were required to stabilize the rim at zero speed.

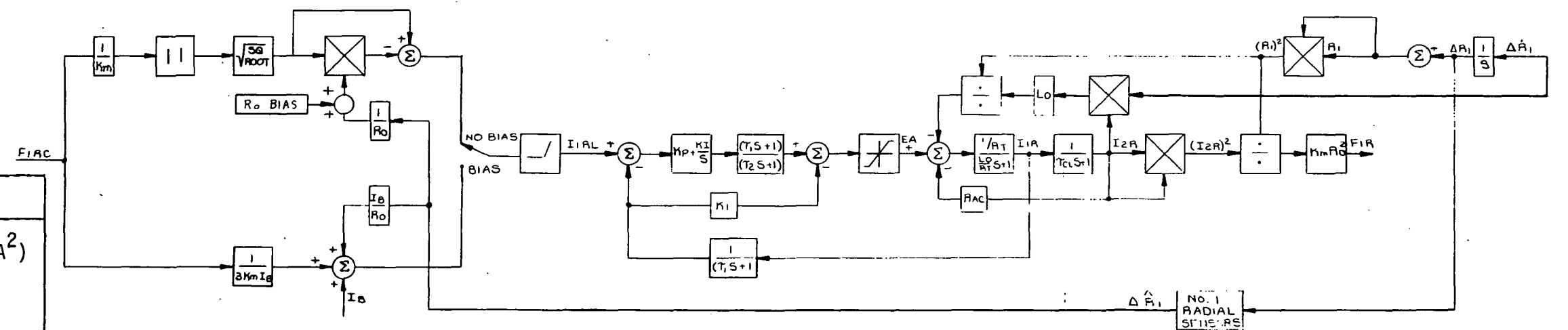
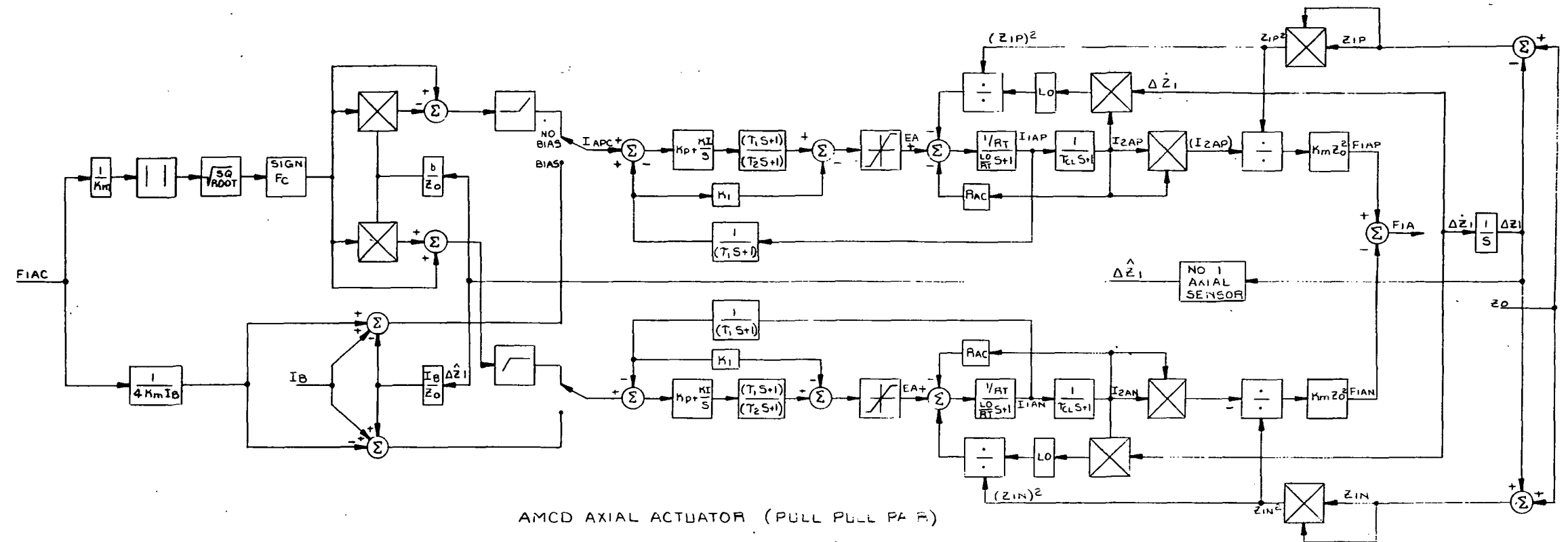


729-9-3 RI

Figure 3
Radial Actuator Control System
Dynamic Model



9



Parameter	Value	Units
Km	2.697 (.605)	N/A ² (lb/A ²)
I _b	1.76 (nominal)	A
Z ₀ = .1" R ₀ = .2"	.254 (.1)	cm (in.)
K _P	1000.	V/A
K _I	10 ⁶	V/(s·A)
K ₁	320.	V/A
τ ₁	.00075	s
τ ₂	10 ⁻⁵	s
L ₀	.335	H
R _T	324	Ω
R _{AC}	319.	Ω
τ _{CL}	.000751	s

Figure 5
AMCD Actuator Dynamic Models

2.1 OBJECTIVES

The main objectives of the program were:

- To achieve 2740-r/min rim speed.
- To learn the behavior of annular momentum storage elements suspended in a magnetic field.
- To suggest methods of improving such a device for possible future applications.

During the development and testing periods of the AMCD, much useful experience and information were gained. These achievements are explained in the remainder of this report and are summarized in Section 4.4.

SECTION 3.0
DATA COLLECTION

The following equipment was used for the collection of data at zero- and 500-r/min rim speeds.

- Two 8-channel strip-chart recorders
- Hewlett-Packard Analyzer, Model No. SD104 L-5 and SD101B
- Hewlett-Packard Gain/Phase Meter, Model No. 3575A
- Two X-Y plotters

Figures 6 and 7 illustrate the schematic test setup for collecting data for both step and frequency response of the system in "open-loop" and "closed-loop" modes, respectively. Because of the nature of the system, data for "open-loop" mode was collected indirectly in the "closed-loop" mode, as shown in Figure 6.

$$\text{Open-loop transfer function} = \frac{C}{E}, \quad (1)$$

$$\text{but } \left| \frac{C}{E} \right|_{\text{db}} = \left| \frac{C}{R} \right|_{\text{db}} - \left| \frac{E}{R} \right|_{\text{db}} \quad (2)$$

Therefore, frequency response of the transfer functions C/R and E/R were plotted, and the response of C/E was derived according to Equation (2). Similarly, the phase of the transfer function C/E was derived using Equation (3).

$$\left| \frac{C}{E} \right|_{\phi} = \left| \frac{C}{R} \right|_{\phi} - \left| \frac{E}{R} \right|_{\phi} \quad (3)$$

Frequency response testing was limited to 80 Hz to avoid a system resonance at about 90 Hz. During testing, two eight-channel strip chart recorders were used to monitor the system status. Signals ΔR_1 , ΔR_2 , ΔR_3 , ΔX , ΔY , ΔZ_1 , ΔZ_2 , ΔZ_3 , Z_E , θ_{XE} , θ_{YE} and rim speed were recorded. A sample of the recording is shown in Figure 8.

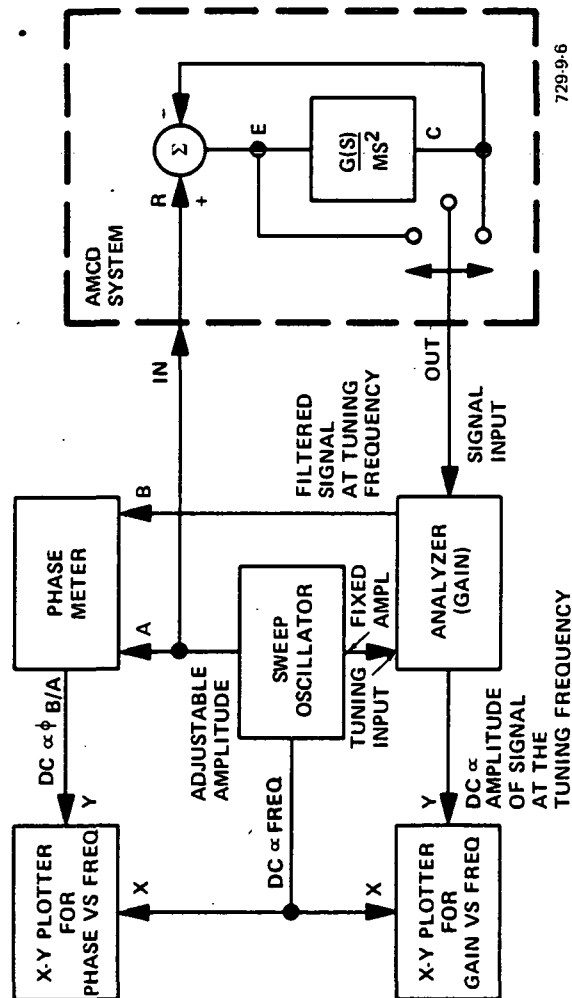


Figure 6
Setup for Open-Loop Frequency Response

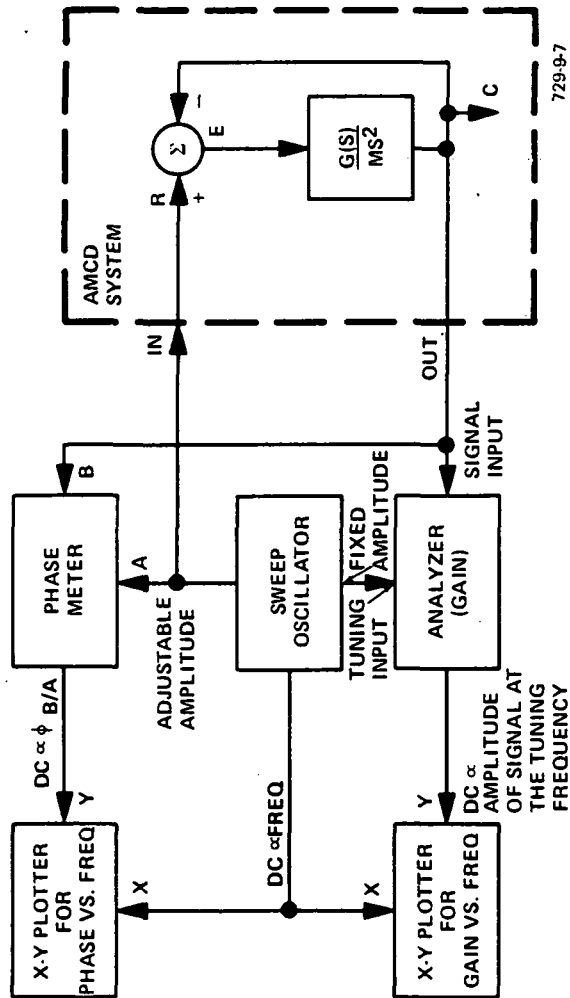
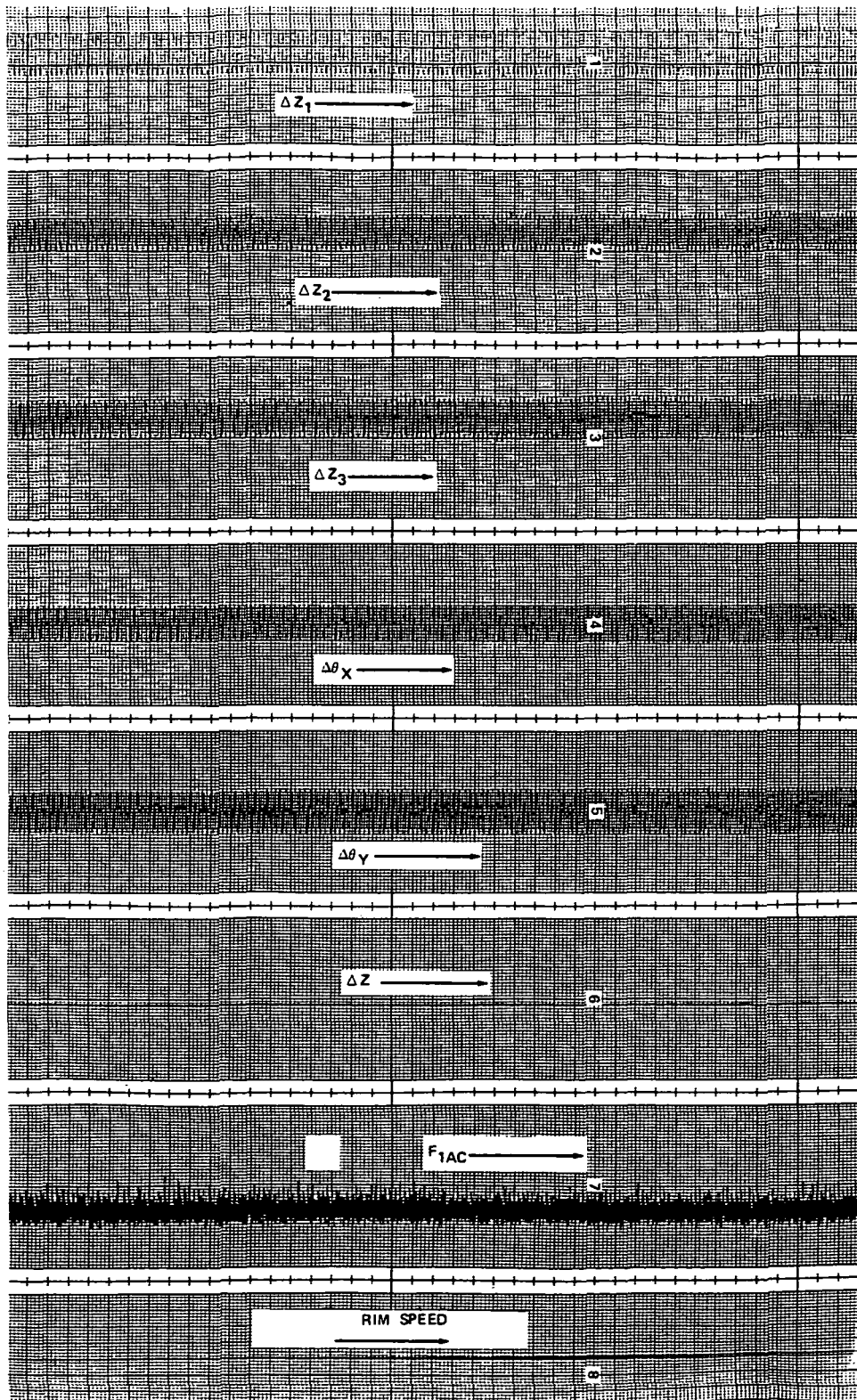


Figure 7
Setup for Closed-Loop Frequency Response



729-9-8 RI

Figure 8
Sample Recording

3.1 IMPORTANT MILESTONES ACHIEVED

During the development of AMCD, a number of important milestones were achieved. These are listed below in chronological order.

1. System Suspension Assembly completed and checked out using
 - a) laboratory equipment
 - b) analog computer feedback response
2. Raised servo bandwidth and achieved stable operating system.
 - a) New suspension electronics and magnetic actuators designed and installed
 - b) Actuator and suspension system control techniques established
3. Replaced radial sensors and redesigned mounting brackets.
 - a) Eliminated structural resonance
4. Determined that electromagnetic coupling effects existed between proximeters.
 - a) Slaved all position sensors to a common excitation and eliminated error response
5. Established K^* and b^* electromagnetic force constants for actuators, using:
 - a) independent force fixture
 - b) system test technique
6. Remounted baseplate support system to eliminate outside structure resonances.
7. Leveled support system within .001 inch (.00254 cm)
8. Balanced rim by adding lead tape to rim.
 - a) A total of 24 grams was added to achieve mass balance.

*See Page 51 for definition.

9. Performed zero-speed response tests
10. Performed 500-r/min response tests
11. Achieved 725-r/min velocity
12. Performed system analog computer simulation
 - a) verified system responses
 - b) predicted precessional responses - model did not account for actuator positional mismatches
13. Attempted precessional switchover - unsuccessfully
14. Summarized results
 - a) operation manual
 - b) test report.

Page Intentionally Left Blank

SECTION 4.0

INTERPRETATION OF COLLECTED DATA

Experimental data collected is divided into two main categories; zero speed characteristics and 500-r/min characteristics.

4.1 DATA COLLECTED AT ZERO R/MIN

Zero speed data was obtained for both step response and frequency response of the system.

4.1.1 Step Response at Zero R/Min

Figures 9, 10 and 11 illustrate step response at zero r/min of each loop; i.e. ΔX , ΔY , ΔZ , $\Delta \theta_x$, $\Delta \theta_y$ for both open-loop and closed-loop modes. The ΔX , ΔY and ΔZ loops are critically damped while θ_{xE} and θ_{yE} loops have a damping ratio of .45. Rise time for the loops is less than .1 second. The step response data for closed-loop mode is tabulated in Table 1.

4.1.2 Frequency Response at Zero R/Min

Figures 12 through 16 disclose the closed-loop frequency response, and Figures 17 through 21 show the open-loop frequency response at zero r/min for each loop. Information pertinent to the frequency response is summarized in Table 1. The poles and zeros of the system are outside the loop bandwidths. The data indicates that the system is stable under the operating configuration chosen.

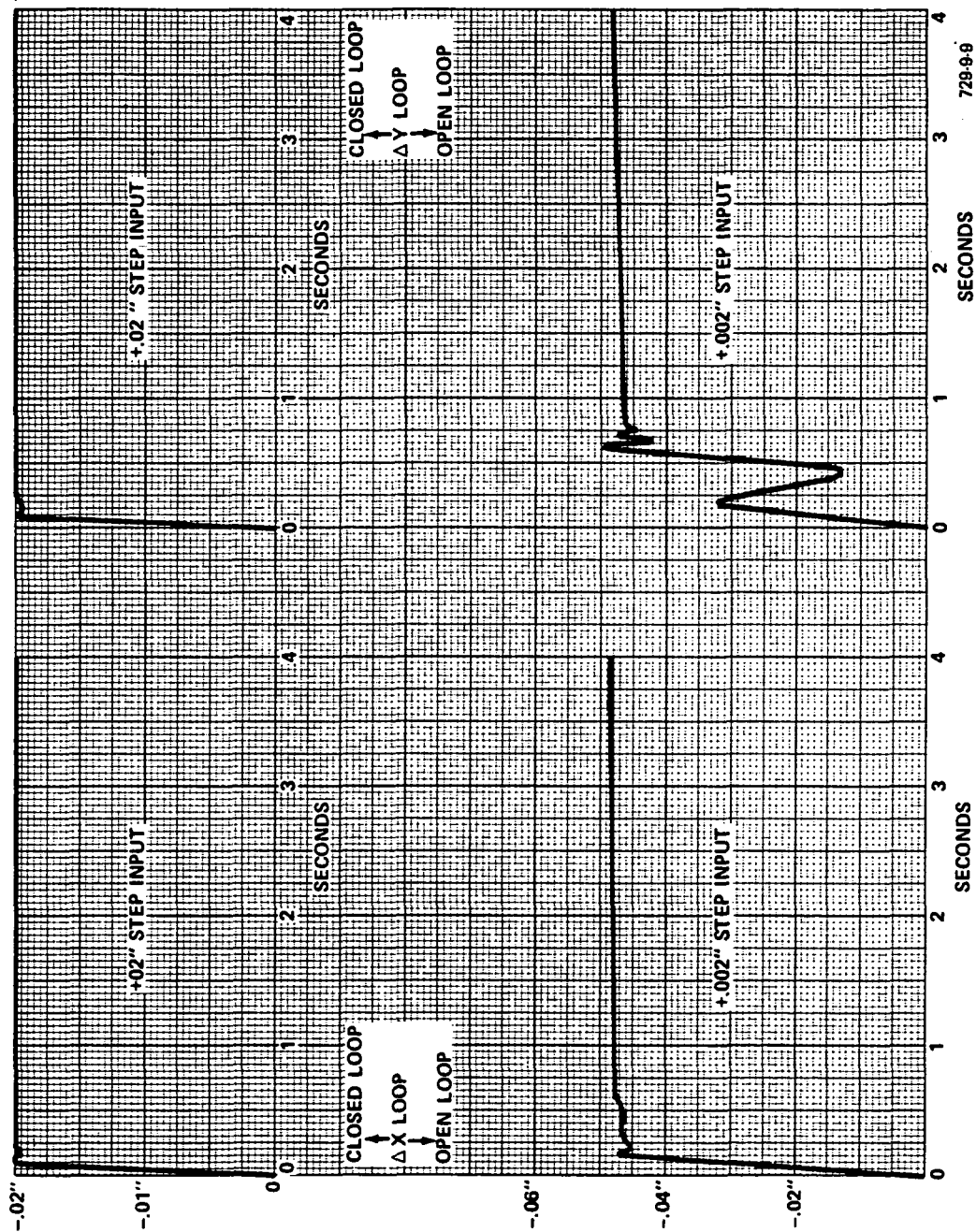


Figure 9
Step Response at Zero Speed
(ΔX , ΔY Loops)

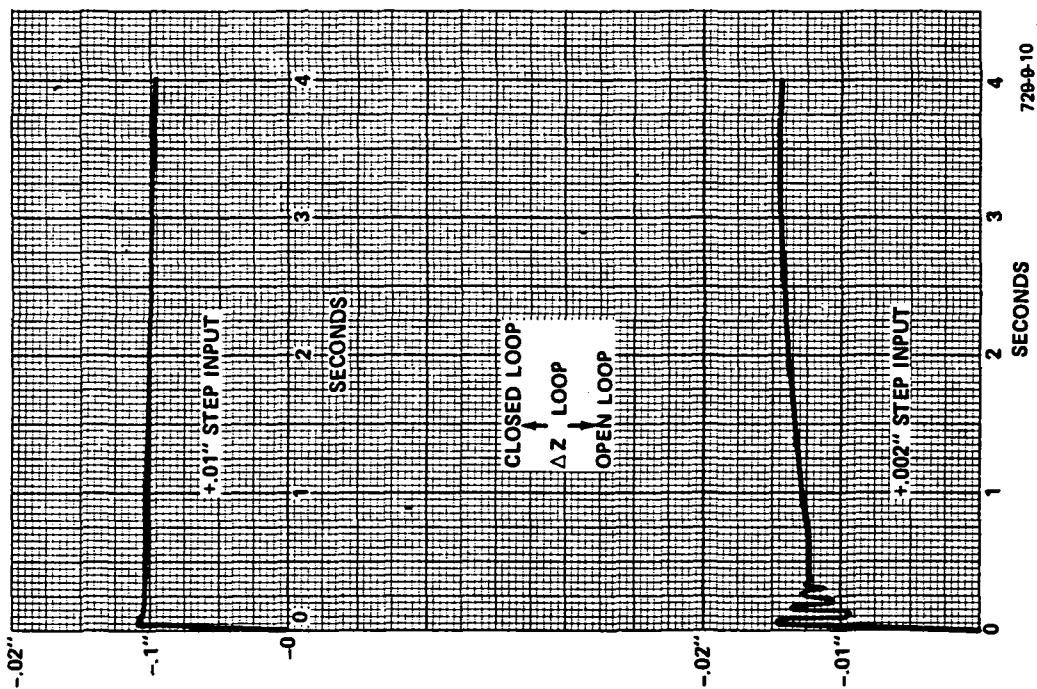


Figure 10
Step Response at Zero Speed
(ΔZ Loop)

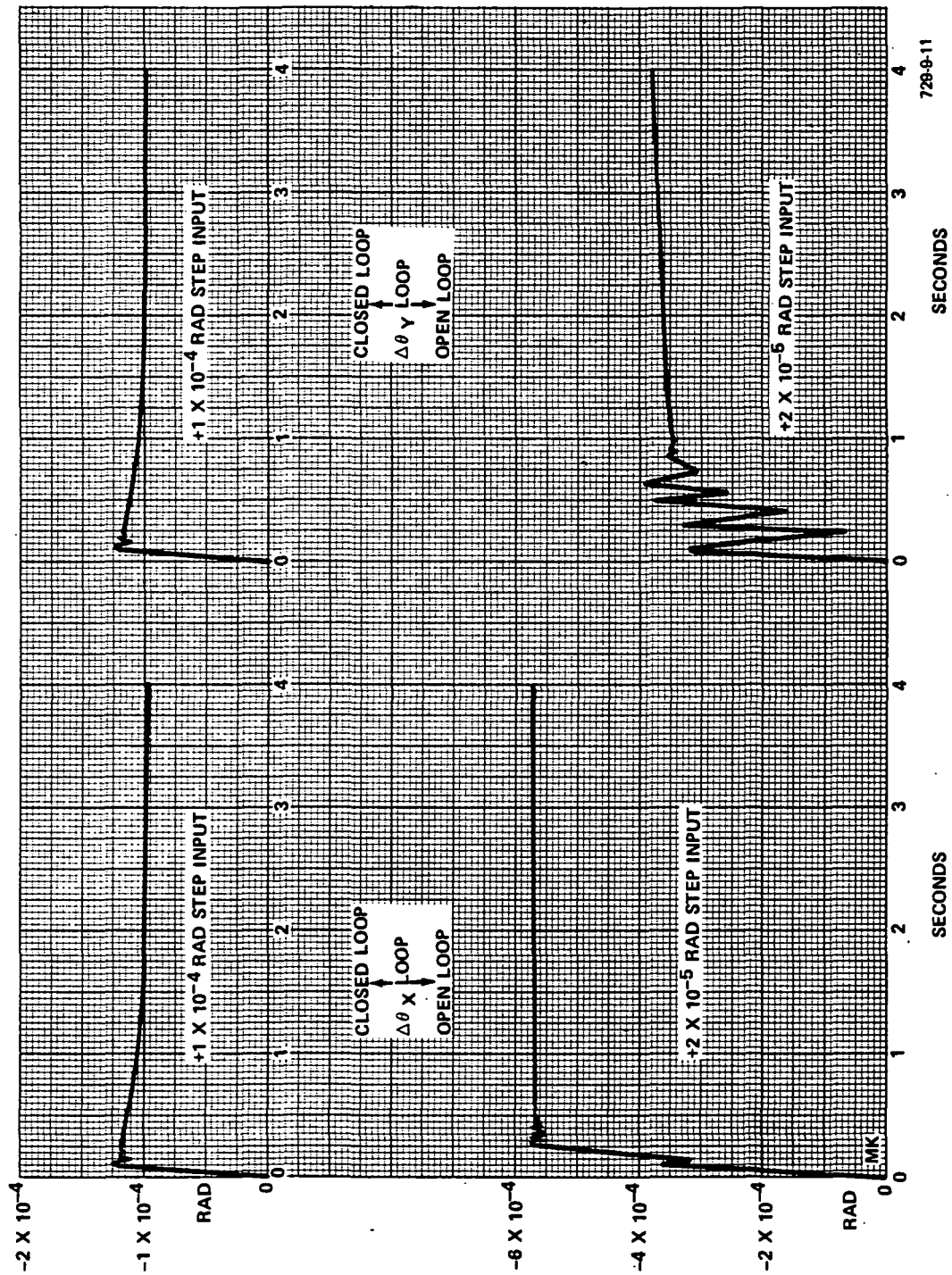


Figure 11
Step Response at Zero Speed
($\Delta\theta x$, $\Delta\theta y$ Loops)

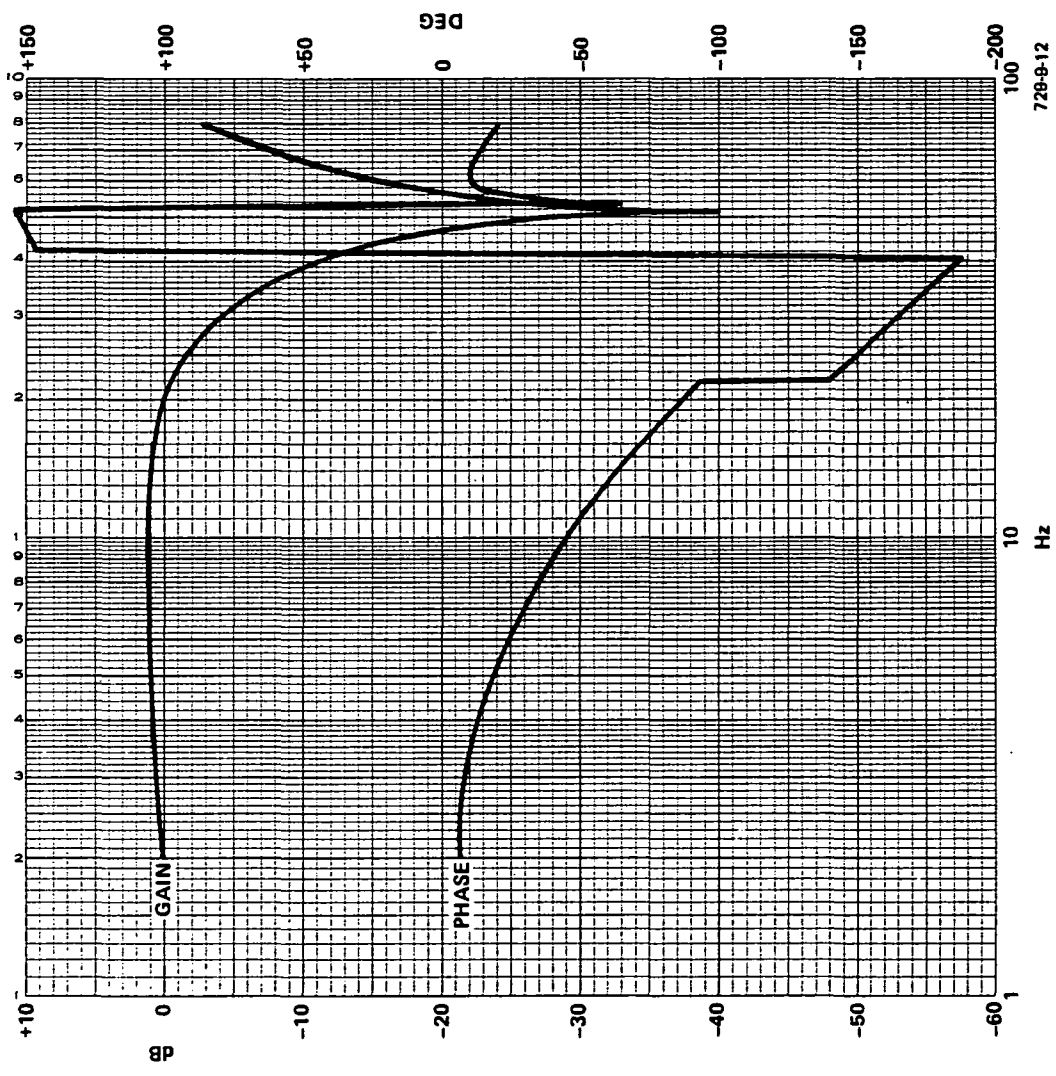


Figure 12
Closed-Loop Frequency Response at
Zero Speed for ΔX Loop

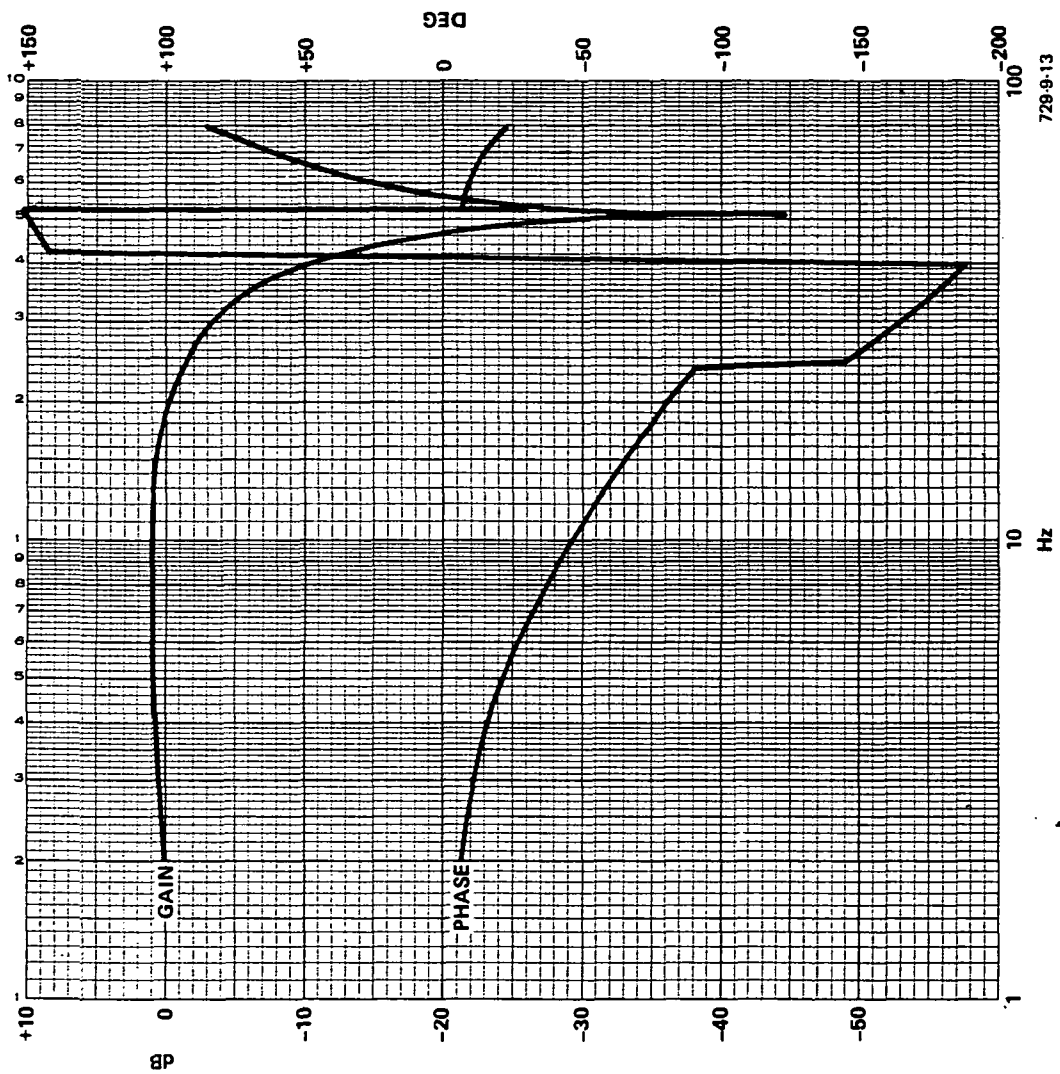


Figure 13
Closed-Loop Frequency Response at
Zero Speed for ΔY Loop

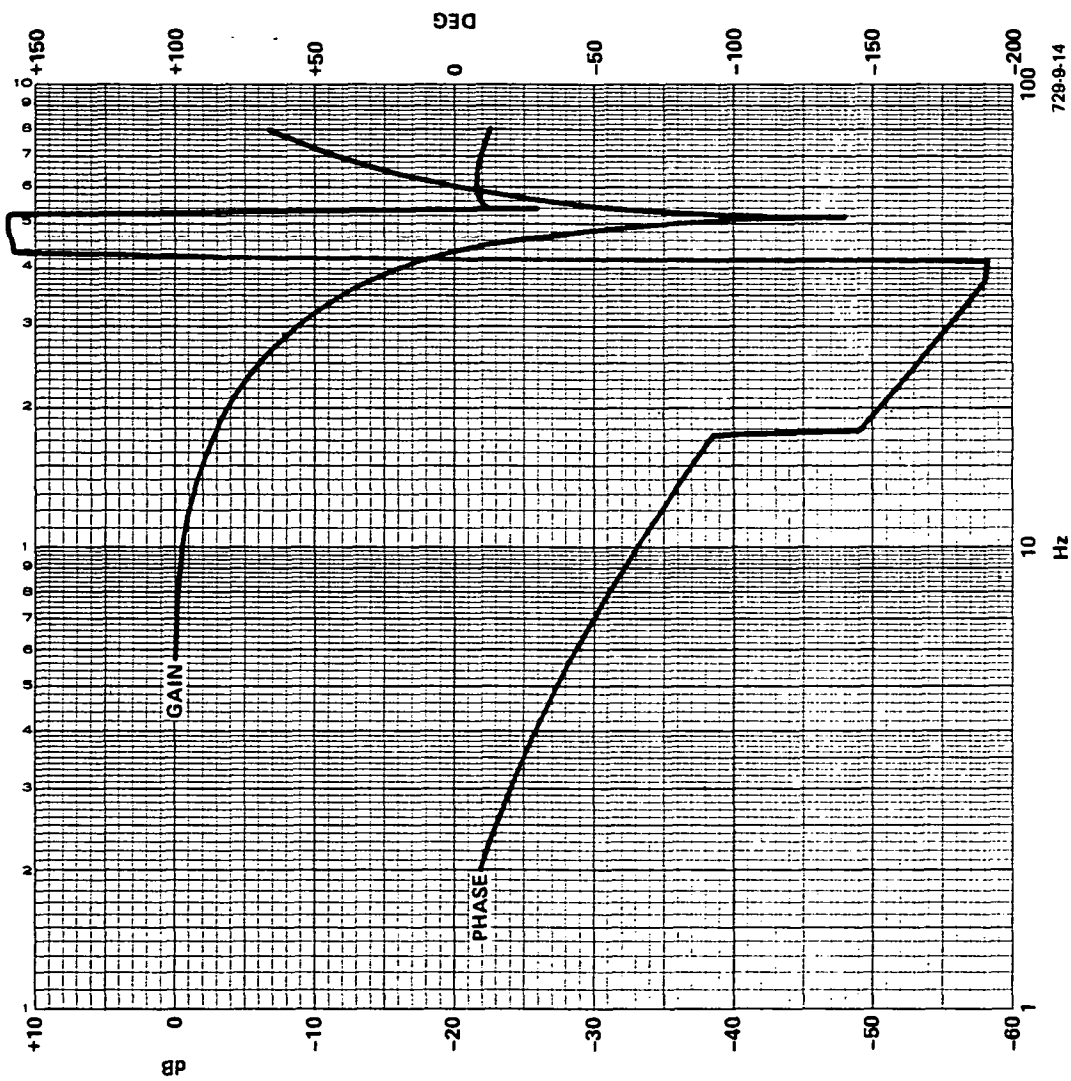


Figure 14
Closed-Loop Frequency Response at
Zero Speed for ΔZ Loop

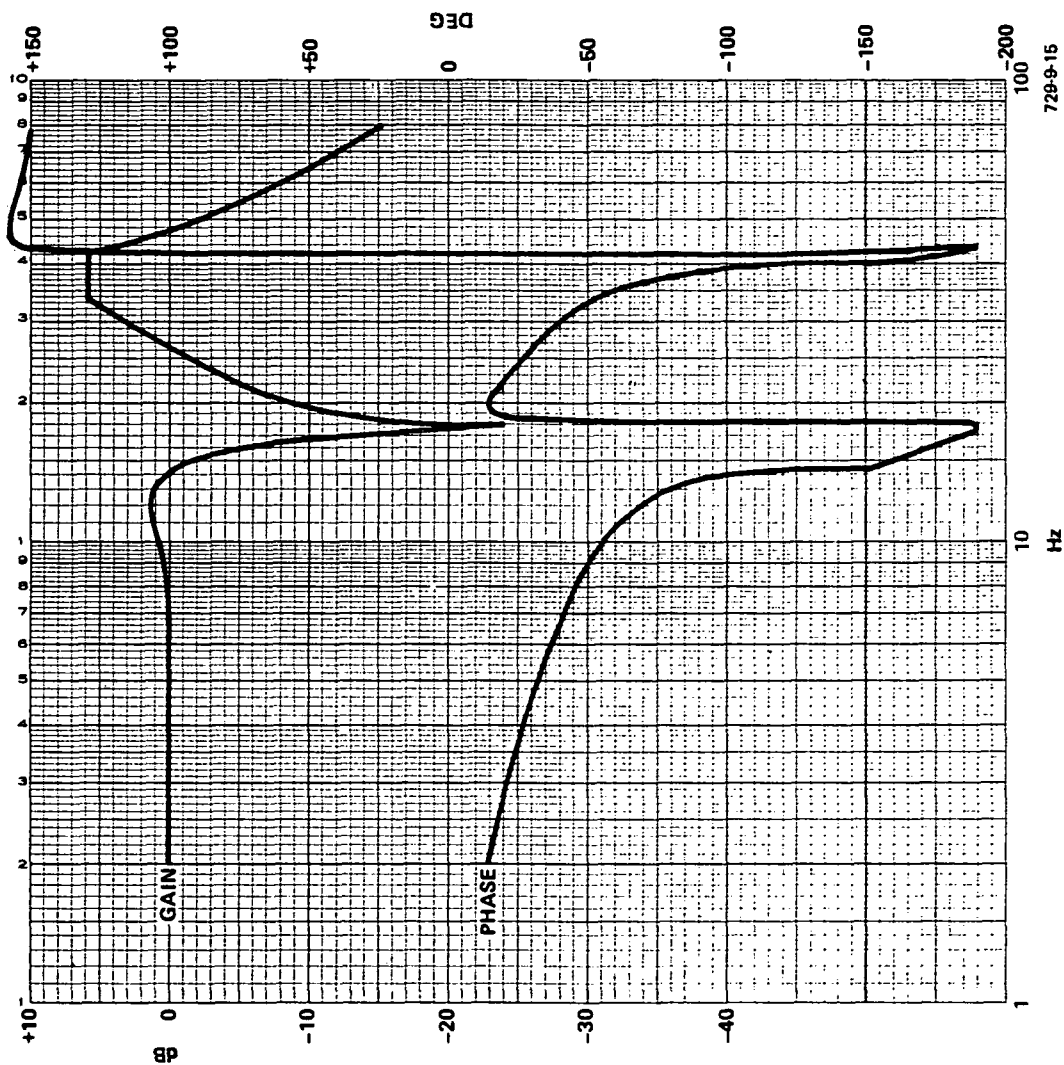


Figure 15
Closed-Loop Frequency Response at
Zero Speed for $\Delta\theta_x$ Loop

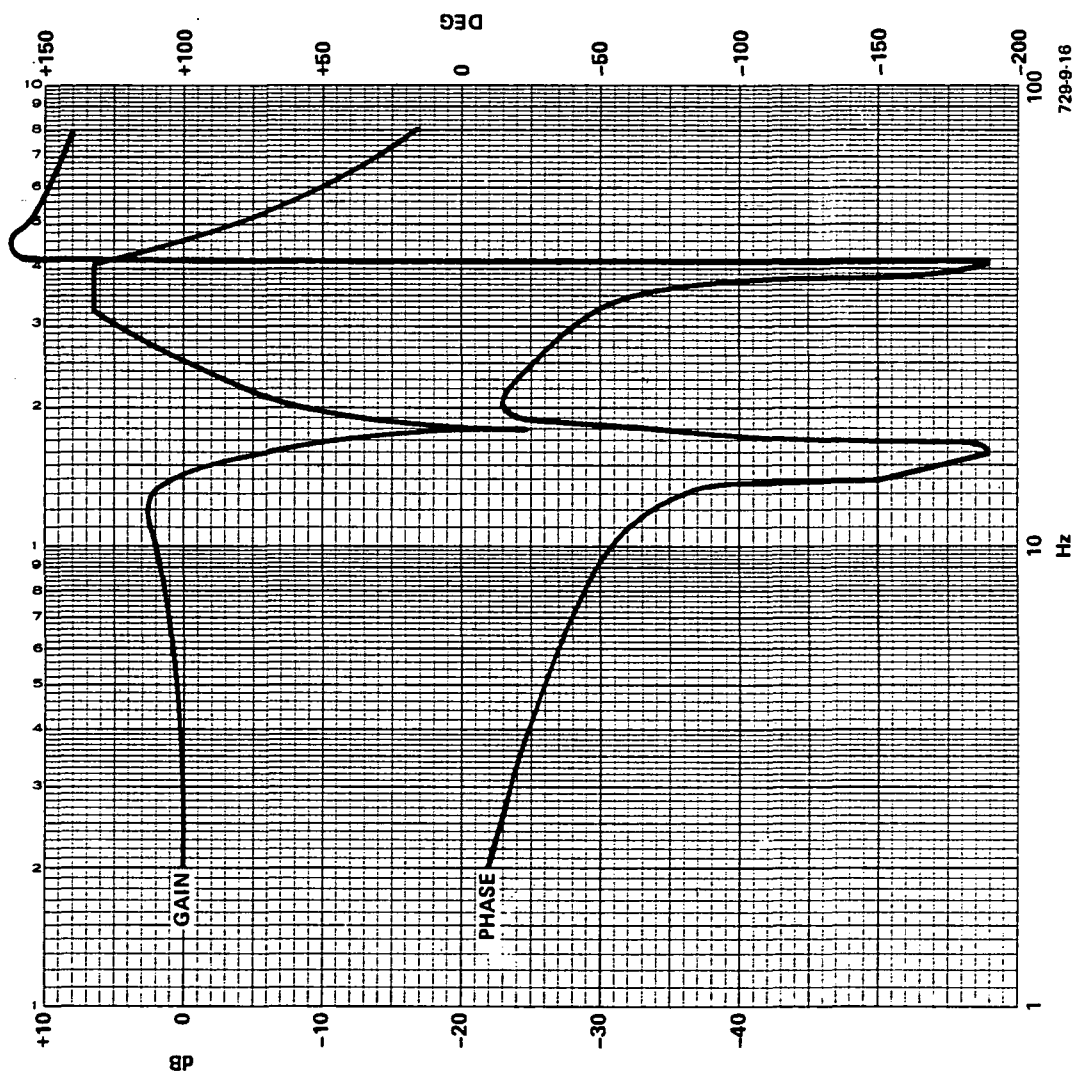


Figure 16
Closed-Loop Frequency Response at
Zero Speed for $\Delta\theta_y$ Loop

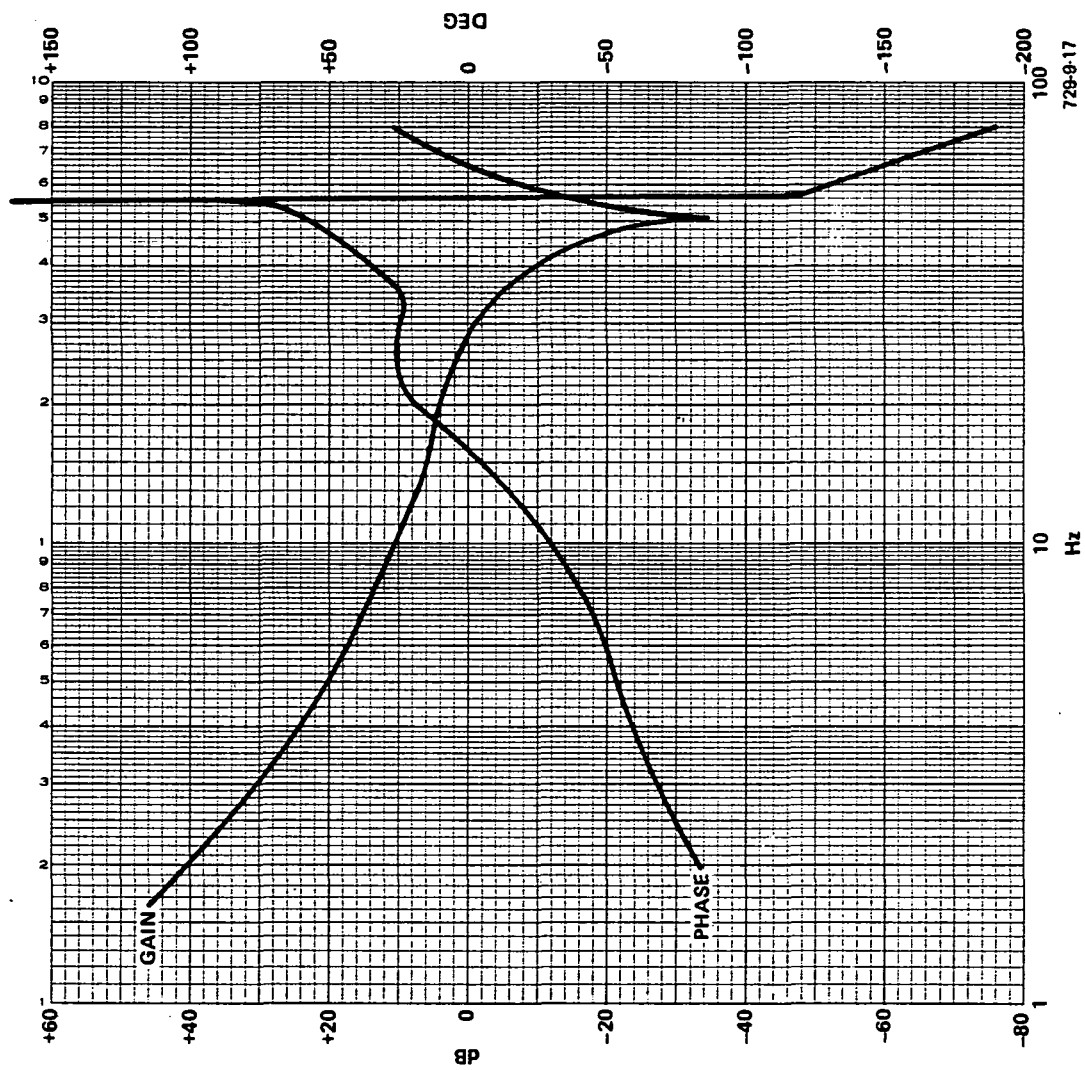


Figure 17
Open-Loop Frequency Response at
Zero Speed for ΔX Loop

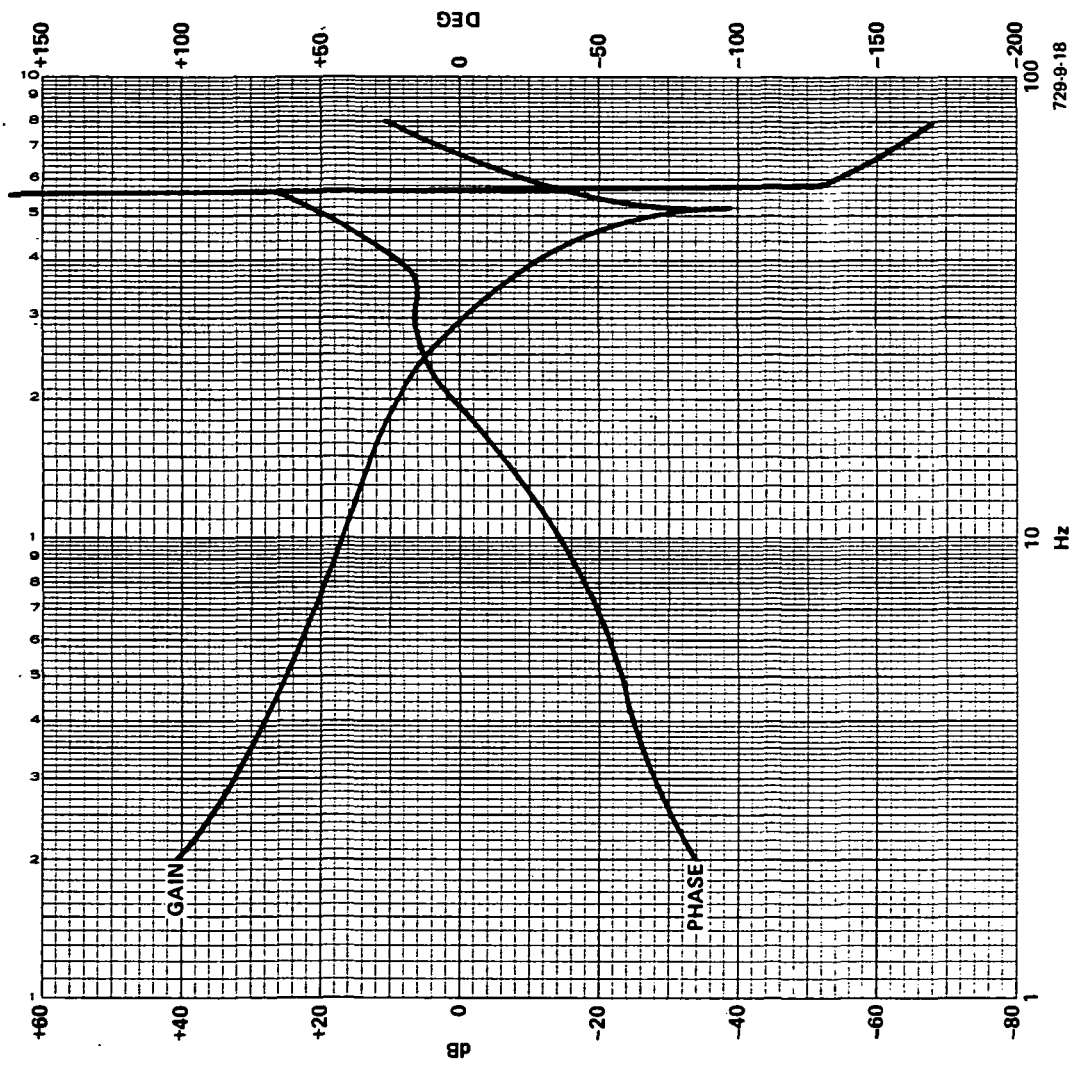


Figure 18
Open-Loop Frequency Response at
Zero Speed for ΔY Loop

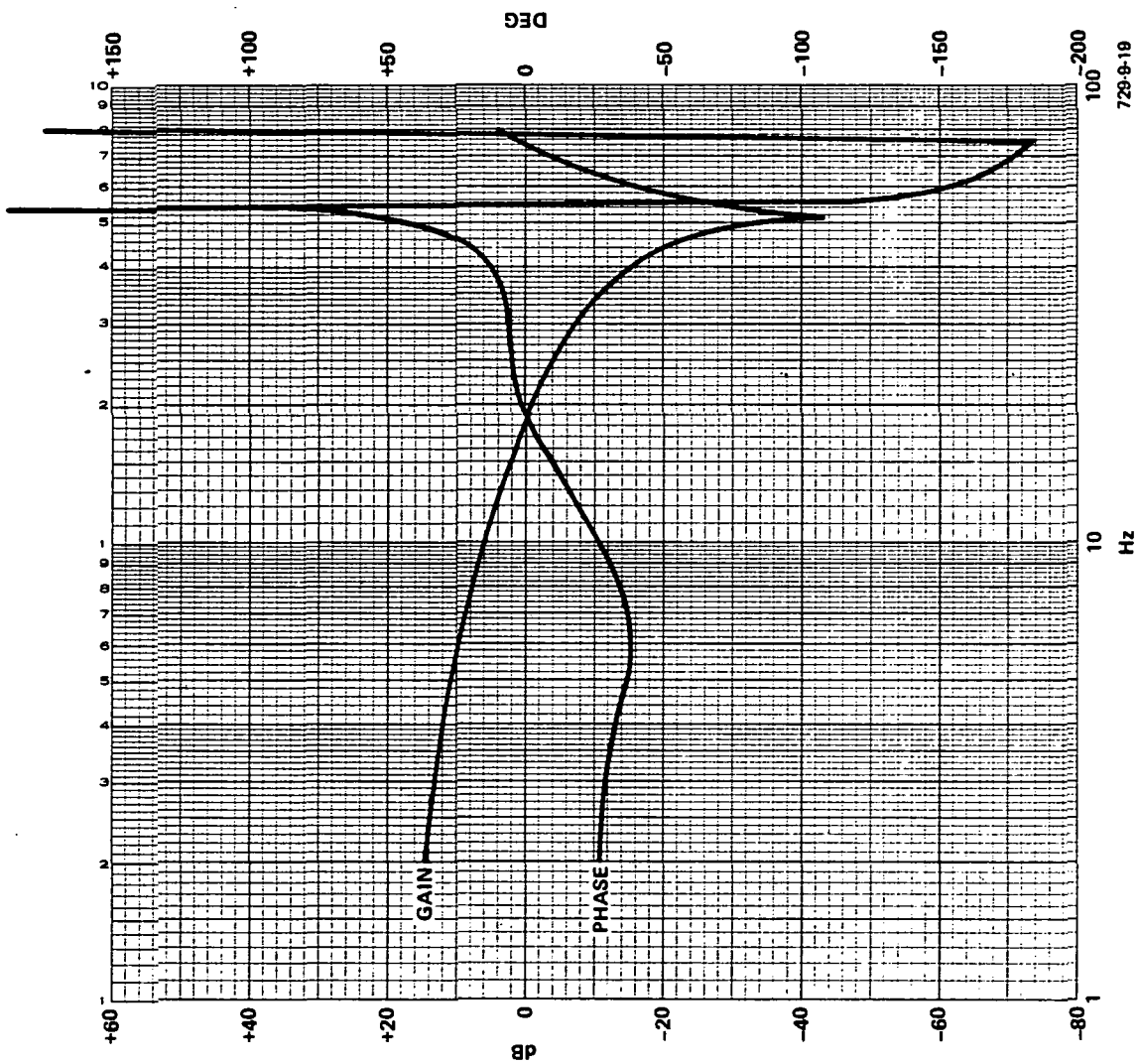


Figure 19
Open-Loop Frequency Response at
Zero Speed for ΔZ Loop

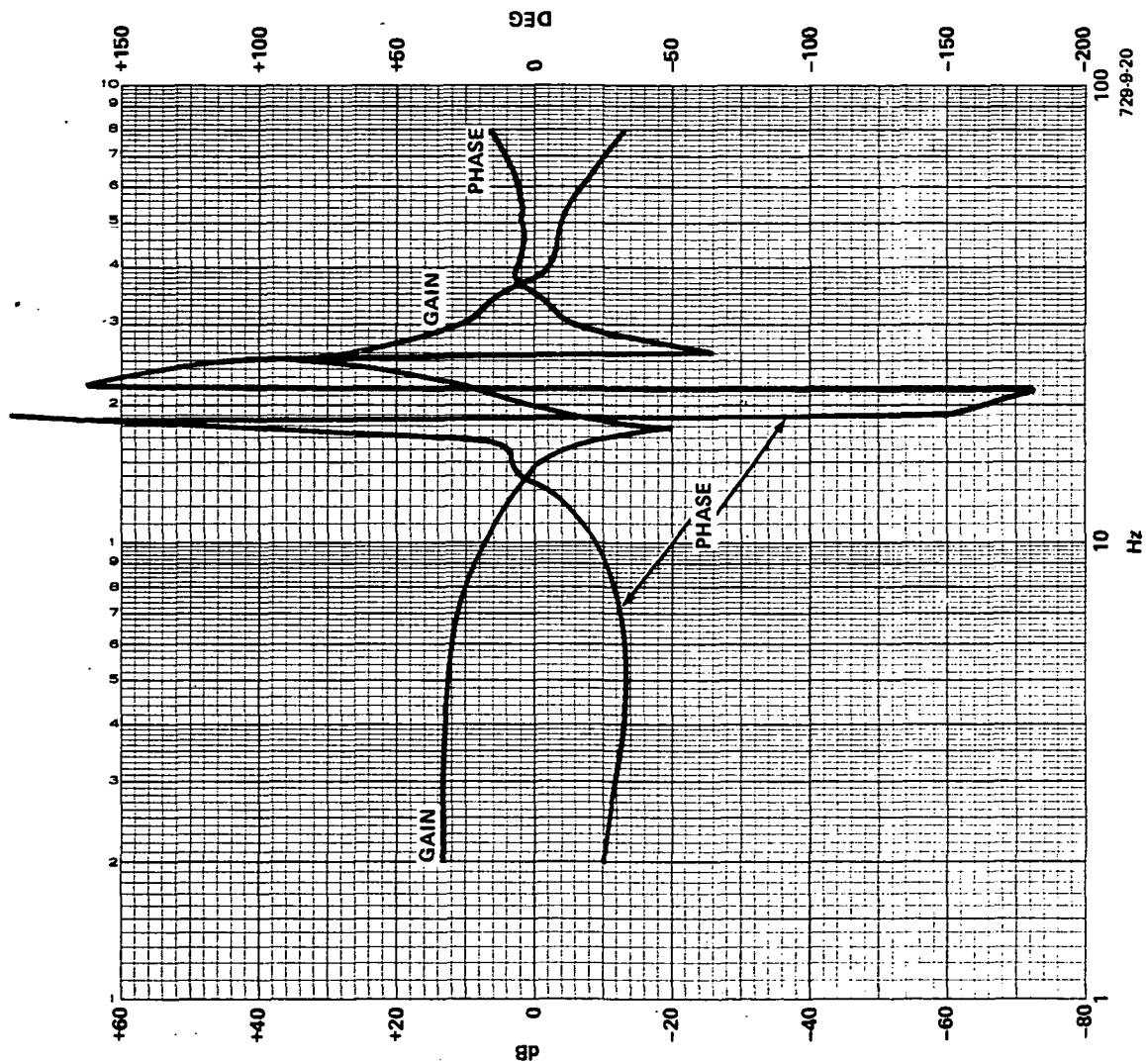
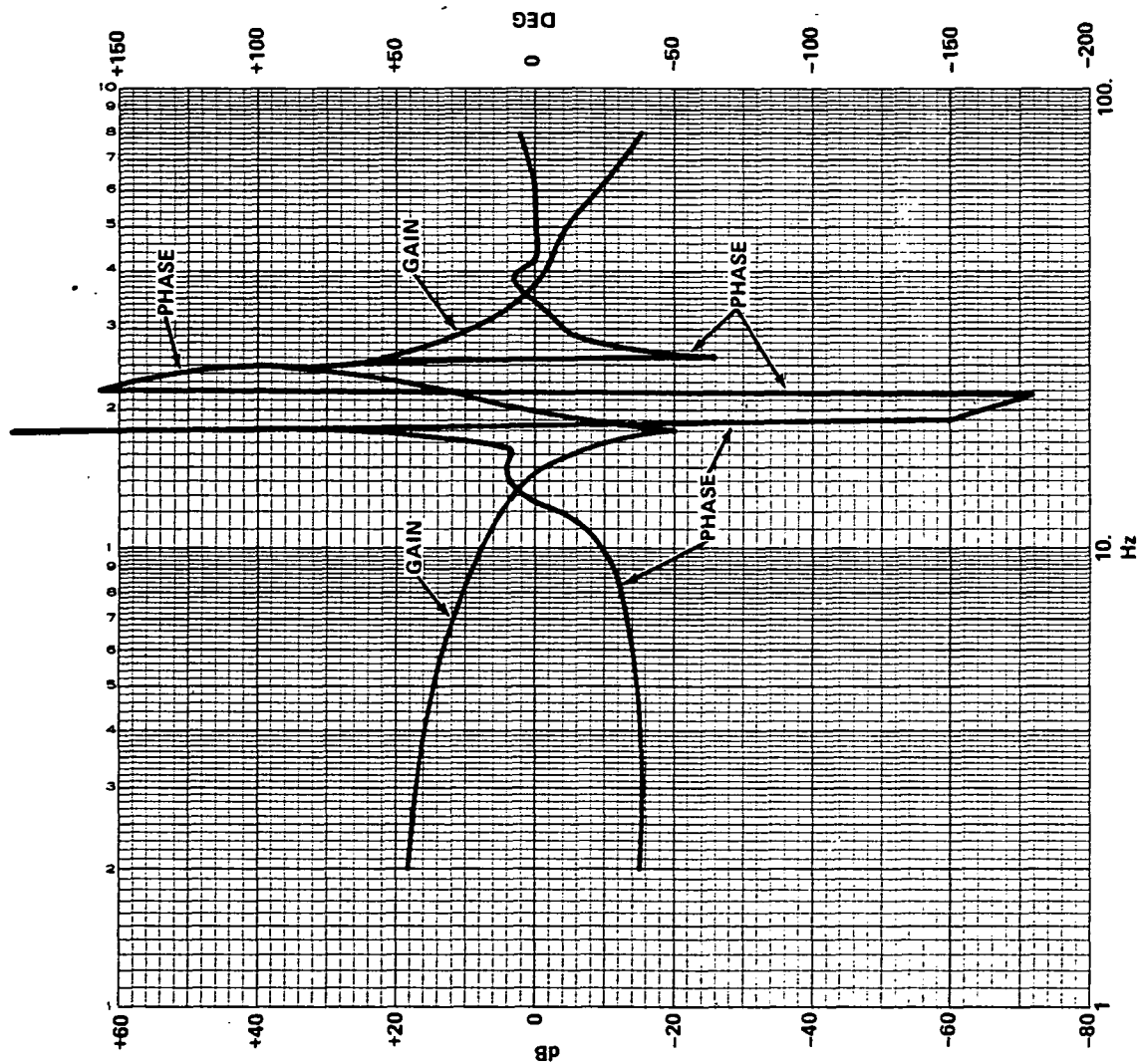


Figure 20
Open-Loop Frequency Response at
Zero Speed for $\Delta\theta_X$ Loop



729-9-21

Figure 21
Open-Loop Frequency Response at
Zero Speed for $\Delta\theta\gamma$ Loop

TABLE 1
AMCD CHARACTERIZATION AT ZERO R/MIN

Zero R/Min						
	Channel	OL	CL	Lowest		
		BW	BW	OL	CL	
		Hz	Hz	Zero	Pole	
				(Hz)	(Hz)	
FREQUENCY RESPONSE	ΔX	28	28	51	80+	
	ΔY	29	29	51	80+	
	ΔZ	18	18	51	80+	
	$\Delta \theta X$	15	15	18	25	
	$\Delta \theta Y$	15	15	18	25	
	Channel	Rise Time		Settling Time		Damping
		Tr		Ts		Ratio
		(sec)		(sec)		
CLOSED-LOOP STEP RESPONSE	ΔX	.1		.2		.7
	ΔY	.1		.2		.7
	ΔZ	.04		2.0		.69
	$\Delta \theta X$.04		1.5		.45
	$\Delta \theta Y$.07		1.5		.48

4.2 DATA COLLECTED AT 500 R/MIN

Five-hundred-r/min data was also determined for both step response and frequency response.

4.2.1 Step Response at 500 R/Min

Figure 22 illustrates 500-r/min step response of each loop for closed-loop mode. Open-loop step response cannot be obtained when the rim is turning. Even the lowest excitation, distinct from the noise, forces the rim to deviate from its center position so that the backup air bearing system is activated. Summary of the closed-loop step response at 500 r/min is given in Table 2. Rise time of the system is about .2 second. The system is sufficiently damped with damping ratios differing from loop to loop. The data indicates that the system is stable but not well damped.

4.2.2 Frequency Response at 500 R/Min

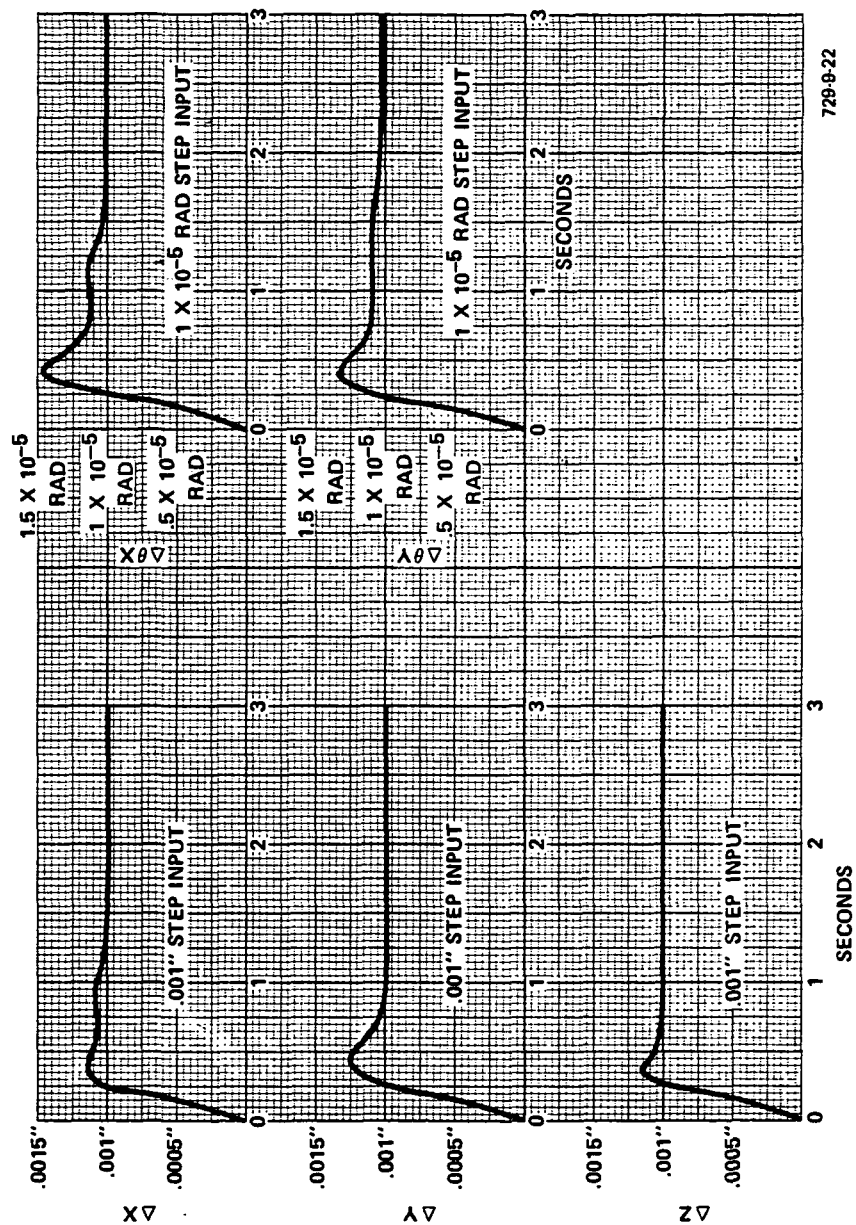
Figures 23 through 27 show the closed-loop frequency response, and Figures 28 through 32 show the open-loop frequency response at 500 r/min for each loop. Information pertinent to the frequency response is summarized in Table 2. Note the resonances at about 8.5 Hz and at frequency multiples of 8.5 Hz. As in the open-loop response, poles and zeros of the system are outside the system loop bandwidths. The data confirms that the system is stable at 500 r/min.

4.3 HIGHER SPEEDS

Testing disclosed that speeds in excess of 600 r/min were impractical using the system as originally configured.

A severe imbalance problem existed so that any response data was impossible to extract because of the unbalanced effects on the data.

A program was initiated to balance the rim. Appendix B describes the method employed and the results. The net result, however, was that a total of 24 grams was added to the outer periphery of the rim to achieve mass balance.



729-6-22

Figure 22
Closed-Loop Step Response at 500 R/Min

TABLE 2
AMCD CHARACTERIZATION AT 500 R/MIN

		500 R/Min						
	Channel	OL BW Hz	Lowest OL Zero (Hz)	Lowest OL Pole (Hz)	CL BW Hz	Lowest CL Zero	Lowest CL Pole	500 R/Min Resonance Frequencies Hz
Frequency Response	ΔX	29	51	80+	30	51	80+	8.5, 17, 33, 42, 58, 80+
	ΔY	28	51	80+	30	51	80+	8.5, 17, 33, 42, 58, 80+
	ΔZ	21	48	62	21	48	68	25, 50
	$\Delta \theta X$	8.9	18, 48	25	7.2	18, 48	37, 56	8.6, 17, 25, 33, 56
	$\Delta \theta Y$	9.8	16, 33	25	9.8	18, 50	37, 58	8.6, 17, 36, 58
		Rise Time Tr (sec)		Settling Time Ts (sec)		Damping Ratio		
Closed-Loop Step Response	ΔX	.2		1.5		.5		
	ΔY	.2		.9		.45		
	ΔZ	.2		.9		.5		
	$\Delta \theta X$.2		1.65		.35		
	$\Delta \theta Y$.2		1.95		.44		

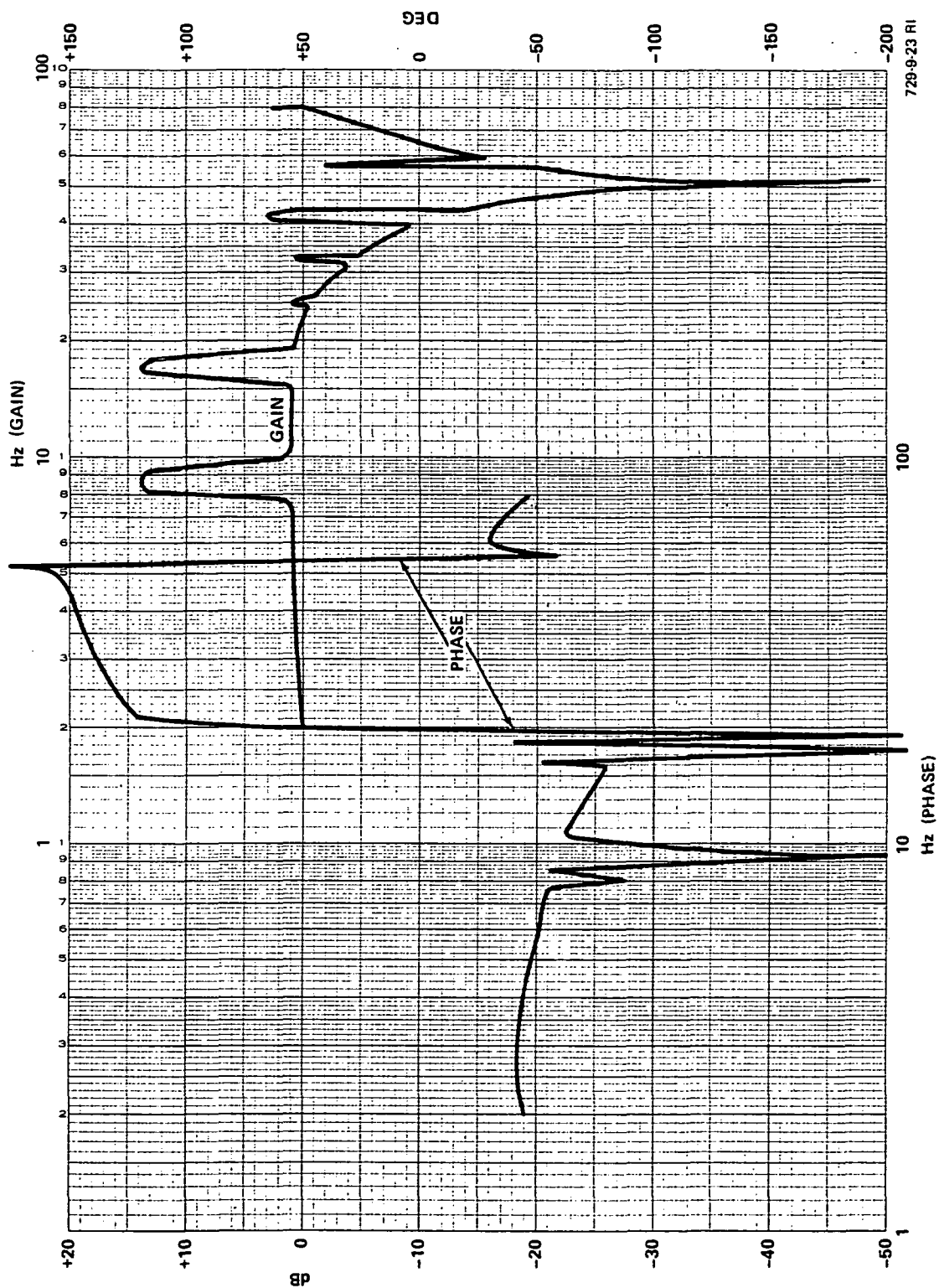


Figure 23
Closed-Loop Frequency Response at
500 R/Min for ΔX Loop

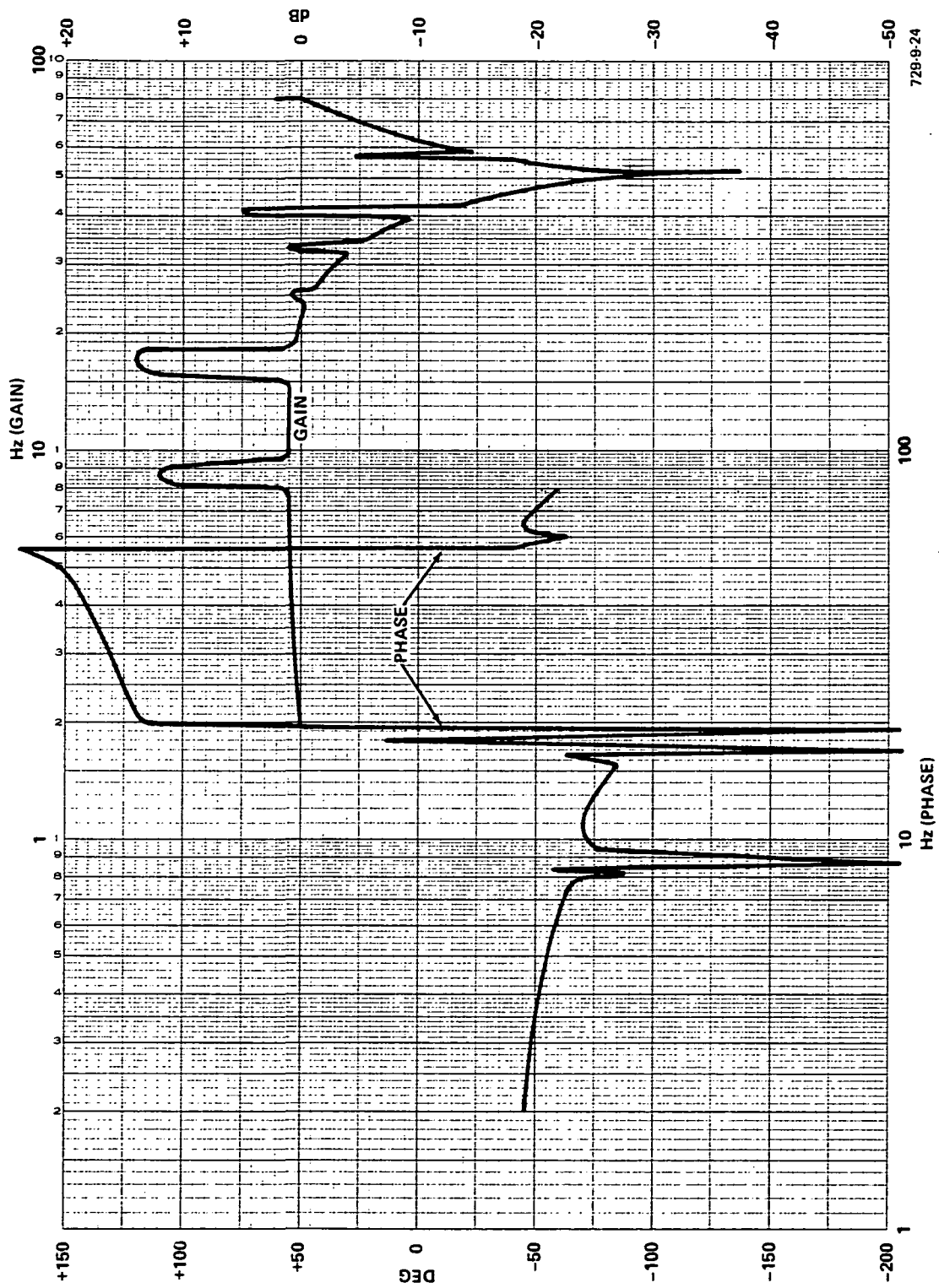


Figure 24
Closed-Loop Frequency Response at
500 R/Min for ΔY Loop

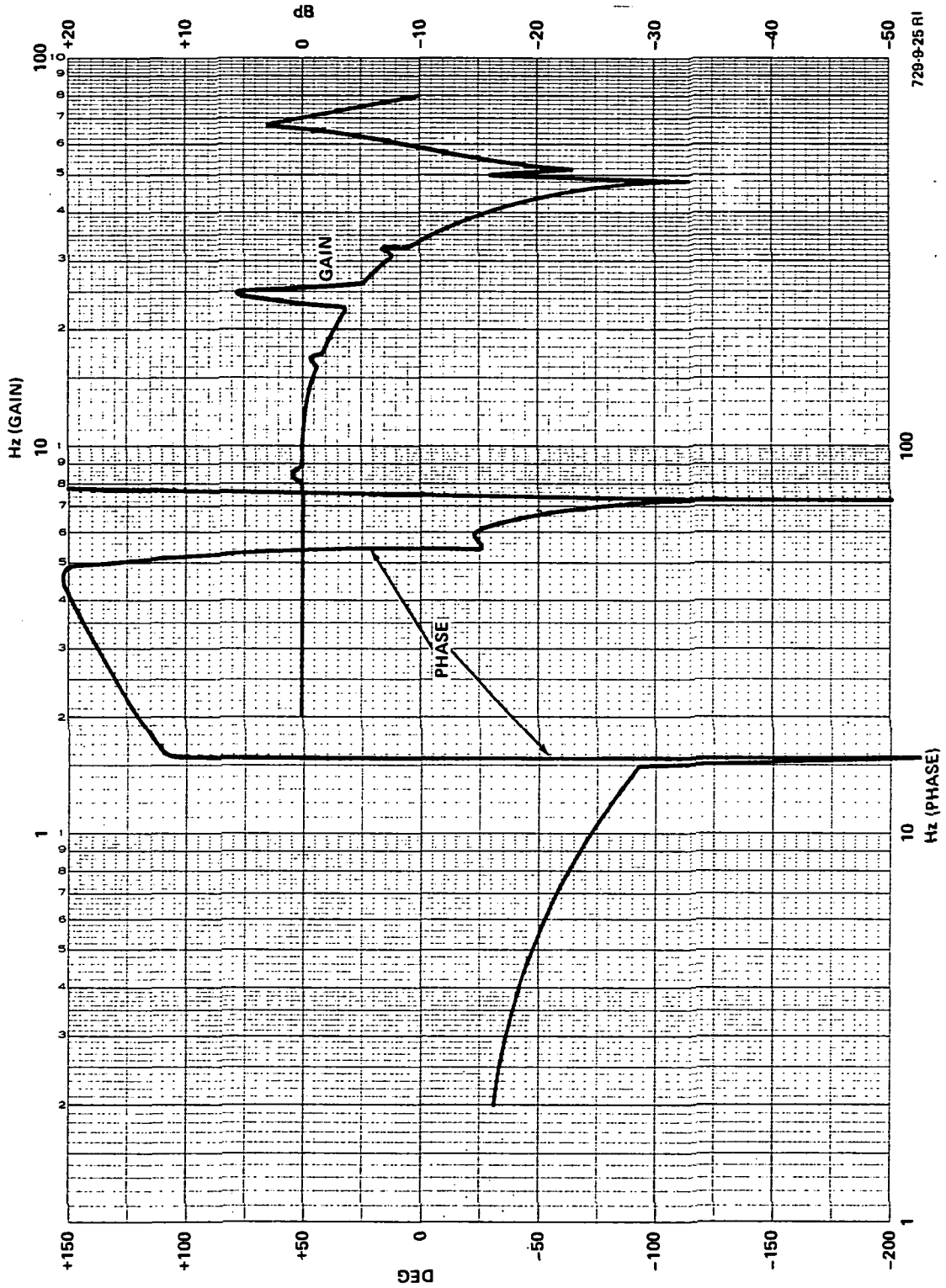
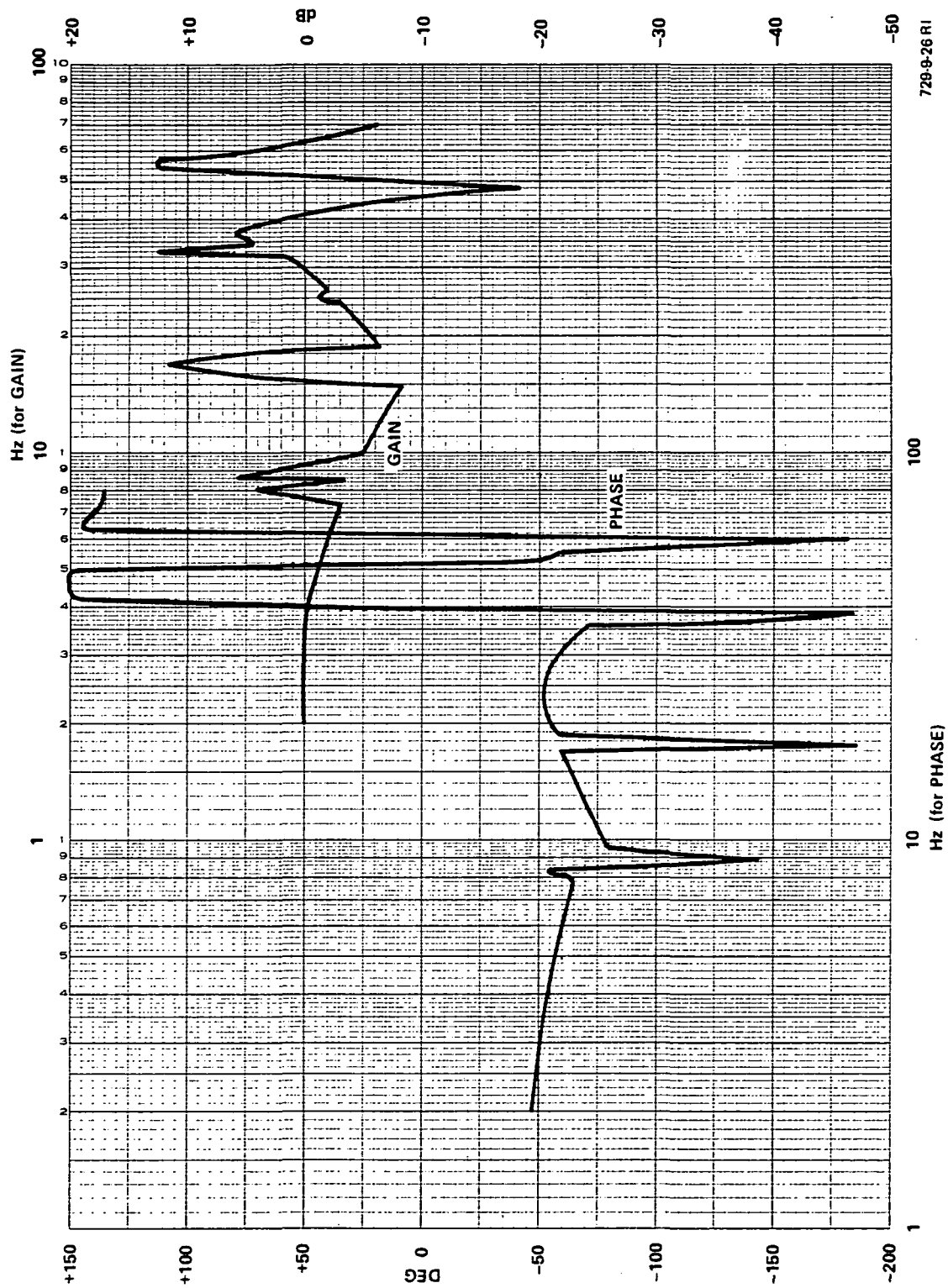


Figure 25
Closed-Loop Frequency Response at
500 R/Min for ΔZ Loop



728-9-26 RI

Figure 26
Closed-Loop Frequency Response at
500 R/Min for 40X Loop

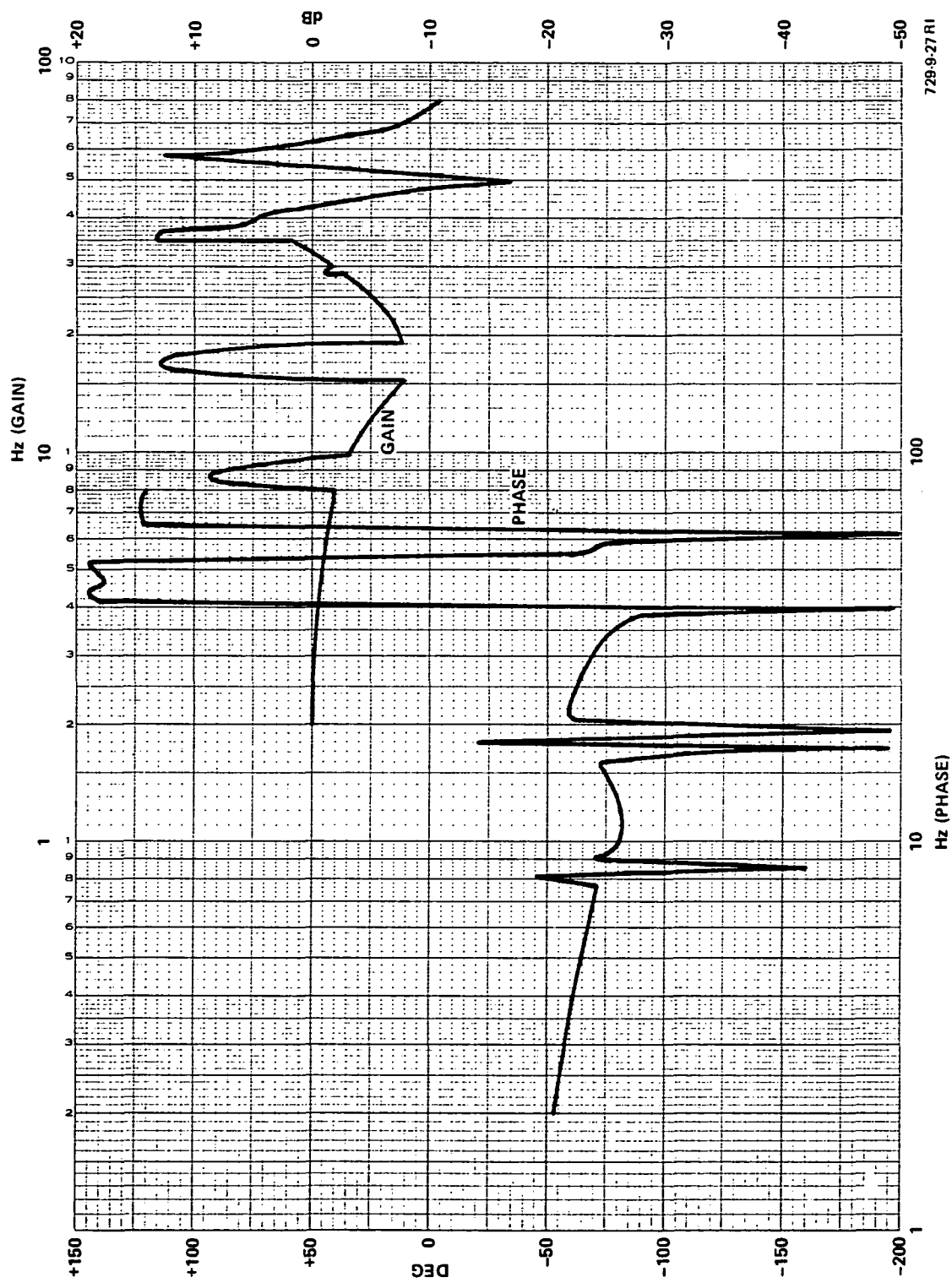


Figure 27
Closed-Loop Frequency Response at
500 R/Min for ΔQY Loop

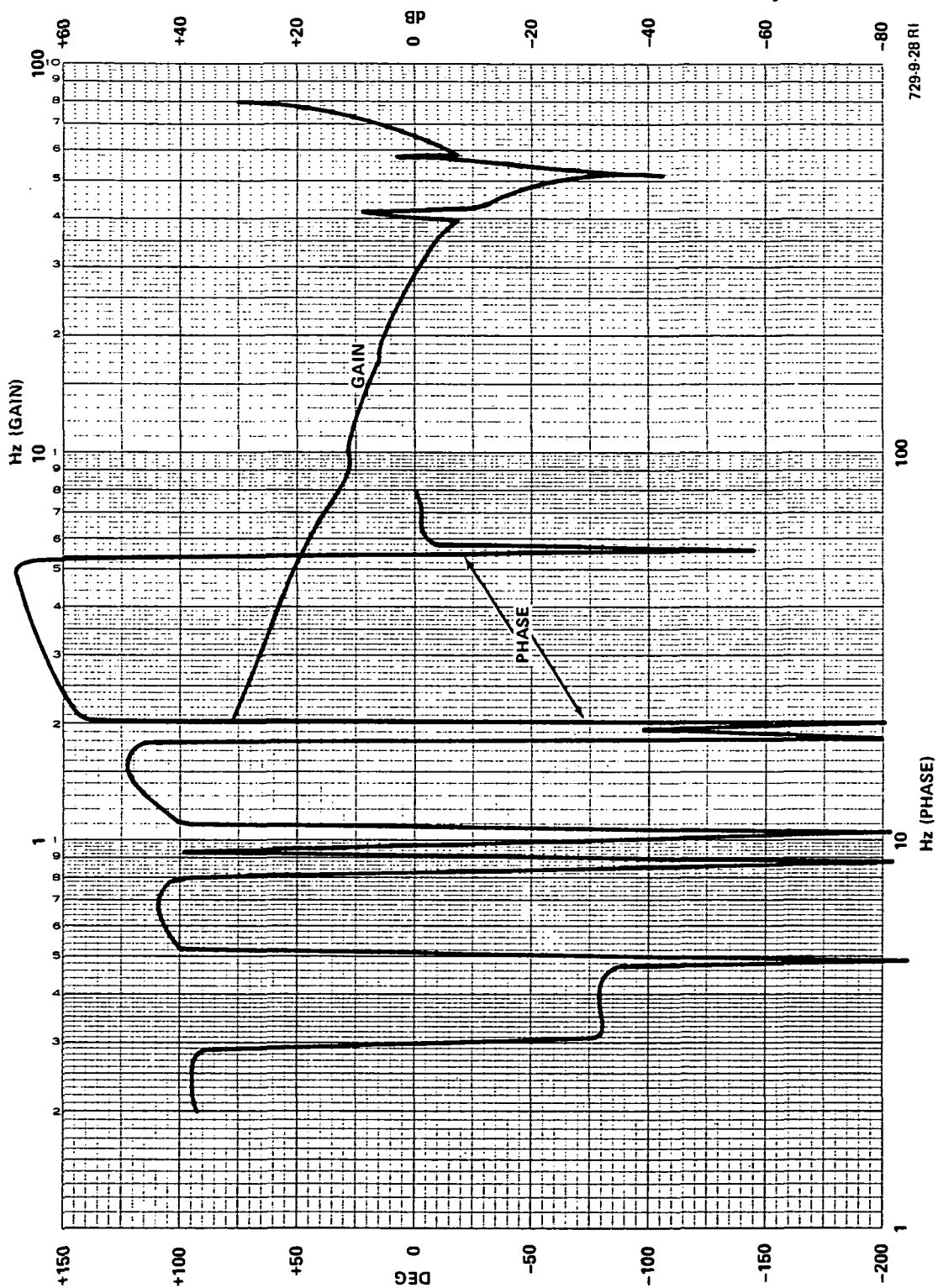


Figure 28
Open-Loop Frequency Response at
500 R/Min for ΔX Loop

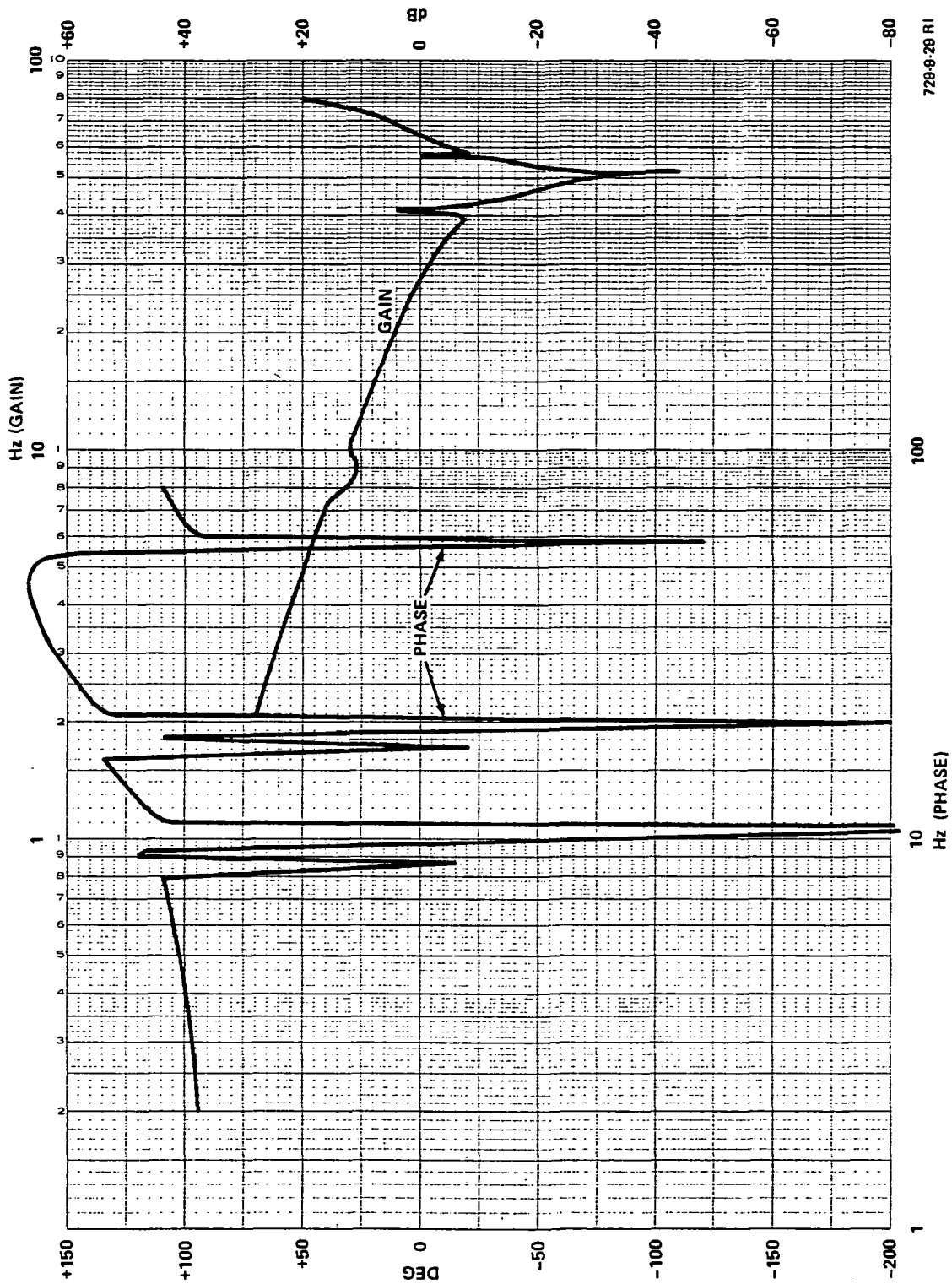


Figure 29
Open-Loop Frequency Response at
500 R/Min for ΔY Loop

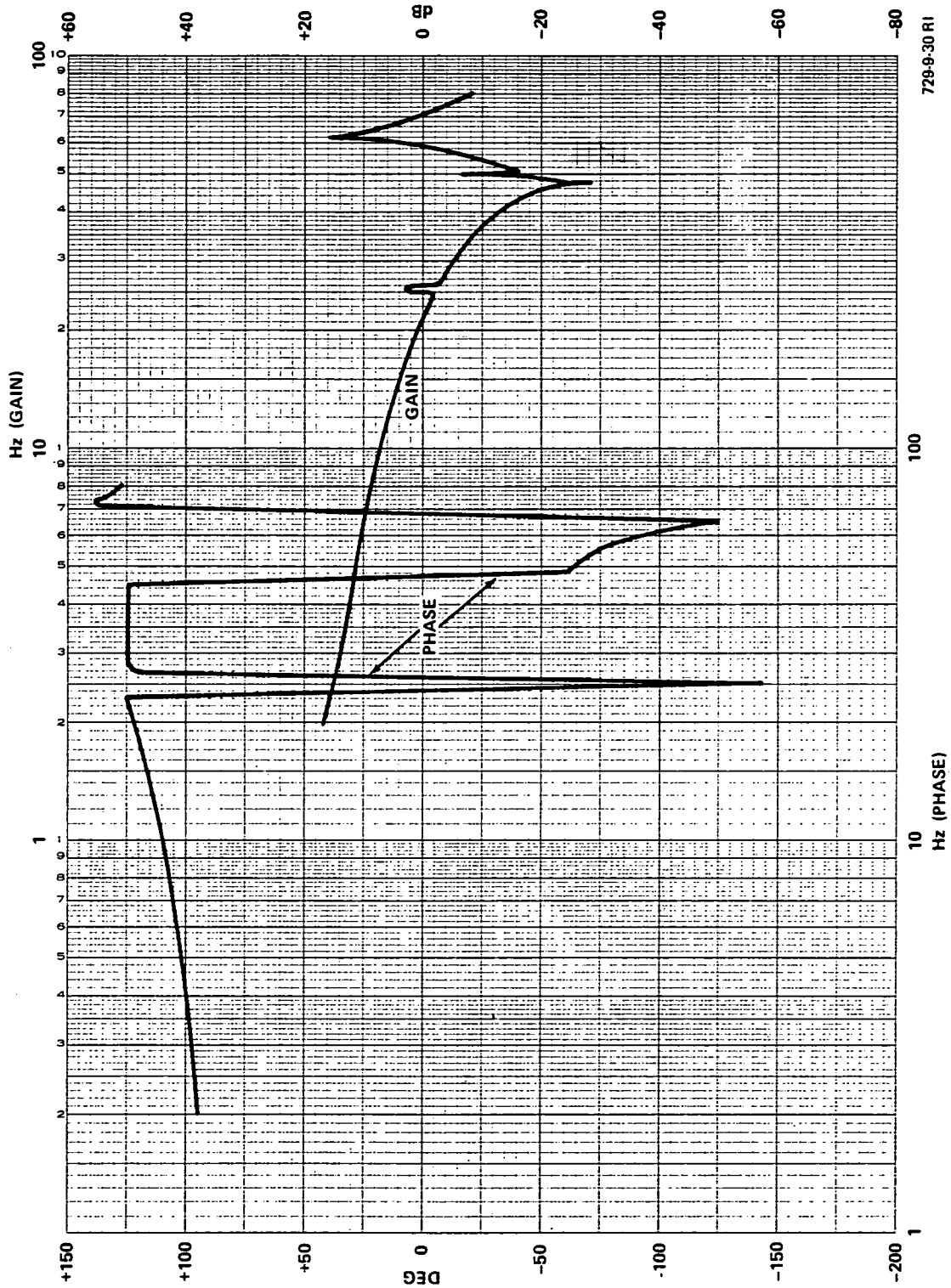


Figure 30
Open-Loop Frequency Response at
500 R/Min for ΔZ Loop

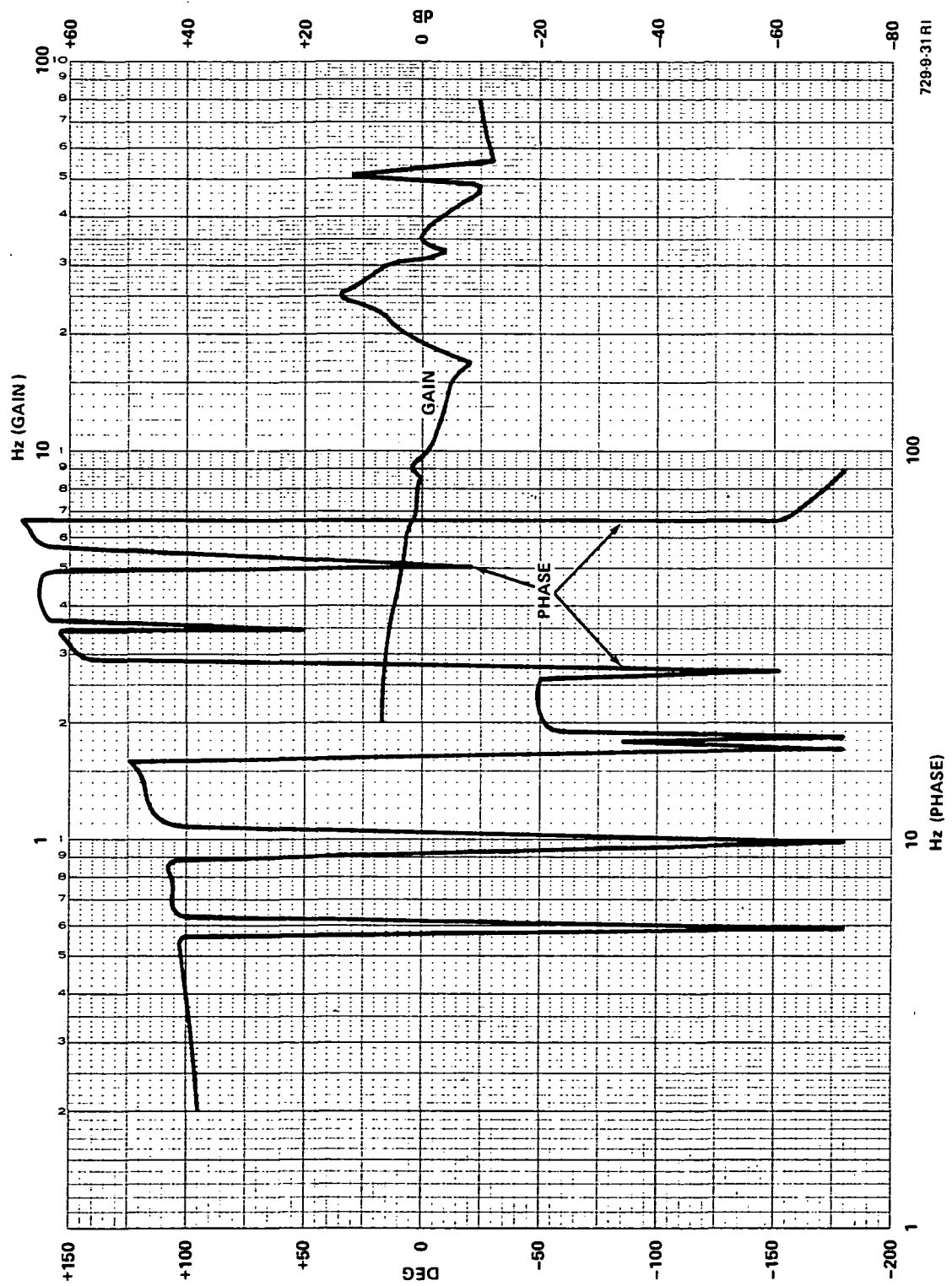


Figure 31
Open-Loop Frequency Response at
500 R/Min for $\Delta 9X$ Loop

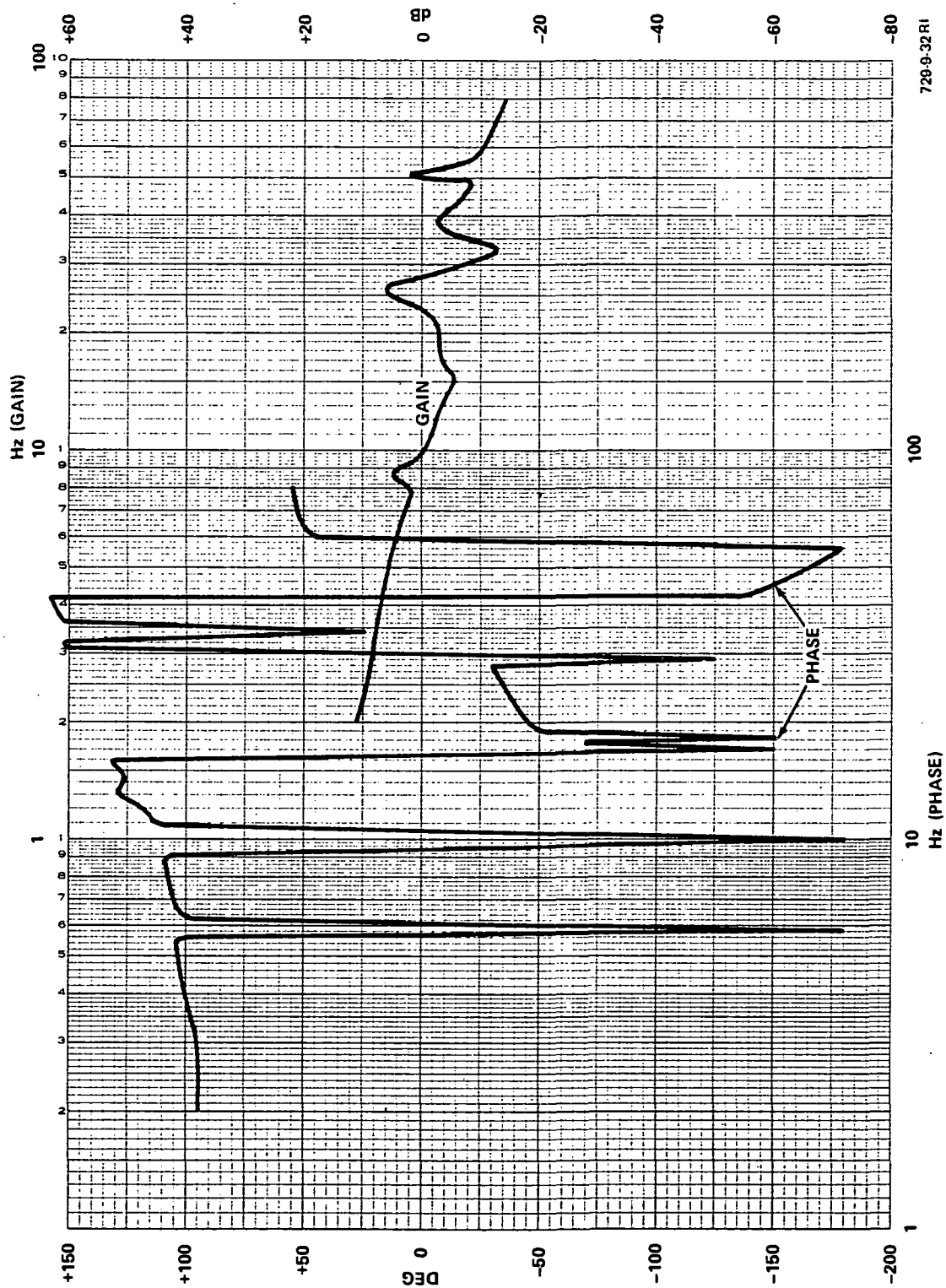


Figure 32
Open-Loop Frequency Response at
500 R/Min for $\Delta 9Y$ Loop

Once the rim balance had been completed a record speed of 725 r/min was achieved. The system became unstable at that speed and was forced to a stop by the backup air bearing and braking system. Further attempts to increase the speed on the basis of dynamic balancing and electronic compensation was beyond the scope of the time and funding framework. The next step was to switch the servo controls to "precession mode" to attempt to achieve higher speeds. Because of the unknown behavior of switching from "direct mode" to "precession mode", it was decided to simulate this mechanism on the analog computer for performance predictions. It was decided to simulate the rim, the magnetic actuators, the driving motor and the associated position/speed sensors. The approach, simulation equations and summary are found in Section 5.

4.4 INTERPRETATION

Zero speed testing disclosed that the rim approximates those dynamic characteristics found in a rigid body. However, the 500-r/min data indicates a number of resonance frequencies. Cross-coupling effects between loops is also evident. These resonances and harmonics are believed to be due to the combined interactive effects of natural rim-bending modes, axial rim warp and gyroscopic characteristics of the system. The most probable cause is the contribution of rim warp which in turn causes the rim-bending effects observed. Rim warp is discussed in Section 5.1. No cross-coupling effect between the loops was anticipated. However this effect should be taken into account for future work. Also, the data for 500-r/min characterization indicates that AMCD along with its support structure cannot be used as a rigid body system. The stiffness of the rim and the support structure play an important part in determining system stability and must be incorporated in the design. There is a limit to the perfection of the rim shape which contributes to rim warp and leads to a number of warp induced signals on top of the "ideal" signal. These rim irregularities and the associated mass imbalances must be compensated, either mechanically or through electronic compensation.

Subsequent testing and analyses have disclosed that minor variations in actuator position and magnetic force constants, K and b , between each actuator are also contributing factors to the suspension system instability. Analysis has shown that the concept of using a single position sensor while trying to control multiple actuators is not completely accurate. Using the test model

AMCD, each position sensor could, at best, sense only the average rim position at each station. As long as the rim is perfectly centered within the station, this data is accurate. However, should any "tilt" exist within the station, then unequal forces will be acting on the rim. This is due to the parallel connection of four actuators per station. Since the actual force is really a square law effect, significant force imbalance can exist within each actuator station.

The conclusion reached from these observations is that for each actuator within the system, a position sensor should be provided. Ideally, a system of nested control loops (one for each actuator, and one for the combinational loop) is required to compute and control actual rim position. This technique should allow much lower operating loop bandwidths and, as such, should eliminate bending mode excitation. Should bending modes be eliminated, the system simulation predicts stability up to and beyond 3000-ft-lb-sec momentum storage.

Page Intentionally Left Blank

SECTION 5.0
ANALOG COMPUTER SIMULATION

5.1 DESCRIPTION

The portion of the AMCD system to be simulated included (1) magnetic actuators, (2) a rim, (3) a driving motor, (4) a tachometer and (5) position sensors (proximeters). The balance of the system, including the electronic compensation, was connected to the analog computer to complete the loop. Figure 33 illustrates the basic setup.

Force commands from the electronic circuits were fed into the computer. These signals are first converted to the current command signals for their respective actuators by the following formula.

$$I_c = \sqrt{\frac{F_c}{K}} \cdot g_o \left(1 + \frac{b\Delta g}{g_o} \right) \quad (4)$$

where

F_c = Force command

g_o = Reference gap between the rim and the actuator

Δg = Displacement of the gap from its reference position

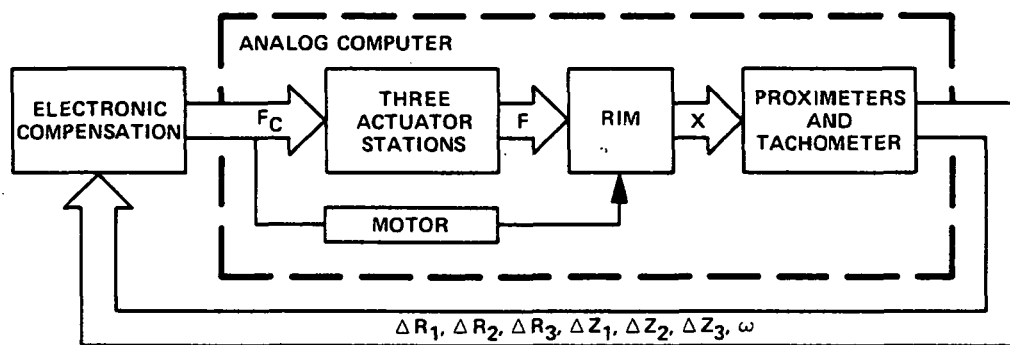
K = Magnetic actuator constant (.00935 lb-in²/A²)

b = Magnetic actuator constant (.9456)

I_c = Current command

The commanded current, when applied to the actuator, attracts the rim with a force F given by

$$F = \frac{K I_c^2}{g_o^2 \left(1 + \frac{b\Delta g}{g_o} \right)^2} \quad (5)$$



729-9-33

Figure 33
AMCD Analog Simulation Setup

The radial and the axial actuator forces acting on the rim give rise to a net displacement of the rim. The displacement is sensed by three radial and three axial proximeters. Equation (5) and the proximeters are modeled on the computer. The output of the simulated displacement sensors is sent to the electronic circuits, where these signals are analyzed and the corrective force commands are computed.

The actual rim is not a perfect rim. By experiment, it was found that the surface of the rim has irregularities.³ Even the radius of the rim is not uniform. These deformations and irregularities, better known as rim warp, cause "ripples" in the rim displacement signals. Also, because of this imperfection, the mass of the rim is not distributed uniformly. The motor and the speed sensor have been incorporated in the simulation. The mass imbalance, the rim ripples and the drive mechanism are discussed in detail in Appendix A. A list of pot settings and static check parameters have been included in the appendix.

5.2 RESULTS

In order to predict the effect of switching electronic control from "direct" mode to the "precession" mode, efforts were made to duplicate the actual test data on the computer. The switch-over mechanism could then be studied without risk of damage to the system.

The step response of the system for zero speed was successfully duplicated. However, 500-r/min characterization could not be fully reproduced. It is believed that since only a rigid body model of the system was simulated, it could not behave like the actual rim. Lack of any compliance of the rim, the support structure, and the bending modes of the rim in the simulation yielded results different from the data.

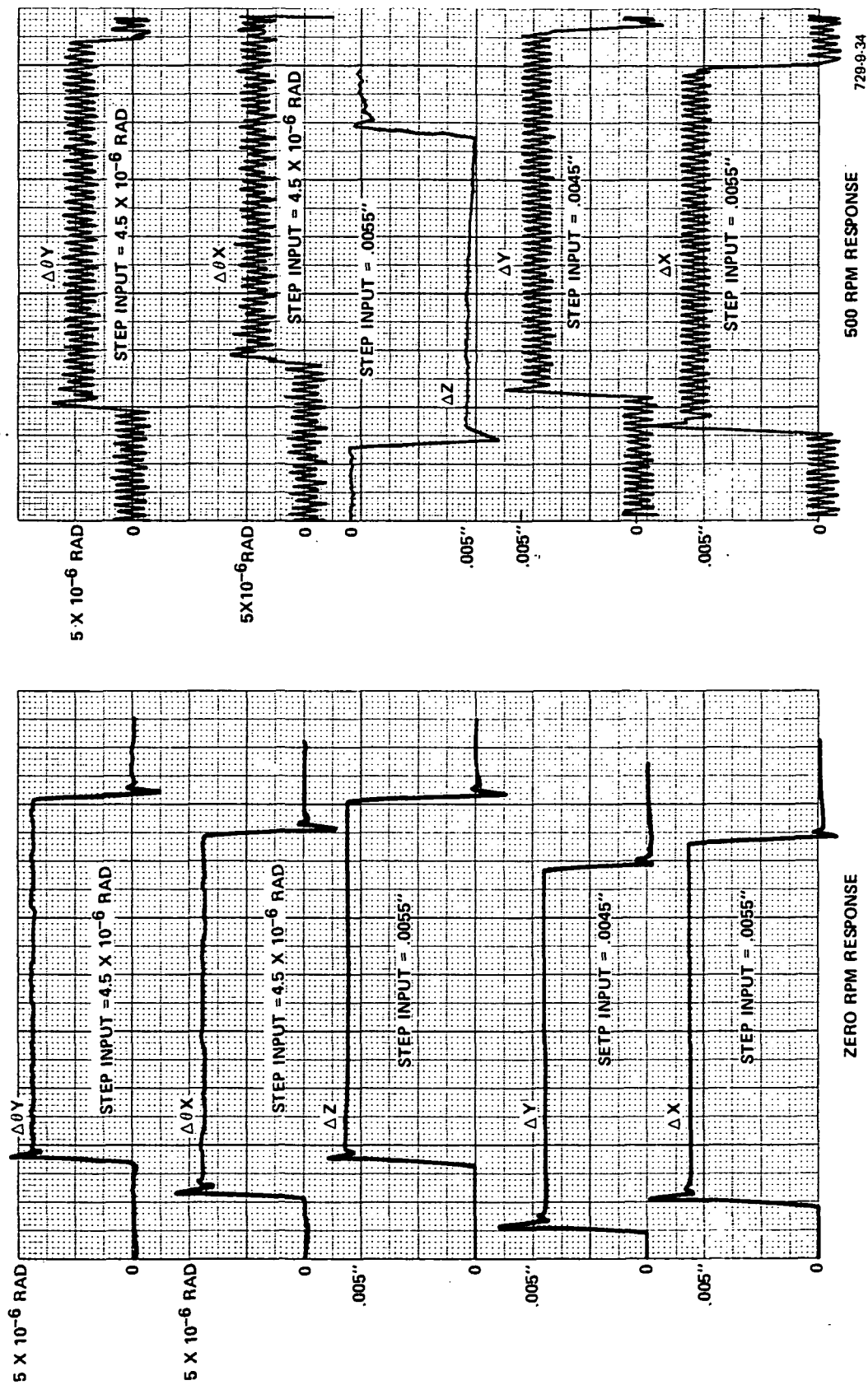


Figure 34
Step Response of Design Simulation

SECTION 6.0

REFERENCES

1. Anderson, Willard W.; and Groom, Nelson J.: The Annular Momentum Control Device (AMCD) and Potential Applications. NASA TN D-7866, 1975.
2. Ball Brothers Research Corp: Annular Momentum Control Device (AMCD), Volumes I and II. NASA CR-144917, 1976.
3. Groom, Nelson J.; and Terray, David E.: Evaluation of a Laboratory Test Model Annular Momentum Control Device. NASA TP-1142, 1978.
4. Groom, Nelson J.; and Waldeck, Gary C.: Magnetic Suspension System for a Laboratory Model Annular Momentum Control Device. AIAA Paper No. 79-1755, AIAA Guidance and Control Conference, Boulder, Colorado, August 6-8, 1979.
5. Wilson, George W.: Double Gimbal Control Moment Gyroscope Gimbal Control Loop Synthesis. AIAA Paper No. 75-1108, AIAA Guidance and Control Conference, Boston, Massachusetts, August 20-22, 1975.

Page Intentionally Left Blank

APPENDIX A

ANALOG SIMULATION MODEL

A.1 SIMULATION SCHEMATIC AND SCALING

The complete AMCD system illustrated in Figures 4 and 5 can be approximated by Figure 36 below.

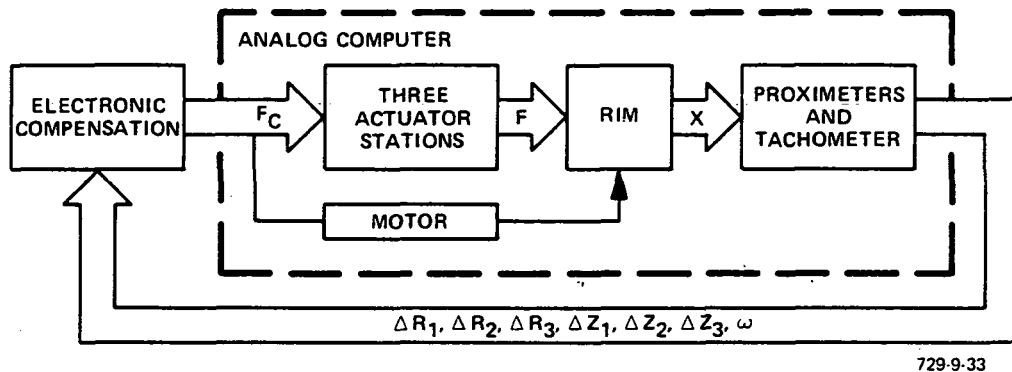


Figure 35
AMCD System Configuration for Analog Simulation

Because of the size and complexity of the simulation, two complete Applied Dynamics Analog-Hybrid AD/4* computers were used in the "master-slave" mode. Blocks shown within the dotted lines represent the simulated parts of the AMCD

*It is a general-purpose hybrid analog computer with reference voltage of ± 100 volts. It has a 4-quadrant analog patchboard, a logic patchboard, a single panel control console with pushbutton keyboard and digital displays, and an attached 8-channel strip chart recorder. Each quadrant of the patchboard is a modular grouping of the analog components, which includes two bipolar summer integrators, eight coefficient devices, bipolar summer-track-hold amplifiers, multipliers, fixed or variable DFGs, hard limiters, and passive networks.

system. They include actuators, a rim, a drive motor, a tachometer and proximeters. The rest of the system, including electronic compensation, was connected to the computer to complete the loop.

The simulation was divided into two basic parts - radial loop simulation and axial loop simulation. The signal flow and scaling scheme are given in subsequent sections.

A.1.1 Radial Loop Simulation

This loop is further divided into four parts.

A.1.1.1 Force Command to Current Command

Three force commands, F_{1RC} , F_{2RC} and F_{3RC} , are received from the electronics servo compensation networks. These commands are converted to current commands determined by the Equation (A-1).

$$F = \frac{K I^2}{R_0^2 \left(1 + \frac{b\Delta R}{R_0}\right)^2} \quad (A-1)$$

Since each station has four magnetic actuators and each actuator current command is determined by Equation (A-1), the total force F_c and the total current I_c are related by

$$F_c = \frac{4K (I_c/4)^2}{R_0^2 \left(1 + \frac{b\Delta R}{R_0}\right)^2} \quad (A-2)$$

where

K = Actuator constant (.00935 lb-in²/A²)

b = Actuator constant (.9456)

R_0 = Reference gap between the rim and the actuator (.2 in.)

ΔR = Difference between actual gap R and the reference gap $[(R-R_0)$ inches]

Equation (A-2) can be rewritten as

$$I_c = \sqrt{10} F_c \left(\frac{4R_o}{\sqrt{40K}} \right) [1 + (4.728R - .9456)] \quad (A-3)$$

Magnitude scaling (A-3) for

$$I_{\max} = 20 \text{ A}, R_{\max} = .2 \text{ in.}, F_{\max} = 50 \text{ lb}$$

we get

$$20 \left(\frac{I_c}{20} \right) = 4.1367 \left[.0544 + 4.728(.2) \left(\frac{R}{.2} \right) \right] \left(\sqrt{\frac{F_c}{50}} \right) (\sqrt{50})$$

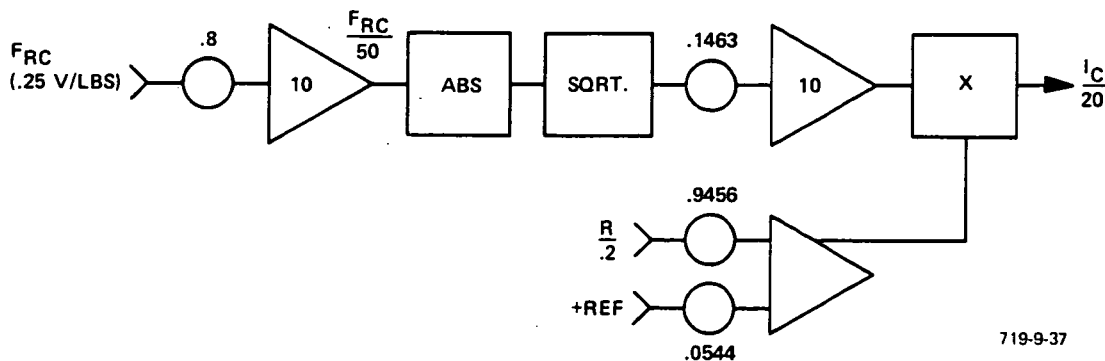
or

$$\left(\frac{I_c}{20} \right) = 1.4625 \left[.0544 + .9456 \left(\frac{R}{.2} \right) \right] \left(\sqrt{\frac{F_c}{50}} \right) \quad (A-4)$$

Also, F_c from the electronics has units of 25 volt/lb and F_c in the computer has units of 2 volt/lb. Therefore, we need an input gain of $2/.25 = 8$.

In Equation (A-4), F_c represents either of the three radial force commands, F_{1RC} , F_{2RC} or F_{3RC} . Similarly, I_c represents any of the three corresponding current commands, I_{1RC} , I_{2RC} or I_{3RC} .

Equation (A-4) can be represented by the following analog block diagram.



The actual analog computer patching diagrams, for the above diagram, as well as for all of the following diagrams in this appendix, are shown in Figures 37 and 38.

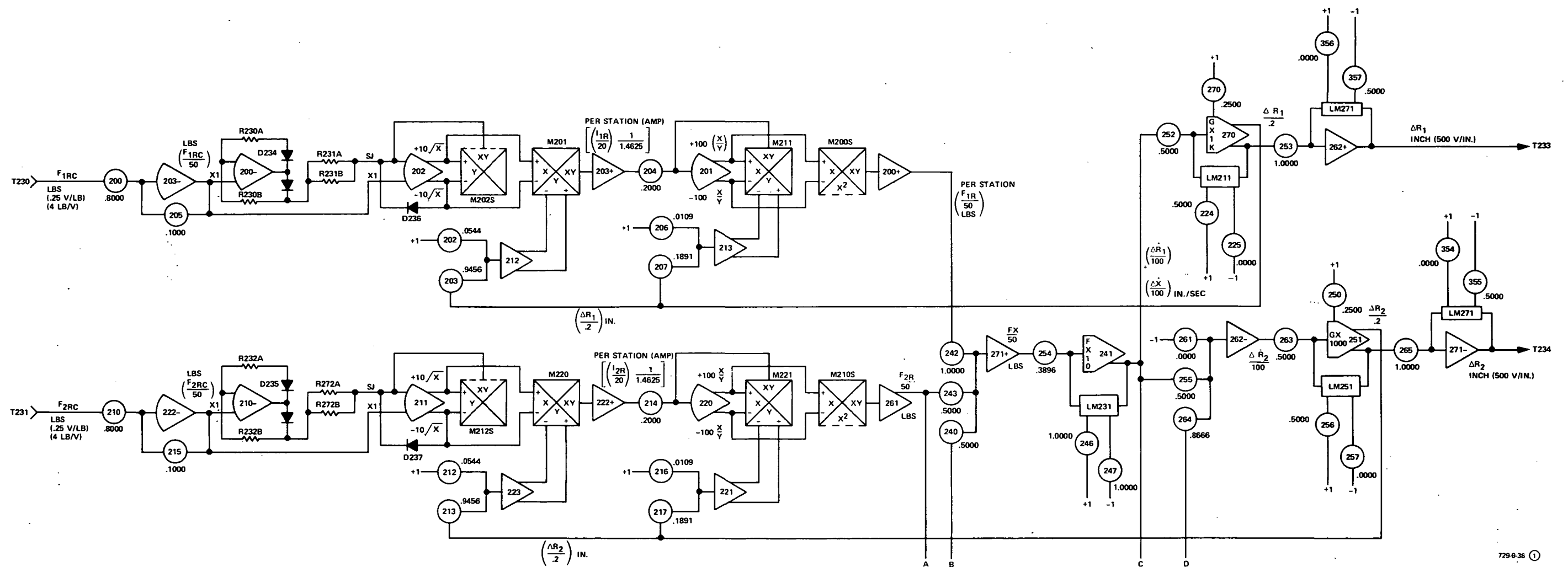


Figure 36
AMCD Radial Loops
(Sheet 1 of 2)

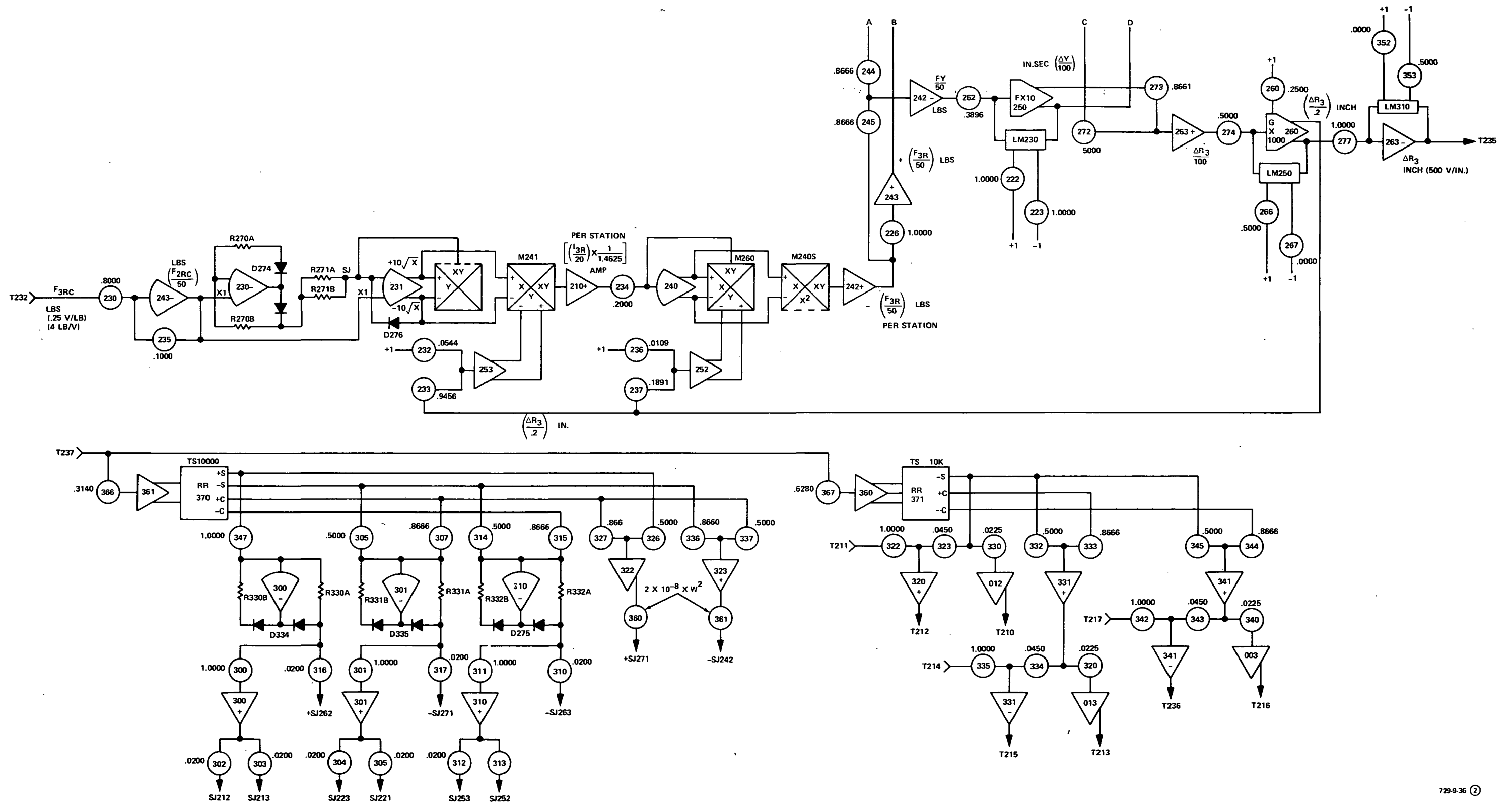


Figure 36
AMCD Radial Loops
(Sheet 2 of 2)

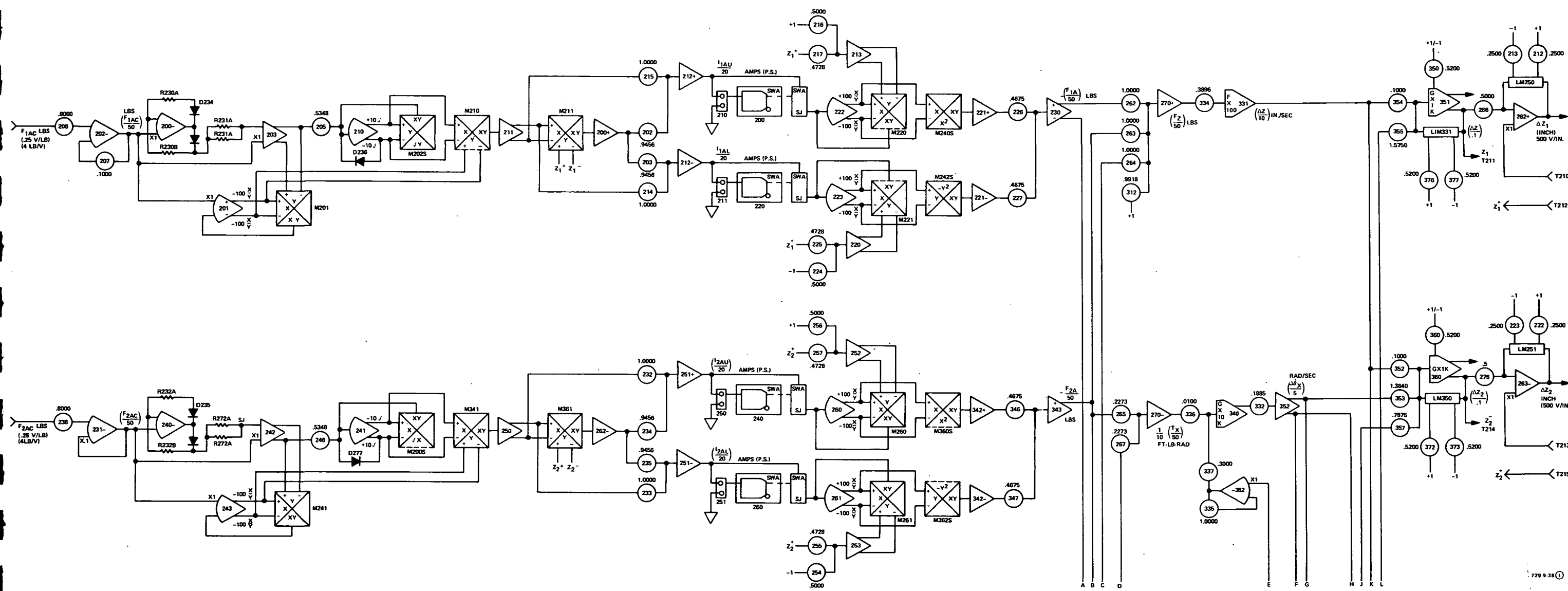


Figure 37
AMCD Axial Loops
(Sheet 1 of 2)

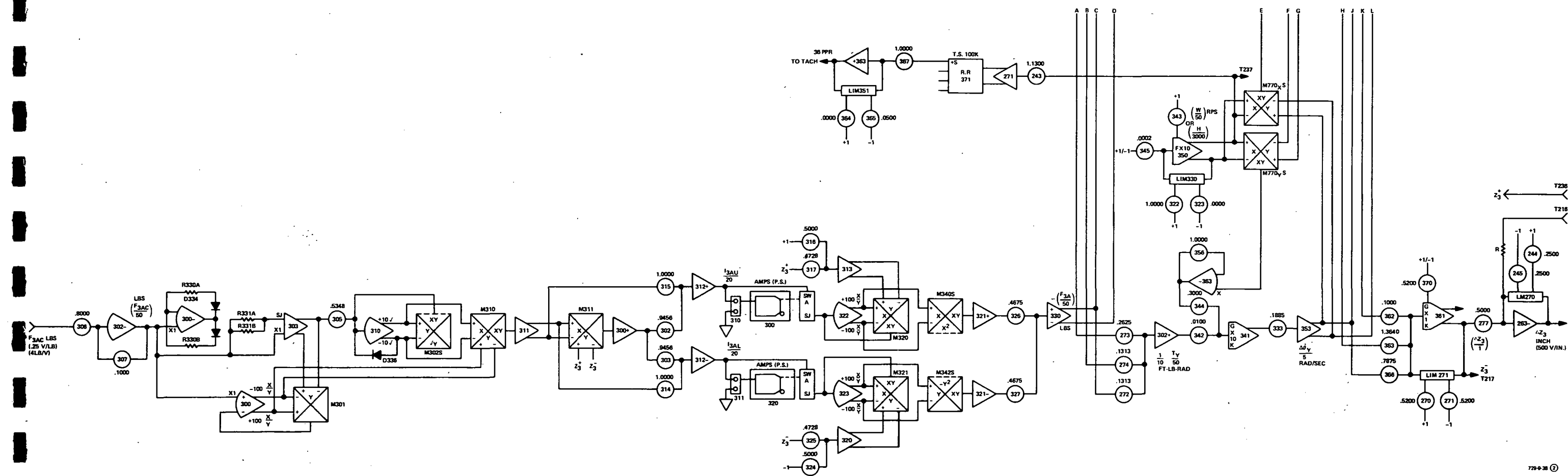


Figure 37
AMCD Axial Loops
(Sheet 2 of 2)

A.1.1.2 Current Command to Force Applied

When the commanded current is applied to a magnetic actuator, it attracts the rim with a force given by the Equation (A-1). For four radial actuators at each station, the total force is given by

$$F_R = \frac{4K (I_C/4)^2}{R_0^2 \left(1 + \frac{b\Delta R}{R_0}\right)^2} \quad (A-5)$$

Scaling (A-5) for

$$F_{R_{\max}} = 50 \text{ lb and } I_{C_{\max}} = 20 \text{ A}$$

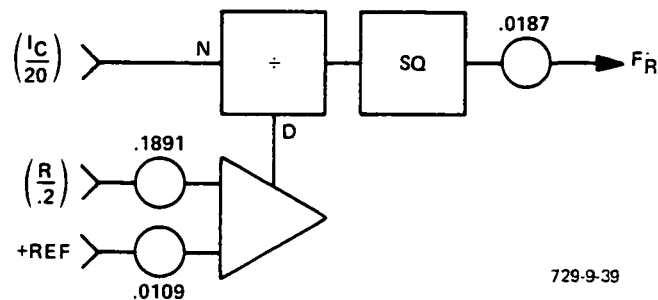
we get,

$$50 \left(\frac{F_R}{50}\right) = \frac{4(.00935)(20)^2(I_C/20)^2}{[R_0 + b(R - R_0)]^2} \quad (A-6)$$

or

$$\left(\frac{F_R}{50}\right) = .0187 \left[\frac{(I_C/20)^2}{.01088 + .18912 \left(\frac{R}{.2}\right)^2} \right] \quad (A-7)$$

Equation (A-7) is represented by the following analog block diagram.



729-9-39

A.1.1.3 Force to Gap Rate

The forces F_{1R} , F_{2R} and F_{3R} from each of the three radial actuators produce resultant radial forces F_X along the X axis and F_Y along the Y axis. These forces produce acceleration in the rim. The rate of movement of the rim can be computed by Equation (A-8).

$$\Delta \dot{X} = \int \left(\frac{F_X}{M} \right) dt \quad (A-8)$$

where $\Delta \dot{X}$ is the rate of travel of the rim along the X axis and M is the mass of the rim. Scaling (A-8) for $F_{X_{max}} = 50$ lb and $\Delta \dot{X}_{max} = 100$ in./sec, we get

$$100 \left(\frac{\Delta \dot{X}}{100} \right) = \frac{12}{1.54} \int 50 \left(\frac{F_X}{50} \right) dt \quad (A-9)$$

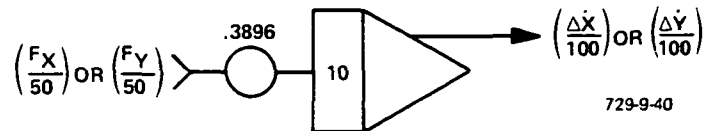
or

$$\left(\frac{\Delta \dot{X}}{100} \right) = 3.896 \int \left(\frac{F_X}{50} \right) dt \text{ in./s}$$

Similarly, for the rate of motion along the Y axis,

$$\left(\frac{\Delta \dot{Y}}{100} \right) = 3.896 \int \left(\frac{F_Y}{50} \right) dt \text{ in./s} \quad (A-10)$$

Equations (A-9) and (A-10) are represented by the following figure.



A.1.1.4 Radial Gap

$\dot{\Delta X}$ and $\dot{\Delta Y}$ are matrixed to compute three radial gap rates $\dot{\Delta R}_1$, $\dot{\Delta R}_2$ and $\dot{\Delta R}_3$. Then individual gaps ΔR_1 , ΔR_2 and ΔR_3 are given by

$$\Delta R = \int \dot{\Delta R} dt \quad (A-11)$$

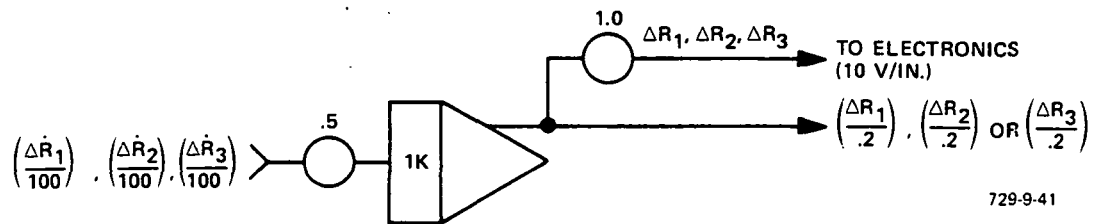
Scaling (A-11) for $\dot{\Delta R}_{\max} = 100$ in./s and $\Delta R_{\max} = .2$ in., we get

$$.2 \left(\frac{\Delta R}{.2} \right) = \int 100 \left(\frac{\dot{\Delta R}}{100} \right) dt \quad (A-12)$$

or

$$\left(\frac{\Delta R}{.2} \right) = 500 \int \left(\frac{\dot{\Delta R}}{100} \right) dt$$

Equation (A-12) is represented by the following analog diagram.



729-9-41

These gaps are transmitted to the electronics compensation circuits. Since ΔR_1 is 500 V/in. and input to the electronics is 500 V/in., we need a gain of $500/500 = 1.0$ as shown in the figure above.

A.1.2 Axial Loop Simulation

This loop is modeled in the same way as the radial loop. However, each station has two axial magnetic actuators. These are (1) upper axial actuators which attract the rim upward against gravity, and (2) lower axial actuators which pull the rim downward, aided by gravity. Positional signals from the axial proximeters and the electronic circuits decide which actuator to energize to keep the rim in the center of the gap.

The axial loop is divided into six parts.

A.1.2.1 Force Command to Current Command

Three force commands, F_{1AC} , F_{2AC} and F_{3AC} , are received from the electronics servo compensation networks. These commands are converted to the respective station current commands according to the formula of Equation (A-13).

$$F = \frac{K I^2}{Z_0^2 \left(1 + \frac{b\Delta Z}{Z_0}\right)^2} \quad (A-13)$$

Since each station has four magnetic actuators, the total force F_C and the total current I_C are related by

$$F_C = \frac{4K (I_C/4)^2}{Z_0^2 \left(1 + \frac{b\Delta Z}{Z_0}\right)^2} \quad (A-14)$$

where

K, b = Actuator constants

Z_0 = Reference axial gap (.1 in.)

ΔZ = Difference between the actual gap Z and the reference gap
 Z_0 [($Z-Z_0$) in.]

Equation (A-14) can be written as

$$I_C = \sqrt{10F_C} \left(\frac{4Z_0}{\sqrt{40K}} \right) \left(1 + \frac{b\Delta Z}{Z_0} \right) \quad (A-15)$$

Magnitude scaling (A-15) for

$$I_{C_{\max}} = 20 \text{ A}, \Delta Z_{\max} = .1 \text{ in. and}$$

$$F_{C_{\max}} = 50 \text{ lb},$$

we get,

$$20 \left(\frac{I_C}{20} \right) = 2.0684 \left[1 + 9.456 (.1) \left(\frac{\Delta Z}{.1} \right) \right] (\sqrt{50}) \left(\sqrt{\frac{F_C}{50}} \right) \quad (\text{A-16})$$

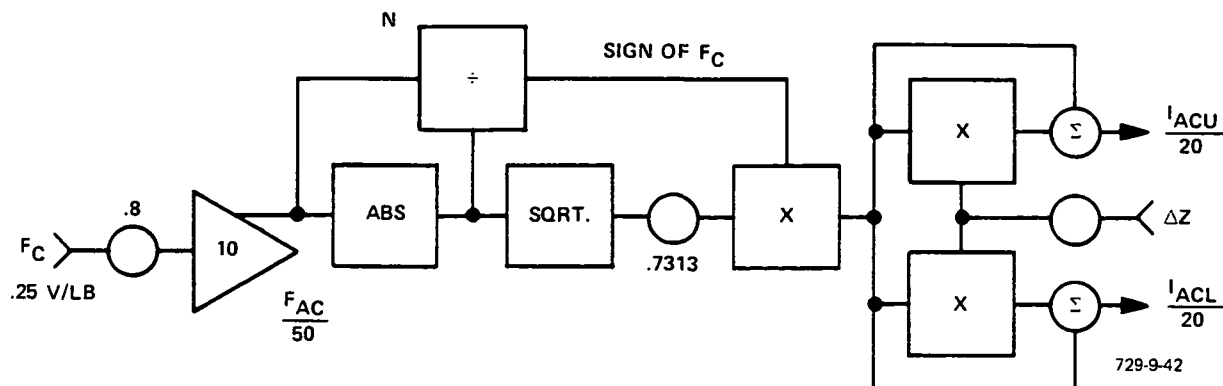
or

$$\left(\frac{I_C}{20} \right) = .7313 \left[1 + .9456 \left(\frac{\Delta Z}{.1} \right) \right] \left(\sqrt{\frac{F_C}{50}} \right) \quad (\text{A-17})$$

Since each station has upper and lower actuators, they are commanded according to the polarity of the ΔZ gap. When the rim moves above the center of the gap, ΔZ is negative. When the rim is positioned below the center of the gap, ΔZ is positive. Force F_C is positive or negative accordingly. The upper actuator current command is determined by Equation (A-17), and the lower actuator current command is determined by Equation (A-18).

$$\left(\frac{I_C}{20} \right)_{\text{lower}} = .7313 \left[-1 + .9456 \left(\frac{\Delta Z}{.1} \right) \right] \left(\sqrt{\frac{F_C}{50}} \right) (\text{Sign of } F_C) \quad (\text{A-18})$$

Equation (A-17) represents the upper axial actuator current commands I_{1ACU} , I_{2ACU} and I_{3ACU} for axial stations 1, 2 and 3, respectively. Similarly, Equation (A-18) represents the lower axial actuator current commands I_{1ACL} , I_{2ACL} and I_{3ACL} . The representative analog schematic is given below.



A.1.2.2 Current Command to Force Applied

As in the radial loop, the command current I_C applied to the axial actuator produces force F_A on the rim.

$$F_A = \frac{4K (I_C/4)^2}{(Z_0 + b\Delta Z)^2} \quad (A-19)$$

Force applied by the upper axial actuator is given by

$$F_{Au} = \frac{4K (I_{cu}/4)^2}{(Z_0 + b\Delta Z)^2} \quad (A-20)$$

Magnitude scaling (A-20) for

$$F_{AU_{max}} = 50 \text{ lb}, I_{CU_{max}} = 20 \text{ A}, \Delta Z_{max} = .1 \text{ in.}$$

we get

$$50 \left(\frac{F_{Au}}{50} \right) = \frac{(.00935/4) (20^2) (I_{cu}/20)^2}{[.1 + (.9456) (.1) \left(\frac{\Delta Z}{.1} \right)]^2} \quad (A-21)$$

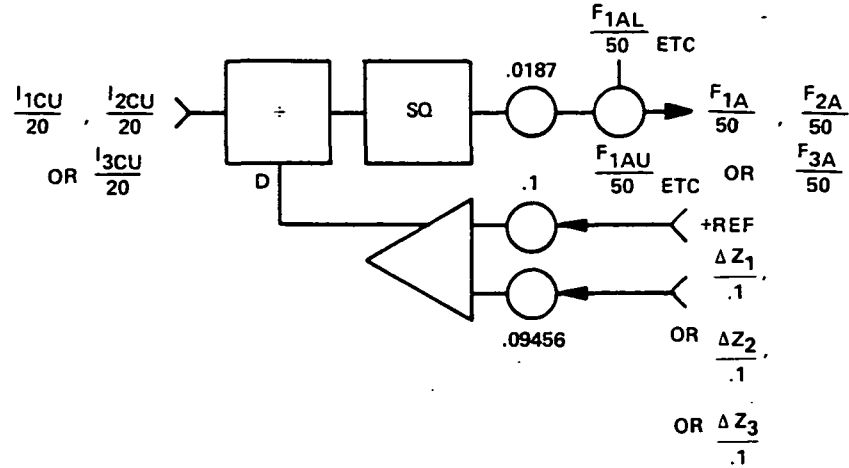
or

$$\left(\frac{F_{Au}}{50} \right) = .0187 \left[\frac{(I_{cu}/20)}{.1 + .09456 \left(\frac{\Delta Z}{.1} \right)} \right]^2 \quad (A-22)$$

Similarly, for the lower actuators

$$\left(\frac{F_{Al}}{50} \right) = .0187 \left[\frac{(I_{cl}/20)}{-.1 + .09456 \left(\frac{\Delta Z}{.1} \right)} \right]^2 \quad (A-23)$$

Equation (A-22) can be represented by the following analog block diagram.



729-9-43

F_{1A} is the net axial force at Station 1.

A.1.2.3 Force to Gap Rate

Three axial forces F_{1A} , F_{2A} and F_{3A} are matrixed to compute net axial force F_Z , torque T_X about the X axis passing through Station 1, and Torque T_Y about the Y axis. Force F_Z gives rise to axial gap rate $\Delta \dot{Z}$ by the formula

$$\Delta \dot{Z} = \int \left(\frac{F_Z}{M} \right) dt \quad (A-24)$$

Scaling (A-24) for $\Delta \dot{Z}_{\max} = 10$ in./s, $F_{Z\max} = 50$ lb,

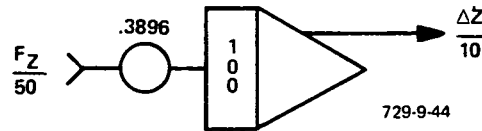
we get

$$10 \left(\frac{\Delta \dot{Z}}{10} \right) = \frac{12}{1.54} \int \left(\frac{F_Z}{50} \right) 50 \quad (A-25)$$

or

$$\left(\frac{\Delta \dot{Z}}{10} \right) = 38.96 \int \left(\frac{F_Z}{50} \right)$$

Equation (A-25) is represented by the figure below.



A.1.2.4 Torque to Rotation Rate

Torques T_X and T_Y and the gyroscopic cross-coupling (H) between these rotational loops, produces angular rates $\Delta\dot{\theta}_X$ and $\Delta\dot{\theta}_Y$.

$$I_X = I_Y = 5.306 \text{ slug-ft}^2 = 5.306 \text{ ft-lb-s}^2$$

$$I_Z = 10.6 \text{ ft-lb-s}^2 \text{ (approximately)}$$

$$\begin{aligned} H = I_Z(\omega) &= 10.6 \times 3000 \text{ r/min} \times \frac{1 \text{ min}}{60 \text{ s}} \times \frac{2\pi \text{ rad}}{\text{rev}} \\ &= 3300 \text{ ft-lb-s for 3000 r/min of the rim} \end{aligned}$$

$$\Delta\dot{\theta}_X = \frac{1}{I_X} \int (T_X + H\Delta\dot{\theta}_Y) \quad (\text{A-26})$$

Magnitude scaling (A-26) for

$$\Delta\dot{\theta}_{X_{\max}} = \Delta\dot{\theta}_{Y_{\max}} = 5 \text{ rad/sec}, H_{\max} = 3000 \text{ ft-lb-sec},$$

we get

$$5 \left(\frac{\Delta\dot{\theta}_X}{5} \right) = \frac{1}{5.306} \int \left[50 \left(\frac{T_X}{50} \right) + 3000 \left(\frac{H}{3000} \right) (5) \left(\frac{\Delta\dot{\theta}_Y}{5} \right) \right] \quad (\text{A-27})$$

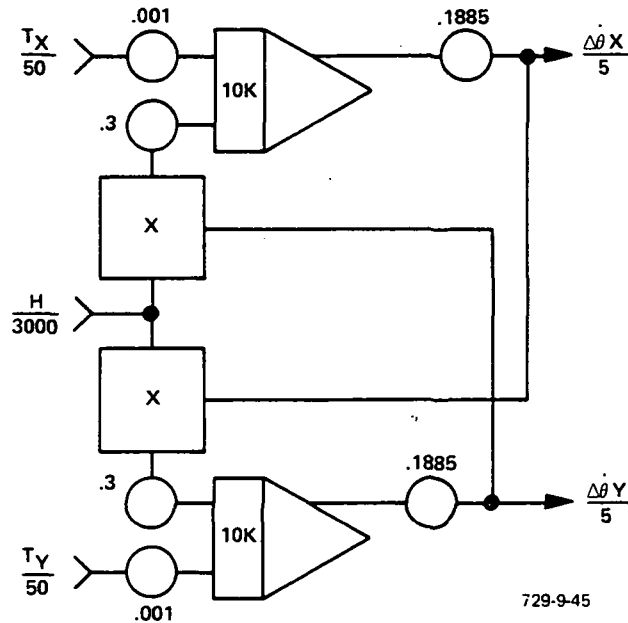
or

$$\left(\frac{\Delta\dot{\theta}_X}{5} \right) = .1885 \int \left[10 \left(\frac{T_X}{50} \right) + 3000 \left(\frac{H}{3000} \right) \left(\frac{\Delta\dot{\theta}_Y}{5} \right) \right]$$

Similarly,

$$\left(\frac{\Delta\dot{\theta}_Y}{5}\right) = .1885 \int \left[10 \left(\frac{T_Y}{50}\right) + 3000 \left(\frac{H}{3000}\right) \left(\frac{\Delta\dot{\theta}_X}{5}\right) \right] \quad (A-28)$$

Equations (A-27) and (A-28) are modeled below.



A.1.2.5 Angular Rates to Axial Displacement Rates

$\Delta\dot{Z}$, $\Delta\dot{\theta}_X$ and $\Delta\dot{\theta}_Y$ are decoupled to compute axial translation rates $\Delta\dot{Z}_1$, $\Delta\dot{Z}_2$ and $\Delta\dot{Z}_3$ for Stations 1, 2 and 3. (See Figure 4.) These rates are given below.

$$\Delta\dot{Z}_1 = \Delta\dot{Z} - 12 R \Delta\dot{\theta}_Y \quad (A-29)$$

Scaling (A-29) for

R = radius of the rim (2.625 ft)

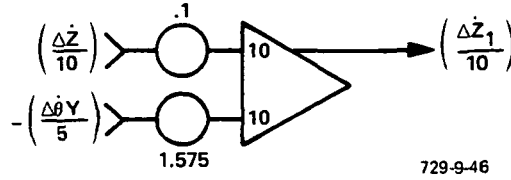
$$\Delta\dot{Z}_{1\max} = \Delta\dot{Z}_{\max} = 10 \text{ in./s}$$

$$\Delta\dot{\theta}_{Y\max} = 5 \text{ rad/s,}$$

we get,

$$\left(\frac{\dot{\Delta Z}_1}{10}\right) = \left(\frac{\dot{\Delta Z}}{10}\right) - 15.75 \left(\frac{\dot{\Delta \theta}_Y}{5}\right) \quad (A-30)$$

(A-30) is modeled below.



Also,

$$\dot{\Delta Z}_2 = \dot{\Delta Z} + 12 (\sqrt{3}/2) R \dot{\Delta \theta}_X + 12(R/2) \dot{\Delta \theta}_Y \quad (A-31)$$

and

$$\dot{\Delta Z}_3 = \dot{\Delta Z} - 12 (\sqrt{3}/2) R \dot{\Delta \theta}_X + 12(R/2) \dot{\Delta \theta}_Y \quad (A-32)$$

Magnitude scaling (A-31) and (A-32) for

$$\dot{\Delta Z}_{2\max} = \dot{\Delta Z}_{3\max} = \dot{\Delta Z}_{\max} = 10 \text{ in./s}$$

$$\dot{\Delta \theta}_{X\max} = \dot{\Delta \theta}_{Y\max} = 5 \text{ rad/s,}$$

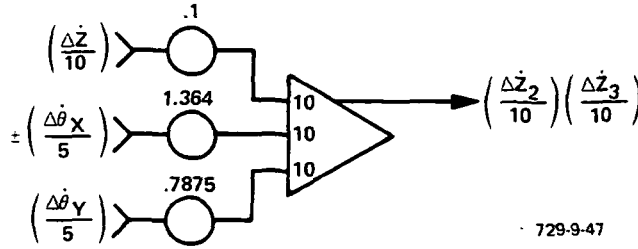
we get,

$$\left(\frac{\dot{\Delta Z}_2}{10}\right) = \left(\frac{\dot{\Delta Z}}{10}\right) + 13.64 \left(\frac{\dot{\Delta \theta}_X}{5}\right) + 7.875 \left(\frac{\dot{\Delta \theta}_Y}{5}\right) \quad (A-33)$$

and

$$\left(\frac{\dot{\Delta Z}_3}{10}\right) = \left(\frac{\dot{\Delta Z}}{10}\right) - 13.64 \left(\frac{\dot{\Delta \theta}_X}{5}\right) + 7.875 \left(\frac{\dot{\Delta \theta}_Y}{5}\right) \quad (A-34)$$

These equations are modeled below.



A.1.2.6 Axial Displacement Rates to Axial Gaps

$$\Delta Z_1 = \int \Delta \dot{Z}_1 dt \quad (A-35)$$

Scaling (A-35) for

$$\Delta Z_{1\max} = .1 \text{ in.}$$

$$\Delta \dot{Z}_{1\max} = 10 \text{ in./s}$$

we get,

$$\left(\frac{\Delta Z_1}{.1}\right) = 100 \int \left(\frac{\Delta \dot{Z}_1}{10}\right) dt \quad (A-36)$$

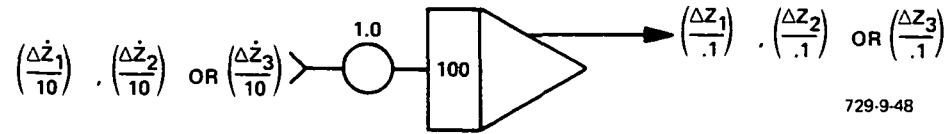
Similarly, displacement for Stations 2 and 3 are given by

$$\left(\frac{\Delta Z_2}{.1}\right) = 100 \int \left(\frac{\Delta \dot{Z}_2}{10}\right) dt \quad (A-37)$$

and

$$\left(\frac{\Delta Z_3}{.1}\right) = 100 \int \left(\frac{\Delta \dot{Z}_3}{10}\right) dt \quad (A-38)$$

Equations (A-36), (A-37) and (A-38) are shown in the following analog model diagram.



Also, the output of AD/4 is at 1000 V/in. The input to the electronics is 500 V/in. Therefore, a gain of $\frac{500}{1000} = .5$ is required at the output.

A.1.3 Radial Ripples in the Rim

Radial ripple is the imperfection of the rim in the radial dimension. For simplicity, it was assumed that the rim is imperfect only in half side, with a sinusoidal increment in its radius. The maximum incremental radius was .004 in.

$$\Delta R_1' = A_{R\omega} \sin(2\pi\omega t) | \text{positive value only}$$

for

$$\Delta R_{1\max}' = .2 \text{ in.}$$

$$\omega_{\max} = 50 \text{ r/s}$$

$$A_{R\omega} = .004 \text{ in.,}$$

we have,

$$\left(\frac{\Delta R_1'}{.2}\right) = .02 \sin \left[2\pi (50) \left(\frac{\omega}{50}\right) t \right] \quad (\text{A-39})$$

The ripple signal $\Delta R_1'$ is routed to the electronics also. Therefore,

$$\therefore (\Delta R_1')_{\text{electronics}} = .00045 \text{ in.} \left[2\pi (50) \left(\frac{\omega}{50}\right) t \right] \quad (\text{A-40})$$

Since the radial stations are located 120 degrees apart, circumferentially, ripple signals for Stations 2 and 3 are given by

$$\Delta R_2' = A_{R\omega} \sin (2\pi\omega t + 2\pi/3)$$

or

$$\left(\frac{\Delta R_2'}{.2}\right) = .02 \left[\left\{ \sin \left[2\pi 50 \left(\frac{\omega}{50} \right) t \right] \right\} \left\{ \cos (2\pi/3) \right\} + \left\{ \cos \left[2\pi 50 \left(\frac{\omega}{50} \right) t \right] \right\} \left\{ \sin (2\pi/3) \right\} \right] \quad (A-41)$$

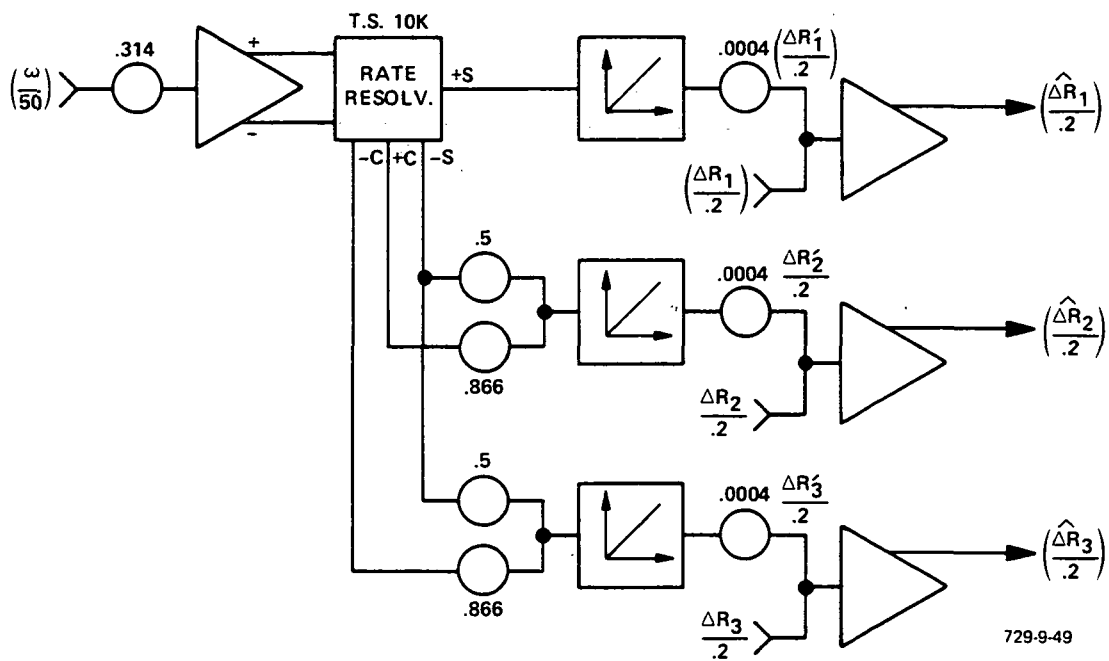
and

$$\Delta R_3' = A_{R\omega} \sin (2\pi\omega t + 4\pi/3) \quad (A-42)$$

or

$$\left(\frac{\Delta R_3'}{.2}\right) = .02 \left[\left\{ \sin \left[2\pi 50 \left(\frac{\omega}{50} \right) t \right] \right\} \left\{ \cos (4\pi/3) \right\} + \left\{ \cos \left[2\pi 50 \left(\frac{\omega}{50} \right) t \right] \right\} \left\{ \sin (4\pi/3) \right\} \right] \quad (A-43)$$

The analog block diagram for Equations (A-39), (A-41) and (A-43) is given on the following page.



Analog Block Diagram for Equations (A-39), (A-41), and (A-43)

A.1.4 Axial Ripples in the Rim

Axial ripple warp is the imperfection of the rim in the axial dimension (Z axis). For simplicity, it is assumed that the axial ripple is sinusoidal in form and changes two full cycles over the circumference of the rim. Peak to peak ripple, $2A_{A\omega}$, is .009 in.

$$\Delta Z'_1 = A_{A\omega} \sin (4\pi \omega t)$$

For

$$\Delta Z'_{1\max} = .1 \text{ in.}$$

we get,

$$\left(\frac{\Delta Z'_1}{.1}\right) = .045 \sin \left[4\pi 50 \left(\frac{\omega}{50}\right) t\right] \quad (\text{A-44})$$

and

$$(\Delta Z'_1)_{\text{electronics}} = .0045 \sin \left[2\pi (100) \left(\frac{\omega}{50}\right) t\right] \quad (\text{A-45})$$

Similarly, axial ripples for Stations 2 and 3 are given by

$$\Delta Z'_2 = A_{A\omega} \sin (4\pi \omega t + 2\pi/3) \quad (\text{A-46})$$

or

$$\left(\frac{\Delta Z'_2}{.1}\right) = .045 \left[\left\{ \sin \left[2\pi (100) \left(\frac{\omega}{50}\right) t \right] \right\} \left\{ \cos (2\pi/3) \right\} + \left\{ \cos \left[2\pi (100) \left(\frac{\omega}{50}\right) t \right] \right\} \left\{ \sin (2\pi/3) \right\} \right] \quad (\text{A-47})$$

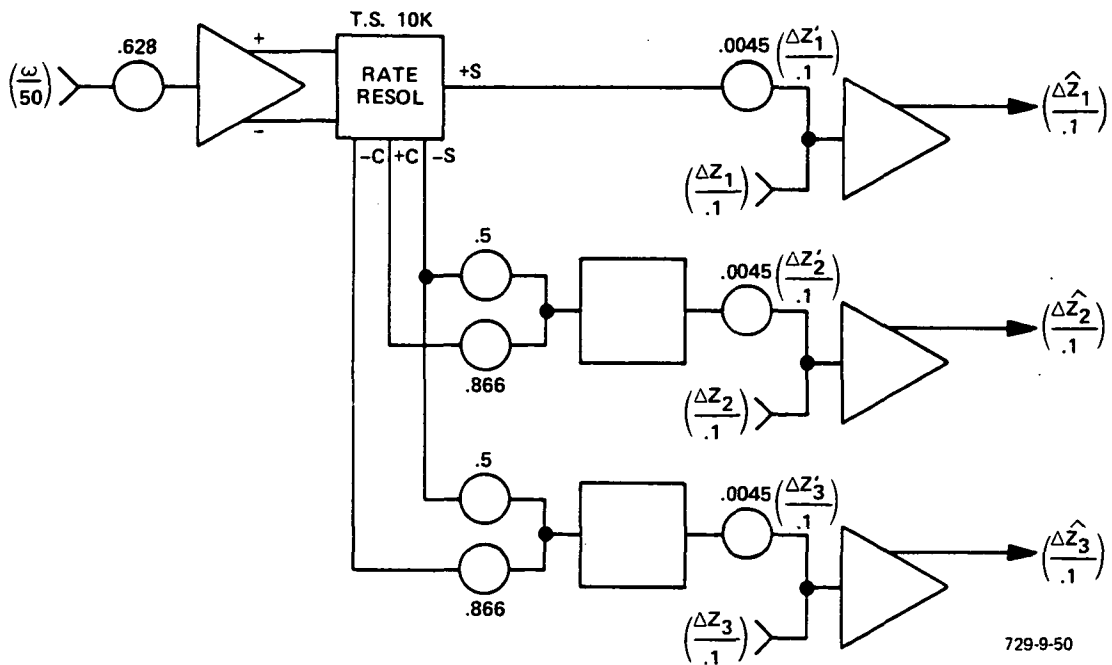
and

$$\Delta Z'_3 = A_{A\omega} \sin (4\pi\omega t + 4\pi/3) \quad (A-48)$$

or

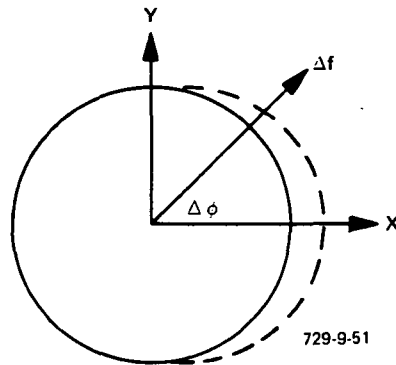
$$\left(\frac{\Delta Z'_3}{.1}\right) = .045 \left[\left\{ \sin \left[2\pi(100)\left(\frac{\omega}{50}\right)t \right] \right\} \left\{ \cos (4\pi/3) \right\} + \left\{ \cos \left[2\pi(100)\left(\frac{\omega}{50}\right)t \right] \right\} \left\{ \sin (4\pi/3) \right\} \right] \quad (A-49)$$

The analog block diagram for Equations (A-44), (A-47) and (A-49) is given below.



A.1.5 Mass Imbalance

Mass imbalance causes a deformation in the shape of the rim when rotating and creates a net force imbalance, Δf . Let $\Delta\phi$ be the angle between the resultant mass imbalance and the resultant shape irregularity, as shown in the figure below.



$\Delta f \propto \text{Mass imbalance}$

$$= \frac{M\omega^2 R}{4\pi^2} = (.975 \times 10^{-6}) \bar{\omega}^2 \quad (\text{A-50})$$

where

M = Mass imbalance

ω = Revolutions per second

R = Radius of the rim

$\bar{\omega}$ = Revolutions per minute

The incremental force ΔF_X along the X axis, for $\Delta\phi = \pi/3$, is given by

$$\Delta F_X = \Delta f (\sin 2\pi\omega t + \Delta\phi) \quad (\text{A-51})$$

Magnitude scaling (A-51), we get

$$\left(\frac{\Delta F_X}{50}\right) = 2 \times 10^{-8} \omega^2 \left\{ .5 \sin \left[100\pi \left(\frac{\omega}{50} \right) t \right] + .866 \cos \left[100\pi \left(\frac{\omega}{50} \right) t \right] \right\} \quad (A-52)$$

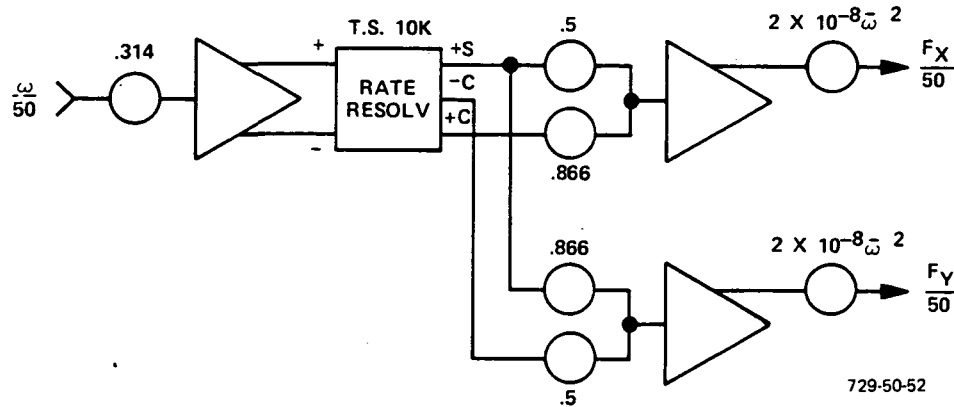
Similarly, the incremental radial force ΔF_Y along the Y axis is given by

$$\Delta F_Y = \Delta f \cos (2\pi\omega t + \Delta\phi) \quad (A-53)$$

Magnitude scaling (A-53), we get

$$\left(\frac{\Delta F_Y}{50}\right) = 2 \times 10^{-8} \omega^2 \left\{ .5 \cos \left[100\pi \left(\frac{\omega}{50} \right) t \right] + .866 \sin \left[100\pi \left(\frac{\omega}{50} \right) t \right] \right\} \quad (A-54)$$

The analog block diagram of Equations (A-52) and (A-54) is given below.



A.2 STATIC TEST SCHEME FOR AMCD SIMULATION

Two patchboards used on the AD/4 analog computers have been conveniently named "Radial Patchboard" and "Axial Patchboard." A static test scheme has been prepared for each patchboard. Tables 3 and 4 give the potentiometer settings for the radial loop patchboard and the axial loop patchboard, respectively. In order to perform the static test, the following modifications should be made before starting the static check.

TABLE 3

AMCD RADIAL LOOPS BOARD

FIELD 2				FIELD 3			
POT	VARIABLE	SETTING	POT	VARIABLE	SETTING	POT	VARIABLE
200	$.25 \times 10^2$.0000	300		1.0000	340	$A_{\text{osc}} \times 10^4 \times 50$
01			301	$A_{\text{osc}} \times 10^4 \times 50$	1.0000	41	
02	(1-b)	.0544	302	$A_{\text{osc}} \times 10^4 \times 50$.0200	342	$A_{\text{osc}} \times 10^4 \times 50$
03	b	.9456	303	"	.0200	343	$A_{\text{osc}} \times 10^4 \times 50$
04	$A_{\text{osc}} \times 10^4 \times 50$.2000	304	"	.0200	344	$A_{\text{osc}} \times 10^4 \times 50$
05	Scale Gain	.1000	305	"	.0200	345	$A_{\text{osc}} \times 10^4 \times 50$
06	(1-b) Ro	.0109	306	$A_{\text{osc}} \times 10^4 \times 50$.5000	346	$A_{\text{osc}} \times 10^4 \times 50$
07	b Ro	.1891	307	$A_{\text{osc}} \times 10^4 \times 50$.8666	347	$A_{\text{osc}} \times 10^4 \times 50$
10	$.25 \times 10^2$.8000	308	$A_{\text{osc}} \times 10^4 \times 50$.0200	0	
11			309	$A_{\text{osc}} \times 10^4 \times 50$	1.0000	1	
12	(1-b)	.0544	310	$A_{\text{osc}} \times 10^4 \times 50$.0200	2	$A_{\text{osc}} \times 10^4 \times 50$
13	b	.9456	311	"	.0200	353	$A_{\text{osc}} \times 10^4 \times 50$
14	$A_{\text{osc}} \times 10^4 \times 50$.2000	312	$A_{\text{osc}} \times 10^4 \times 50$.5000	14	$A_{\text{osc}} \times 10^4 \times 50$
15	Scale Gain	.1000	313	$A_{\text{osc}} \times 10^4 \times 50$.8666	15	$A_{\text{osc}} \times 10^4 \times 50$
16	(1-b) Ro	.0109	314	$A_{\text{osc}} \times 10^4 \times 50$.0200	16	$A_{\text{osc}} \times 10^4 \times 50$
17	b Ro	.1891	315	$A_{\text{osc}} \times 10^4 \times 50$.5000	17	$A_{\text{osc}} \times 10^4 \times 50$
20			316	$A_{\text{osc}} \times 10^4 \times 50$.8666	20	$A_{\text{osc}} \times 10^4 \times 50$
21			317	$A_{\text{osc}} \times 10^4 \times 50$.0200	21	"
22	$A_{\text{osc}} \times 10^4 \times 50$	1.0000	318	$A_{\text{osc}} \times 10^4 \times 50$	1.0000	22	
23	$A_{\text{osc}} \times 10^4 \times 50$	1.0000	319	$A_{\text{osc}} \times 10^4 \times 50$.0450	23	
24	$A_{\text{osc}} \times 10^4 \times 50$.5000	320	$A_{\text{osc}} \times 10^4 \times 50$		24	
25	$A_{\text{osc}} \times 10^4 \times 50$.0000	321	$A_{\text{osc}} \times 10^4 \times 50$		25	
26	$A_{\text{osc}} \times 10^4 \times 50$	1.0000	322	$A_{\text{osc}} \times 10^4 \times 50$.5000	26	$A_{\text{osc}} \times 10^4 \times 50$
27			323	$A_{\text{osc}} \times 10^4 \times 50$.8666	27	$A_{\text{osc}} \times 10^4 \times 50$
30	$.25 \times 10^2$.8000	324	$A_{\text{osc}} \times 10^4 \times 50$.0200	30	
31			325	$A_{\text{osc}} \times 10^4 \times 50$		31	
32	(1-b)	.0544	326	$A_{\text{osc}} \times 10^4 \times 50$.5000	32	
33	b	.9456	327	$A_{\text{osc}} \times 10^4 \times 50$.8666	33	
34	$A_{\text{osc}} \times 10^4 \times 50$.2000	328	$A_{\text{osc}} \times 10^4 \times 50$.0450	34	
35	Scale Gain	.1000	329	$A_{\text{osc}} \times 10^4 \times 50$	1.0000	35	
36	(1-b) Ro	.0109	330	$A_{\text{osc}} \times 10^4 \times 50$.8666	36	
37	b Ro	.1891	331	$A_{\text{osc}} \times 10^4 \times 50$.5000	37	

PROJECT AMCD
RADIAL LOOPS BOARD
DATE 2/21/79
3/26/79

FIELD

POT	VARIABLE	SETTING
00		
01		
02		
03		
04		
05		
06		
07		
10		
11		
12		
13		
14		
15		
16		
17		

TABLE 4

AMCD AXIAL LOOPS BOARD

FIELD 2				FIELD 3			
POT	VARIABLE	SETTING	POT	VARIABLE	SETTING	POT	VARIABLE
200			240			300	
01			41			01	
02	b	.9456	42		.9456	02	10
03	b	.9456	43		.9456	03	1000
04			44			04	3000
05	$\frac{22}{10} \times \frac{100}{30}$.5348	45	$\frac{22}{10} \times \frac{100}{30}$.5348	05	100000
06	$\frac{22}{10} \times \frac{100}{30}$.8000	46	$\frac{22}{10} \times \frac{100}{30}$.8000	06	50K
07	Scale Gain	.1000	47	Scale Gain	.10000	07	"
10			50			10	ZZ1C
11			51			11	
12	$\frac{42}{10} \times \frac{100}{30}$.2500	52	$\frac{42}{10} \times \frac{100}{30}$.9918	12	$\frac{42}{10} \times \frac{100}{30}$
13	$\frac{42}{10} \times \frac{100}{30}$.2500	53			13	$\frac{42}{10} \times \frac{100}{30}$
14		.10000	54		.10000	14	$\frac{42}{10} \times \frac{100}{30}$
15		.10000	55		.10000	15	$\frac{42}{10} \times \frac{100}{30}$
16	5Z0	.5000	56	5Z0	.5000	16	Scale Gain
17	5bZ0	.4728	57	5bZ0	.4728	17	12R
20			60			20	ZZ1C
21			61			21	
22	$\frac{42}{10} \times \frac{100}{30}$.2500	62	Limit	.10000	22	$\frac{42}{10} \times \frac{100}{30}$
23	$\frac{42}{10} \times \frac{100}{30}$.2500	63	Limit	.0000	23	$\frac{42}{10} \times \frac{100}{30}$
24	5Z0	.5000	64	5Z0	.5000	24	Pulse
25	5bZ0	.4728	65	5bZ0	.4728	25	Pulse
26	50K	.4675	66	50K	.4675	26	AMPL
27	"	.4675	67	"	.4675	27	AMPL
30			70			30	ZZ3C
31			71			31	
32		.10000	72	1/1x	.1885	32	+ZZ2 Limit
33		.1000	73	1/1y	.1885	33	-ZZ2 Limit
34	b	.9456	74	$\frac{42}{10} \times \frac{100}{30}$.3896	34	
35	b	.9456	75	Scale Gain	.1000	35	
36	$\frac{42}{10} \times \frac{100}{30}$.8000	76	1000	.0100	36	+ZZ1 Limit
237			77	$\frac{42}{10} \times \frac{100}{30}$.0300	37	-ZZ1 Limit

PROJECT
A.M.C.D.

AXIAL LOOP BOARD
DATE 2/21/79
3/20/79

FIELD			
POT	VARIABLE	SETTING	
00			
01			
02			
03			
04			
05			
06			
07			
10			
11			
12			
13			
14			
15			
16			
17			

1. On the radial patchboard
 - a) Set P200, P210 and P230 at .0500 and connect them from +Ref.
 - b) Connect 241_{IC} to +Ref.
 - c) Connect 250_{IC} to -Ref.
 - d) Set P360 and P361 at .0200.
 - e) Set P322, P335 and P342 at .1000 and connect them to +Ref.
 - f) Set P270 at .5000, P250 at .1240 and P260 at .0000.
2. On the axial patchboard
 - a) Set P206, P236 and P306 at .0500 and connect them to +Ref.
 - b) Connect 331_{IC} , 340_{IC} and 341_{IC} to +Ref.
 - c) Set P343 at .1000.

Tables 5 and 6 give the values of the output of the pots and the amplifiers for static test.

After the static test is checked out, make the following changes for actual setup.

3. On the radial patchboard
 - a) Set P200, P210 and P230 at .8000 and disconnect them from +Ref.
 - b) Disconnect 241_{IC} from +Ref.
 - c) Disconnect 250_{IC} from -Ref.
 - d) Set P360 and P361 at $2 \times 10^{-8} \times \overline{\omega}^2$ ($\overline{\omega} = r/\text{min}$)
 - e) Set P322, P335 and P342 at 1.0000 and disconnect them from +Ref.
 - f) Set P270, P250 and P260 at desired initial position of the rim.

4. On the axial patchboard

- a) Set P206, P236, P306 at .8000 and disconnect them from +Ref.
- b) Disconnect 331_{IC}, 340_{IC}, and 341_{IC} from +Ref.
- c) Set P343 at .0000.

Normal pot settings for Radial and Axial Patchboards are shown in Tables 3 and 4, respectively.

TABLE 5
RADIAL BOARD CHECKLIST

Element	Value (V)	Element	Value (V)	Element	Value (V)
A203-	-50.22	A212	52.71	A201	70.67
A200-	50.87	A203+	37.33	A200+	-49.95
A202	70.87	A213	10.55	A222-	-50.11
A210-	50.75	A260	.0000	P343	-3.89
A211	70.73	A263-	.0500	A341-	-13.90
A223	19.00	P316	.0000	P340	1.91
A222+	13.43	A300+	.0000	A012	.0000
A221	5.16	P307	-86.63	A013	-1.94
A220	51.51	P317	+1.70	A003	1.91
A261	26.52	A217-	14.22	A002	14.22
A243-	-49.95	A301+	86.59		
A230-	50.58	P315	86.60		
A231	70.64	P310	.0000		
A253	5.41	A310+	.0000		
A210+	3.84	A263-	.0500		
A252	1.07	P327	-86.61		
A240	70.04	A322+	86.62		
A242+	-49.07	P323	.0000		
A243+	49.07	P337	-50.01		
A271+	12.08	A323	-50.01		
A242-	19.56	A320+	-10.00		
A241	+100	P330	.0000		
A250	-100	P333	-86.58		
A270	+50	A331+	-86.58		
A262+	+50	P334	3.88		
A262-	-36.62	A331-	-6.11		
A263+	136.67	P320	-1.94		
A251	12.50	P344	86.60		
A271-	14.22	A341+	+86.60		

TABLE 6
AXIAL BOARD CHECKLIST

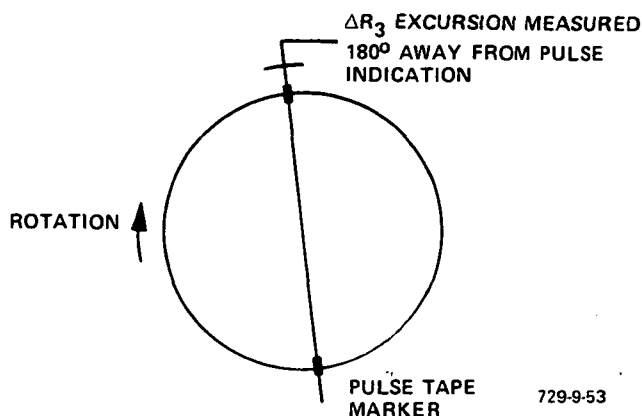
Element	Value (V)	Element	Value (V)	Element	Value (V)
A202-	-50.00	A260	103.67	A352	18.84
A200-	50.69	A261	.0000	A353	18.82
A203	50.05	A342+	-107.05	A350	10.00
A210	51.72	A342-	.0000	A362-	1.88
A201	-100.09	A343	-50.05	A363-	1.90
A211	51.73	A302-	-50.07	A351	51.95
A200+	.0000	A300-	50.10	A262+	24.92
A212+	51.77	A303	50.04	A360	51.95
A212-	-51.77	A310	51.72	A263+	24.94
A213	49.94	A301	-99.99	A361	51.94
A220	-49.99	A311	51.69	A263-	24.96
A222	103.60	A300+	.0000	SJ331	-19.48
A223	.0000	A312+	51.65	SJ351	161.27
A221+	-107.23	A312-	-51.76	SJ360	161.24
A221-	.0000	A313	49.96	SJ361	-85.00
A230	-50.13	A320	-50.01	A271	11.30
A231-	-50.07	A322	103.37	A363+	.0000
A240-	50.72	A323	.0000		
A242	50.04	A321+	-106.75		
A241	-51.76	A321-	.0000		
A243	-99.94	A330	-49.90		
A250	51.88	A270+	50.02		
A262-	.0000	A270-	.0000		
A251+	51.84	A302+	-.0005		
A251-	-51.84	A331	99.93		
A252	49.96	A340	99.93		
A253	-50.00	A341	99.94		

APPENDIX B

AMCD LOW SPEED BALANCE

APPENDIX B AMCD LOW SPEED BALANCE

The rim was balanced dynamically at low speeds ranging from 200 r/min to 350 r/min. Details of the trial runs are given below. A total of 24 grams of lead tape was added to the mass of the rim. The criteria and the location of this added mass is explained here.



B.1 BALANCE IMPROVEMENT AT 200 R/MIN

Run No. 1, 12/28/78

Baseline run, no weight added.

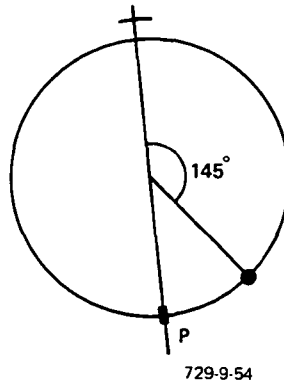
Chart speed = 200 mm/s, Pulse τ = 57 mm

$$\rightarrow N = 210.5 \text{ r/min}, \frac{360^\circ}{57} = 6.32^\circ/\text{mm}$$

Max ΔR_3 occurs at ΔR_3 at pulse + (23 mm) (6.32 $^\circ/\text{mm}$) = ΔR_3 Pulse
+ 145 $^\circ$

$$\Delta R_3 \text{ amplitude} = \frac{15}{2} = 7.5 \text{ mm} = (7.5 \text{ mm}) \left(\frac{.020 \text{ in.}}{16.5 \text{ mm}} \right) = .0091 \text{ in.}$$

i.e., .009 in. is the original unbalance amplitude at 200 r/min.



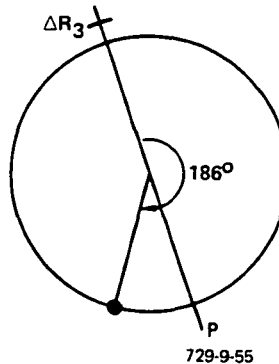
NOTE: This unbalance amplitude would theoretically increase as the square of the speed ratio, i.e., at 700 r/min would get $\left(\frac{700}{200}\right)^2 (.009) = .110$ in. (theoretically). The speed-squared effect was verified by checking amplitude at 100 r/min (about $T/2 = 3.5$ mm, as expected).

Run No. 2, 12/28/78

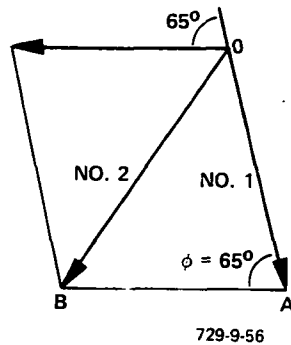
(Add 10 gm at ≈ 130 degrees CW from pulse)

$$\tau = 58 \text{ mm} \rightarrow \frac{360}{58} \text{ deg} = 6.21^\circ/\text{mm}$$

$$\text{Max } \Delta R_3 \text{ at } \Delta R_3 \text{ at } P + (6.21) (30 \text{ mm}) = P + 186^\circ$$



From polar plot, $\phi_{12} = 65^\circ$, \rightarrow move the weight from 130° to 195° CW from P weight magnitude.



AB is the effect of the added weight of 10 gm at 130° .
 $OA = 3.75$ in. on polar plot
 $AB = 2.58$ in. on polar plot

$$\rightarrow \text{Weight} = 10 \text{ gm} \left(\frac{3.75}{2.58} \right) = 14.5 \quad (15 \text{ gm at } P + 195^\circ)$$

Run No. 4, 12/28/78

(Try 10 gm at 195° CW from P)

$$\tau = 57.5 \text{ mm} \rightarrow 6.26^\circ/\text{mm}$$

$$\Delta R_3 \text{ max at } \Delta R_3 \text{ at } P + (\approx 17 \text{ mm}) (6.26) = P + 106^\circ$$

$$\Delta R_3 \text{ Amplitude} = \frac{9.0}{2} = 4.5 \text{ mm; } oc = 2.65 \text{ in. (Figure 39)}$$

$$\rightarrow \text{Weight} = \frac{OA}{OC} = \frac{3.75}{2.65} (10) = 14.1 \text{ gm at } 195 - \phi_{13} = 195 - 35 = 160^\circ$$

Run No. 5, 12/28/78

(Try 18 gm at ≈ 165 deg)

$$\tau = 57.2 \text{ mm} \rightarrow 6.29^\circ/\text{mm}$$

$$\text{Max } \Delta R_3 \text{ at } \Delta R_3 \text{ at } P + (6.29) (32.2 \text{ mm}) = P + 203^\circ$$

$$\Delta R_3 = \frac{9}{2} = 4.5 \text{ mm; } OD = 3.22 \text{ (Figure 39)}$$

$$\text{Next Weight} = \frac{3.75}{3.22} (18) = 21 \text{ gm}$$

$$\phi_{15} = 35^\circ$$

Try 18 gm at $P + 165 + 35 = P + 200^\circ$ (CW from P)

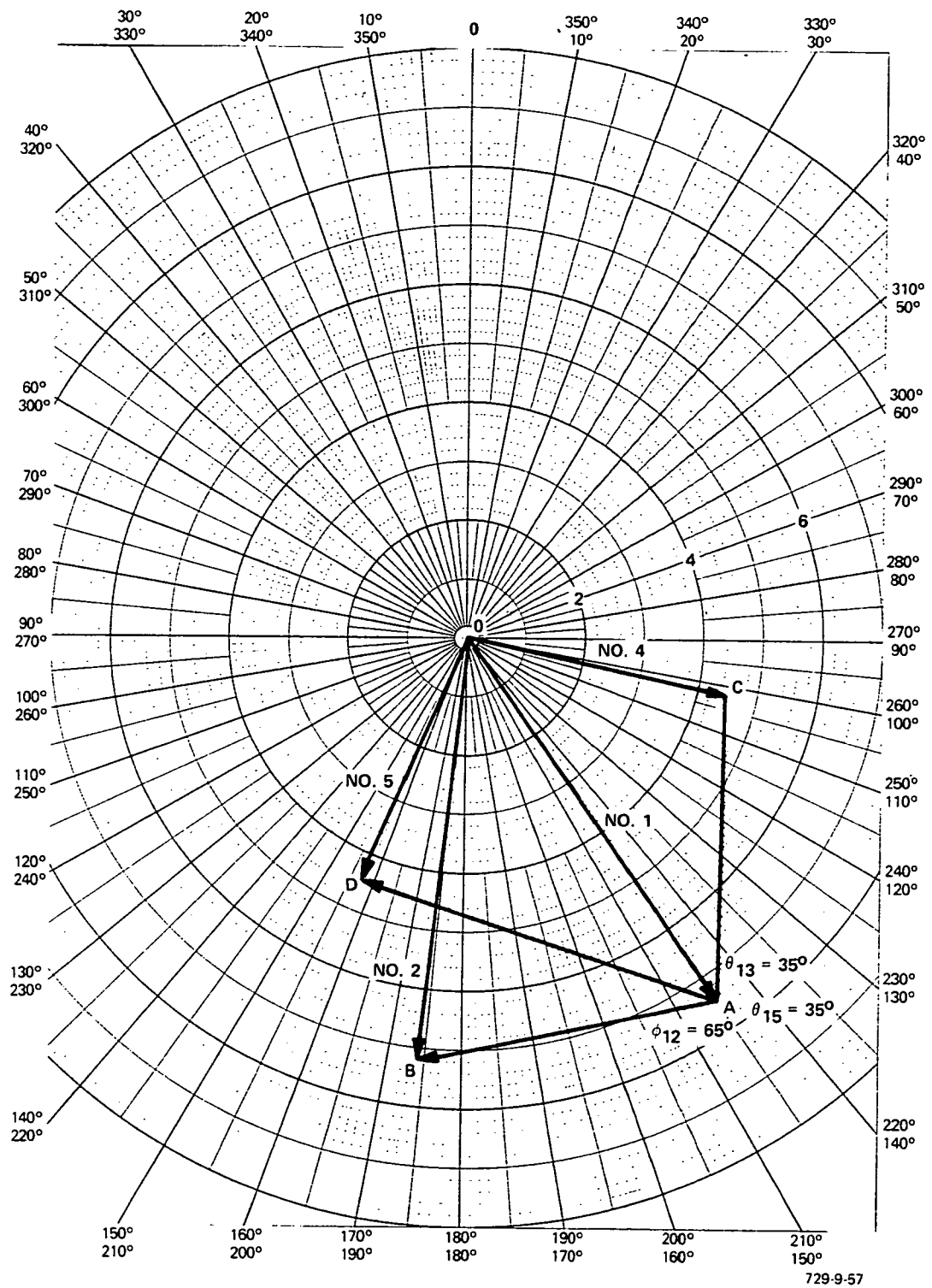


Figure 38
Balance Improvement at 200 R/Min

Run No. 1, 12/29/78

(18 gm at ≈ 195 deg)

$$\tau = 57.2 \text{ mm} \rightarrow 6.29^\circ/\text{mm}$$

$$\text{Max } \Delta R_3 \text{ at } P + (14) (6.29) = P + 88^\circ$$

$$\Delta R_3 = 5/2 = 2.5 \text{ mm}$$

$$\Delta E = 3.25 \text{ (Figure 40)}$$

$$\text{Weight} = \frac{3.75}{3.25} (18) = 21 \text{ gm}, \phi = 20^\circ \text{ (Figure 40)}$$

$$21 \text{ gm at } 195^\circ - 20^\circ = 175^\circ$$

Balanced reasonably good \rightarrow increase speed.

B.2 BALANCE IMPROVEMENT AT 350 R/MIN

Run No. 2, 12/29/79

(18 gm at ≈ 195 degrees) (350 r/min) (baseline at 350 r/min)

$$\tau = 34.6 \text{ mm} \rightarrow 10.4^\circ/\text{mm} (\rightarrow N = 347 \text{ r/min})$$

$$\Delta R_{\text{max}} \text{ at } \Delta R_3 \text{ at } P + (9.5 \text{ mm}) (10.4) = P + 99^\circ$$

$$\Delta R_3 = \frac{9.5}{2} = 4.75 \text{ mm}; \text{OA} = 2.375 \text{ in. (Figure 41)}$$

$$\Delta R_3 \text{ w/o balancing would have been } \left(\frac{350}{200}\right)^2 (7.5 \text{ mm}) = 23 \text{ mm.}$$

(\rightarrow Amplitude decrease by factor of about 5)

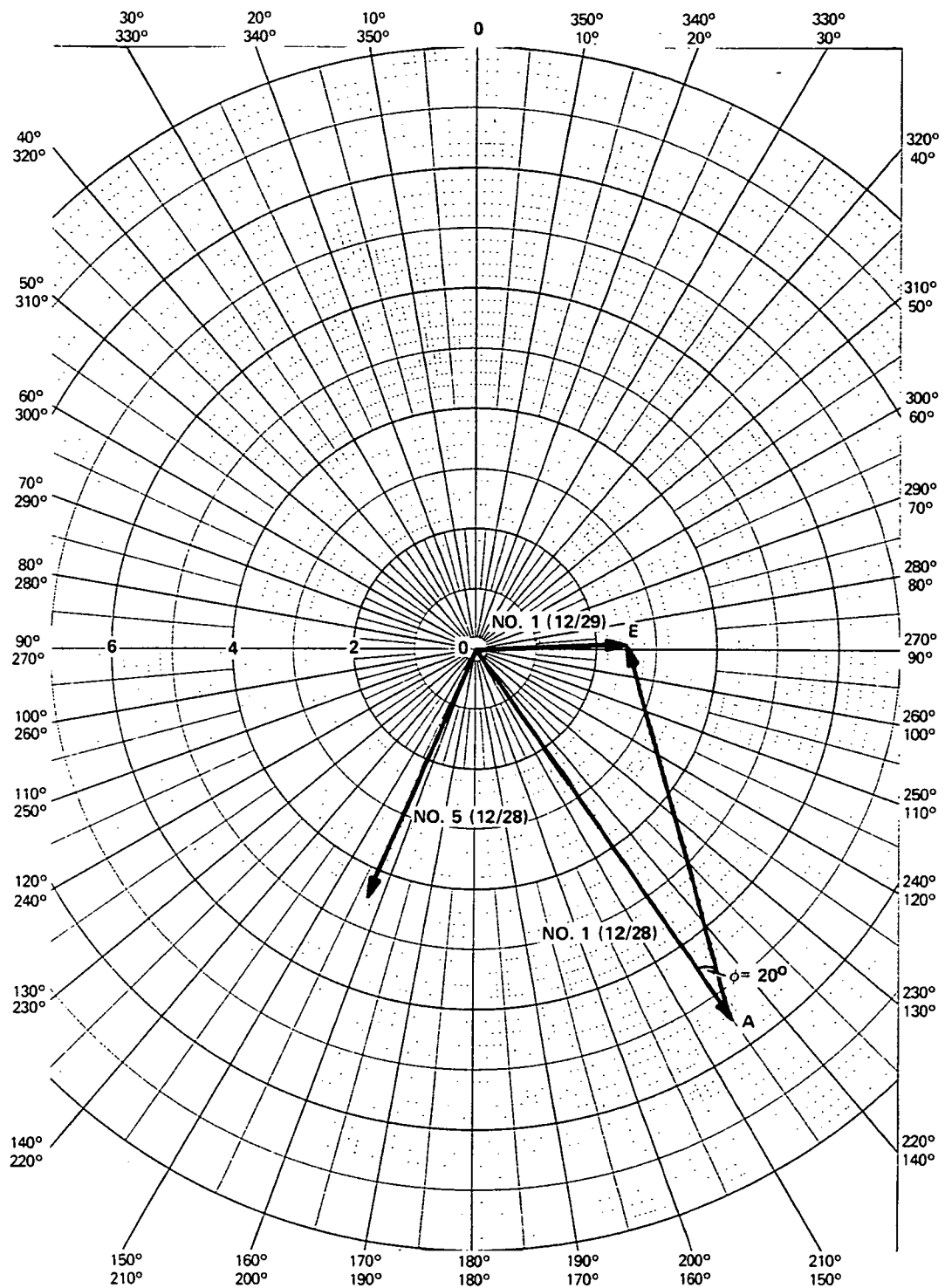


Figure 39
Balance Improvement at 200 R/Min

729-9-58

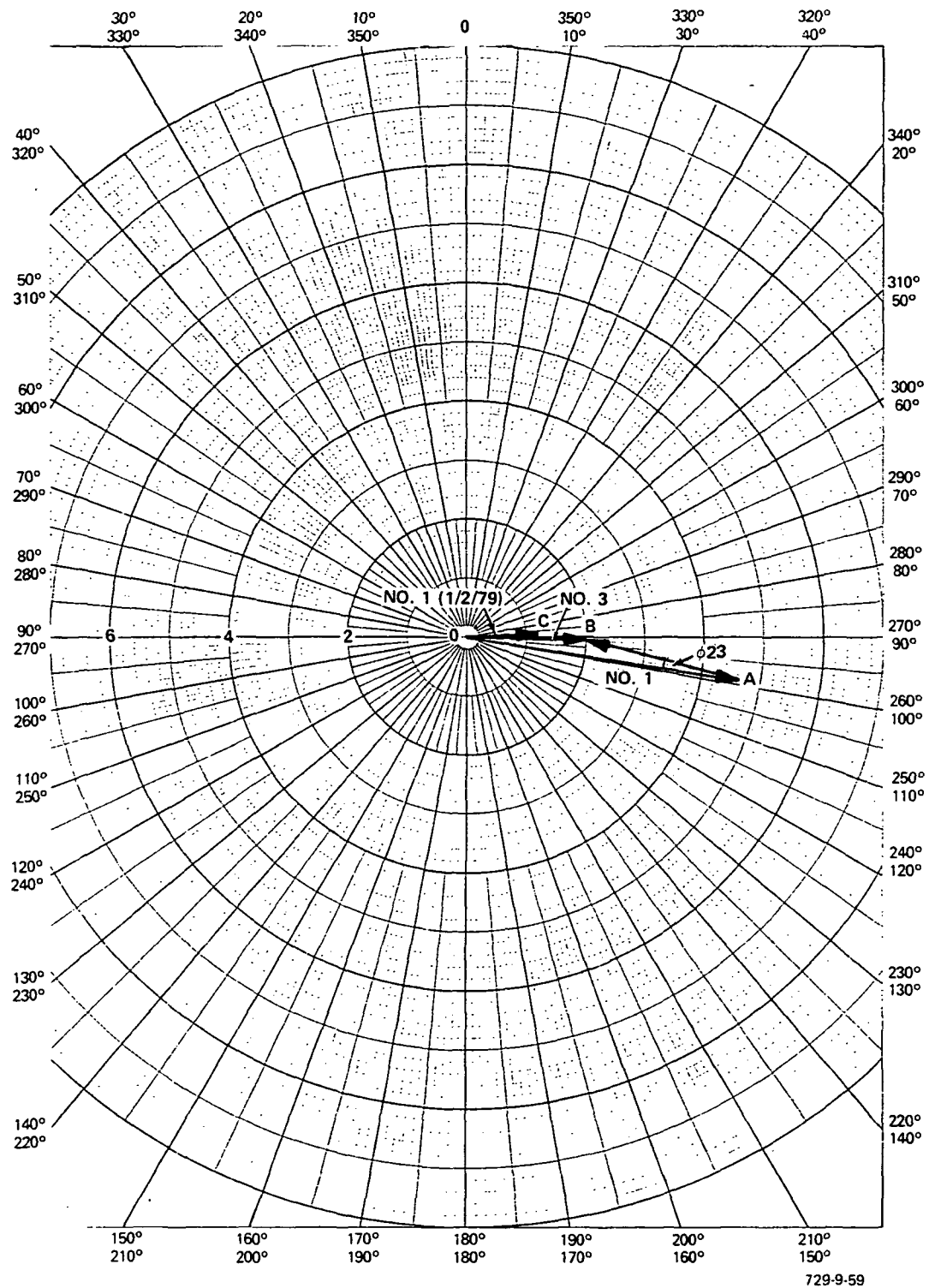


Figure 40
Balance Improvement at 350 R/Min

Run No. 3, 12/29/79

(Added 4 gm at ≈ 185 degrees or total weight ≈ 22 gm. at $\approx 185^\circ - 200^\circ$)

$$\tau = 33.6 \text{ mm} \rightarrow 10.71^\circ/\text{mm} \text{ (N = 357 r/min)}$$

$$\text{Max } \Delta R_3 \text{ at } P + (8.5 \text{ mm}) (10.71) = P + 91^\circ \text{ (Rel to } R_3 \text{ point)}$$

$$\Delta R_3 = \frac{4}{2} = 2 \text{ mm; AB} = 1.4 \text{ in.}$$

$$\phi_{23} = 5^\circ$$

$$\text{Weight} = (4 \text{ gm}) \left(\frac{2.375}{1.4} \right) = 6.8 \text{ gm and move center 5 degrees CCW;}$$

i.e., add 7 gm (to the 18 gm at $195^\circ (\approx)$) at $\approx 180^\circ$ rel to P

Run No. 1, 1/2/79

(24 gm total over 170° to 205°)

$$\tau = 34.2 \text{ mm} \rightarrow 10.53^\circ/\text{mm}$$

$$\text{Max } \Delta R_3 \text{ at } P + (8.5 \text{ mm}) (10.53) = P + 89.5^\circ \text{ (rel to } R_3 \text{ point)}$$

$$\Delta R_3 = \frac{2.6}{2} = 1.3 \text{ mm (OC on Figure 41)}$$

$$\Delta C = 1.74 \text{ in. on Figure 41, } \phi \approx 4^\circ$$

Weight = 6 gm $\left(\frac{2.375}{1.74} \right) \approx 8$ gm instead of 6 on the CCW side of this run's location

Balance judged good enough to go to higher speed.

Amplitude reduced from what would have been $(.0091 \text{ in.}) \left(\frac{350}{200} \right)^2 = .028 \text{ in. to } (1.3 \text{ mm}) \left(\frac{.020 \text{ in.}}{16.5 \text{ mm}} \right) = .0016$ or by factor of ≈ 18 at ≈ 350 r/min.

Run No. 2, 1/3/79

(24 gm at 170° to 205° CW from pulse tape)

(200 mm/s trace speed)

$$\tau = 17 \text{ mm} \rightarrow N = 706 \text{ r/min}$$

$$\text{Max } \Delta R_3 = \frac{8}{2} = 4 \text{ mm}$$

$$\text{Amplitude} = 4 \text{ mm} \left(\frac{.020 \text{ in.}}{16.5 \text{ mm}} \right) = .00485 \text{ in.} \approx .005 \text{ in.}$$

Without balancing, amplitude can be projected to have been (.0091)
 $\left(\frac{700}{200} \right)^2 = .111 \text{ in.}$, giving a reduction factor of $\frac{.111}{.005} \approx 23$ at 700 r/min

Balance attempts at 600 r/min did not reduce the amplitude. It appears that the remaining apparent unbalance is actually a rim warp rather than mass unbalance.

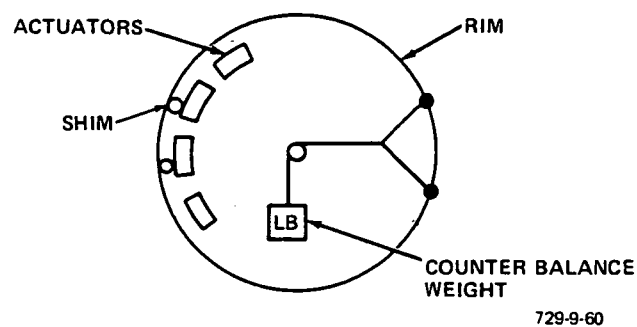
Portions of recorder traces for the above runs are filed in Lab Notebook PX 2751.

APPENDIX B

AMCD LOW SPEED BALANCE

APPENDIX C
AMCD MAGNETIC BEARING CHARACTERIZATION

Digital simulation of the system suggested that the bandwidths of the radial and axial loops could be reduced considerably if accurate values of actuator constants could be determined and incorporated. An experiment was thus set up to determine these actuator constants, viz. K and b , in-situ condition. The following describes the test setup.



The rim was suspended level from three steel rods placed at the opening of the AMCD test-pit. The rim was adjusted to be equidistant from all three radial stations. All of the axial actuators and radial actuators for Stations 2 and 3 were disabled. Station 1 radial actuators were excited. Movement of the rim was counterbalanced by weights suspended diametrically opposite Station 1. This was repeated for Stations 2 and 3. From the known values of the gap, balancing weights and excitation currents, the values of K and b were calculated.

The experiment was not totally successful. The rim could not be perfectly leveled and plumbed because of the continuous stretching of the suspension wires. Also, the line of application of counterbalancing weights could not be set exactly diametrically opposite the station under test. The gap between the rim and four actuators of one station was not uniform. The EM department set up

a separate fixture to determine the actuator constants using a single actuator. Given below is the summary of the average values of constants from the above experiments.

	<u>Station 1</u>	<u>Station 3</u>	<u>EM Dept Exp</u>
b	.937	.9223	.9456
K	.006258	.008358	.00935
b (range)	(.818 - .998)	(.784 - .998)	(.914 - .973)
K (range)	(.0051 - .00797)	(.00685 - .00918)	(.00856 - .00975)

Values of $b = 0.9456$ and $K = .00935 \text{ lb-in.}^2/\text{A}^2$ were incorporated in the electronics. The response of the system was improved substantially. The previously observed high frequency noise in the rim displacement signal at zero speed disappeared, and the rim responded well to the external incremental displacement commands.

DISTRIBUTION LIST

Pub. No. 72-8191-04-02

MAGNETIC SUSPENSION SYSTEM FOR
AN ANNULAR MOMENTUM CONTROL
DEVICE (AMCD) (FINAL REPORT)

October 1980

Coordinator: C. Cotler

Copy No.		Mail Station
1 - 5*	NASA Langley Research Center (via H. Richard)	207A
6	H. Richard	207A
7	R. Van Riper	108C
8	J. Harrison	108C
9	G. Waldeck	108C
10	M. Khetarpal	108C
11	F. Richards	201C
12	Publications File	Peoria
13 - 100	Spares	Peoria

* plus one reproducible copy for NASA (via H. Richard)

1. Report No. NASA CR-159255		2. Government Accession No.		3. Recipient's Catalog No.	
4. Title and Subtitle MAGNETIC SUSPENSION SYSTEM FOR AN ANNULAR MOMENTUM CONTROL DEVICE (AMCD)				5. Report Date December 1979	
				6. Performing Organization Code	
7. Author(s) M. L. Khetarpal				8. Performing Organization Report No.	
9. Performing Organization Name and Address Sperry Flight Systems P.O. Box 21111 Phoenix, AZ 85036				10. Work Unit No.	
				11. Contract or Grant No. NAS1-14502	
12. Sponsoring Agency Name and Address National Aeronautics and Space Administration Washington, DC 20546				13. Type of Report and Period Covered Contractor Report	
				14. Sponsoring Agency Code	
15. Supplementary Notes Langley Technical Monitor: David E. Terray Final Report					
16. Abstract A new magnetic suspension system for an existing laboratory test model Annular Momentum Control Device (AMCD) is described and test results presented. The suspension system utilizes zero flux-bias magnetic bearing actuators for both axial and radial control. Test results include system open- and closed-loop frequency response at zero rim speed and at a rim speed of 500 rpm. A description of an analog computer simulation of the AMCD system, a description of the method used to achieve low speed dynamic balance of the AMCD rim, and a description of the magnetic bearing characterization approach is also presented.					
17. Key Words (Suggested by Author(s)) Magnetic suspension system				18. Distribution Statement Unclassified - Unlimited	
19. Security Classif. (of this report) Unclassified		20. Security Classif. (of this page) Unclassified		21. No. of Pages 101	
22. Price*					